Fakultät für Physik der Technischen Universität München
Physik-Department E12

Decay spectroscopy of neutron-rich nuclei around ^{37}Al

Konrad Steiger

Abstract

A decay spectroscopy experiment investigating extreme neutron-rich nuclei around ^{37}Al is presented in this thesis. For modern nuclear structure physics this part of the nuclear chart is interesting to study as the classical magic numbers 20 and 28 might disappear and new shell gaps are suspected there.

The experiment discussed in this thesis was performed in fall 2010 at the RIKEN Nishina Center in Wako (Japan). Neutron-rich nuclei were produced by relativistic projectile fragmentation of a 345 A MeV ^{48}Ca primary beam on a beryllium target. The secondary cocktail beam was separated and unambiguously identified with the "BigRIPS" fragment separator and the "ZeroDegree" spectrometer. The fragments were implanted in the "CAITEN" detector (Cylindrical Active Implantation Target for Exotic Nuclei) which is a completely new detector concept optimized for high rate secondary beams. It consists of a highly segmented plastic scintillator with the shape of a hollow cylinder which is read out by position sensitive photomultiplier tubes. A rotation and a vertical motion of the scintillator reduce background decay events as long-lived radioactivity is transported away from the active area of the detector. Implantations and β decays are correlated in time and space. γ-rays are detected by three germanium clover detectors.

The half-lives of ^{29}F, ^{30}Ne, ^{35,36}Mg and ^{37}Al could be determined with a higher precision than previously known. For ^{31,35}Na und ^{38}Al the known half-life values could be confirmed within a confidence level of 2σ. β-delayed γ-ray spectroscopy was performed to detect deexcitations of the nuclei populated in the β decay and decay cascades were reconstructed by measuring γ-γ coincidences. Applying these methods after the decay of ^{30}Ne the low-energy level structure of ^{30}Na which was recently reported in [Tri07a] could be confirmed. For the first time a level scheme of ^{37}Si could be determined by detecting β-delayed γ-rays after the decay of ^{37}Al. Transitions with energies of 156, 562, 717, 1115, 1202 and 1270 keV were placed in the level scheme of ^{37}Si. γ-rays with energies of 418, 1074, 1159, 1470 and 2211 keV were measured after the decay of ^{38}Al and could be attributed to a partial level scheme of ^{38}Si. In addition several new γ-rays were observed after the decays of ^{29}F, ^{35}Na and ^{36}Mg. The results were compared to new shell model calculations using the effective interactions SDPF-MU and SDPF-U which allow a tentative assignment for the spin and parity values of the experimental energy levels. Furthermore the new results give evidence for the modification of the input parameters of these shell model calculations.

Zusammenfassung

In dieser Arbeit wird ein Experiment vorgestellt, bei dem extrem neutronenreiche Kerne in der Umgebung von ^{37}Al mittels Zerfallsspektroskopie untersucht wurden. Dieser Teil der Nuklidkarte ist von großem Interesse für die moderne Kernstrukturphysik, da dort die klassischen magischen Zahlen 20 und 28 verschwinden könnten und neue Schalenabschlüsse vermutet werden.

Das Experiment fand im Herbst 2010 am RIKEN Nishina Center in Wako (Japan) statt. Durch relativistische Projektilfragmentation eines ^{48}Ca Primärstrahls mit einer Energie von 345 A MeV in einem Beryllium Target wurden extrem neutronenreiche Kerne erzeugt. Die gewünschten Fragmente wurden im "BigRIPS" Fragmentseparator und dem "ZeroDegree" Spektrometer separiert und eindeutig identifiziert. Anschließend wurden sie in den "CAITEN" Detektor (Cylindrical Active Implantation Target for Exotic Nuclei) implantiert. Dies ist ein neues Detektorsystem, das für Sekundärstrahlen mit hohen Raten optimiert ist. Es besteht aus einem vielfach segmentierten, beweglichen Plastikszintillator in Form eines Hohlzylinders, der mit positionsempfindlichen Photomultipliern ausgelesen wird. Eine Rotation und eine vertikale Bewegung des Szintillators reduzieren dabei Untergrundzerfälle durch den Abtransport von langlebiger Radioaktivität aus der aktiven Fläche des Detektors. Implantationen und darauf folgende β-Zerfälle können durch Ort- und Zeitkorrelation einander zugeordnet werden. γ-Zerfälle werden mit drei Germanium-Clover-Detektoren nachgewiesen.

Die Halbwertszeiten von ^{29}F, ^{30}Ne, ^{35,36}Mg und ^{37}Al wurden mit einer höheren Genauigkeit als bisher bekannt gemessen und für ^{31,35}Na und ^{38}Al konnten innerhalb eines Konfidenzbereichs von 2σ die bisherigen Halbwertszeiten bestätigt werden. β-verzögerte Gammaspektroskopie ermöglichte die Messung von Übergängen in Tochterkernen. Mittels γ-γ Koinzidenzen konnten Zerfallskaskaden nachgewiesen werden. Diese Methode ermöglichte die Bestätigung des vor kurzem gemessenen Niveauschemas von ^{30}Na nach dem Zerfall von ^{30}Ne [Tri07a]. Außerdem konnte erstmals ein Niveauschema von ^{37}Si nach dem Zerfall von ^{37}Al konstruiert werden. Dort wurden γ-Zerfälle mit den Energien 156, 562, 717, 1115, 1202 und 1270 keV in ^{37}Si nachgewiesen. Nach dem Zerfall von ^{38}Al konnten γ-Zerfälle mit den Energien 418, 1074, 1159, 1470 und 2211 keV der Tochter ^{38}Si zugeordnet werden. Zudem wurden neue γ-Übergänge nach den β-Zerfällen von ^{29}F, ^{35}Na und ^{36}Mg beobachtet. Die Ergebnisse wurden mit neuen Schalenmodellrechnungen mit den effektiven Wechselwirkungen SDPF-MU und SDPF-U verglichen. Damit konnten Hinweise auf Spin und Parität der experimentell bestimmten Energieniveaus gefunden werden. Zudem liefern die neuen experimentellen Ergebnisse Hinweise für die Modifikation von Eingangsparametern dieser Schalenmodellrechnungen.

Contents

Chapter 1

Introduction

The nuclear shell model was introduced in 1949 [Goe49, Hax49]. It predicts the so called "magic numbers" 2, 8, 20, 28, 50, 82 and 126: At these proton or neutron numbers there are large gaps between the single particle energies of nuclear (sub-)shells. The gaps arise from a central potential (e.g. a phenomenological Woods-Saxon potential) in combination with the spin-orbit force. This concept of independent particles moving in a potential can explain many experimental results like ground state spins, excited states and magnetic moments for nuclei with only one particle outside or one hole inside a magic core. But this model cannot account for all aspects of the interaction between the nucleons.

A more realistic model than this independent particle model is the interacting shell model which has been used for many years. A configuration space is chosen to have a closed core which consists of fully occupied proton and neutron shells and a valence space. Nucleons in this valence space interact via the so called residual interaction. There are two different kinds of input parameters for this model: The single-particle energies (SPEs) ϵ_i of the valence orbits i and the two-body matrix elements (TBMEs) which model the residual interaction between nuclei outside the closed core. The SPEs are taken from experimental data and the TBMEs are derived from fitting nuclear properties in a certain region of the nuclear chart. The TBMEs are written as $\langle j_1 j_2 | V | j_3 j_4 \rangle_{JT}$. The nucleons occupy the orbits i with the angular momenta j_i. They couple to the total angular momentum J and the total isospin T. V is an effective interaction. All combinations of j_i have to be taken into account. As an example nuclei with the neutron numbers $N = 2 - 8$ and proton numbers $Z = 2 - 8$ can be modeled with a ^{4}He core and a $0p$ valence space, which includes the orbits $0p_{3/2}$ and $0p_{1/2}$. The SPEs of the two orbits $0p_{3/2}$ and $0p_{1/2}$ and 15 TBMEs have to be known to perform such a calculation [Coh65]. For the calculation of heavier nuclei the number of TBMEs increases. Nuclei with the neutron numbers $N = 8 - 20$ and proton numbers $Z = 8 - 20$ can be calculated with a ^{16}O core and a 1s0d valence space including the $0d_{5/2}$, $1s_{1/2}$ and $0d_{3/2}$ orbits. A calculation with this configuration space needs 63 TBMEs and 3 SPEs as input parameters [Wil84].

In the recent years large scale shell model calculations became possible which allow to include the interaction between many more valence particles than previously possible. In addition, new components like the tensor force were included in the residual inter-

action to calculate TBMEs. The driving force for the change of shell gaps and ESPEs towards nuclei with extreme isospin is the monopole term of the residual interaction that is dominated by the tensor force [Ots05]. The so called monopole Hamiltonian

$$V_{j_1 j_2}^T = \frac{\sum_J (2J+1) \langle j_1 j_2 | V | j_1 j_2 \rangle_{JT}}{\sum_J (2J+1)} \tag{1.1}$$

is the average over all orientations of the interaction between two particles in the orbits with the angular momenta j_1 and j_2. The effective single particle energies (ESPEs) are calculated with the bare SPEs and the effects from $V_{j_1 j_2}^T$ as a measure of the mean effect from other nucleons on a nucleon in a specific orbit. The ESPE of an orbit is defined as the separation energy of a nucleon in this orbit with the opposite sign. As the J dependence is taken away, only the number of nucleons in each orbit matters [Ots01]. Consequently by filling n_{j_2} protons (neutrons) in the orbit j_2 the ESPE of the neutron (proton) orbit j_1 changes by $\Delta \text{ESPE}_{j_1} = (V_{j_1 j_2}^{T=0} + V_{j_1 j_2}^{T=1}) n_{j_2}$ [Ots05].

In the reference [Ots10] the monopole-based universal interaction V_{MU} is introduced which consists of two terms: A Gaussian central force and the tensor force composed of π and ρ meson exchanges. An illustration of the two terms can be seen in figure 1.1. A schematic picture of the consequence of the tensor force between protons and neutrons is shown in the left part of figure 1.2: The orbital angular momenta of protons and neutrons are denoted by l and l' and the protons can occupy the $j_> = l + 1/2$ or $j_< = l - 1/2$ orbits and neutrons can occupy the $j'_> = l' + 1/2$ or $j'_< = l' - 1/2$ orbits. The tensor force created by a neutron in the $j'_>$ orbit acts attractively (repulsively) for a proton in the $j_<$ ($j_>$) orbit and vice versa. For neutron in the $j'_<$ orbit it is the opposite. If both $j'_>$ and $j'_<$ are fully occupied the tensor force vanishes [Ots05]. The right part of figure 1.2 shows the resulting neutron EPSEs of the $N = 20$ isotones. Without the tensor force there is a rather monotonic decrease of the $N = 20$ shell gap between the $d_{3/2}$ and $f_{7/2}$ orbits going from $Z = 20$ to $Z = 8$. But with the tensor force the $N = 20$ shell gap is approximately constant from $Z = 20$ to $Z = 14$ and decreases from $Z = 14$ to $Z = 8$. While going from $Z = 14$ to $Z = 8$ six protons are removed from the $d_{5/2}$ orbit. As explained before the tensor force generated by these
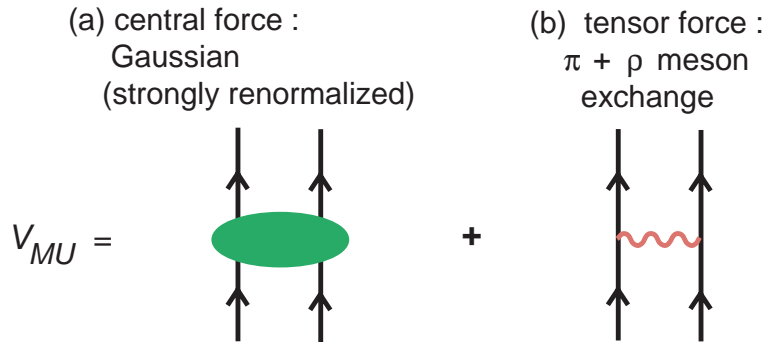

Figure 1.1: Illustration of the two terms of the monopole-based universal interaction V_{MU}, adopted from [Ots10].
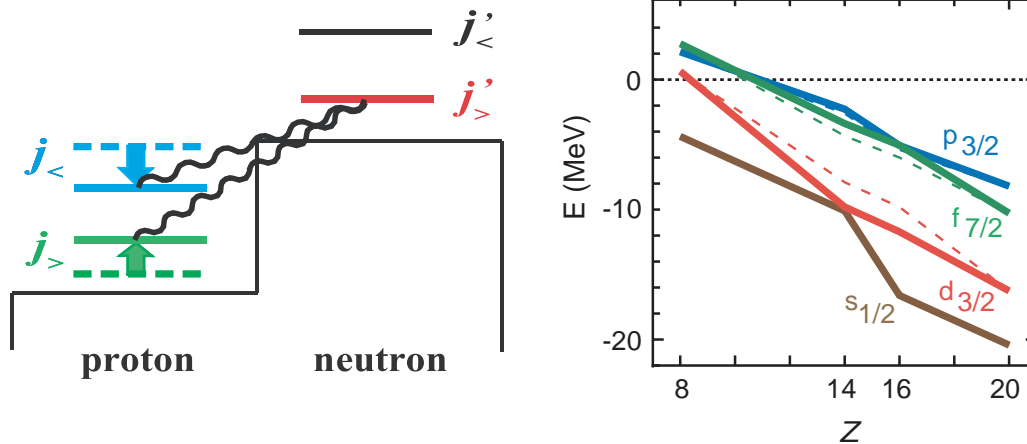
Figure 1.2: *Left:* Schematic picture of the tensor force between protons and neutrons. A neutron in the $j'_>$ orbit acts attractively (repulsively) for a proton in the $j_<$ ($j_>$) orbit. Taken from [Ots05]. *Right:* Evolution of neutron effective single-particle energies (EPSEs) of $N = 20$ isotones for the $1s_{1/2}$, $0d_{3/2}$, $0f_{7/2}$ and $1p_{3/2}$ neutron orbits. Solid (dashed) lines represent calculation with the V_{MU} interaction with (without) the tensor force. Taken from [Ots10].

$d_{5/2}$ protons lowers the ESPE of the $d_{3/2}$ neutrons. Consequently removing the $d_{5/2}$ protons increases the neutron $d_{3/2}$ ESPE. This increase vanishes the $N = 20$ shell gap and produces a new shell gap at $N = 16$ for $Z = 8$ [Ots10].

An important consequence of the tensor force is the formation of the so called "Island of Inversion" for neutron-rich Ne, Na and Mg nuclei with $Z = 10 - 12$. As can be seen in the right part of figure 1.2 neither the classical $N = 20$ shell gap nor the "new" $N = 16$ shell gap which appears at $Z = 8$ is large for these nuclei but there is a rather equal difference between the $1s_{1/2}$, $0d_{3/2}$ and $0f_{7/2}$ ESPEs. Therefore quadrupole correlations which have a similar strength compared to the differences of the ESPEs play an important role for these nuclei. That is why a partial occupation of orbits in the pf-shell leads to an effective lowering of ESPEs of pf-shell orbits compared to the sd-shell. Consequently deformed 2-particle-2-hole (2p-2h) intruder configurations across the $N = 20$ shell gap are lowered in energy and can compete with spherical 0p-0h configurations. As a result nuclei inside the Island of Inversion have ground states which are dominated by deformed 2p-2h intruder configurations caused by quadrupole collectivity and states with a spherical 0p-0h configuration become excited states. Figure 1.3 illustrates the inversion of the 2p-2h and 0p-0h 0^+ states by comparing the level schemes of ^{32}Mg which is inside the Island of Inversion and ^{30}Mg which is not. The shape coexisting spherical 0_2^+ state shown there was recently discovered [Wim10b]. So far the borders of the Island of Inversion at $N = 20$ are not exactly known. Figure 1.4 shows a part of the nuclear chart. Nuclei which are known to be inside the Island of Inversion and the nuclei produced in the experiment discussed in this thesis are marked. The results of this experiment will be compared to a SDPF-MU shell model calculation [Uts12] using
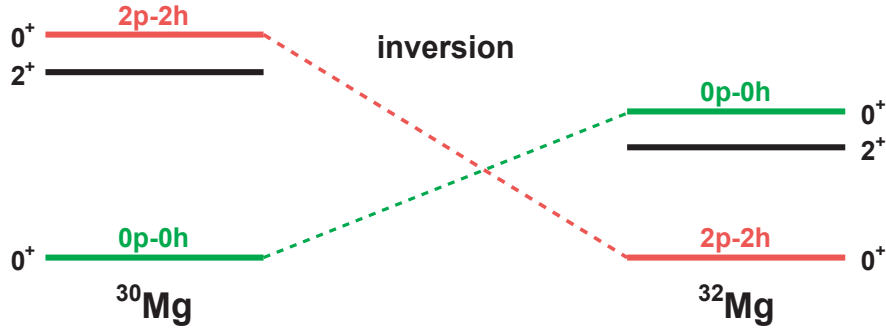
Figure 1.3: Comparison of level schemes of ^{30}Mg and ^{32}Mg. While ^{30}Mg has a spherical 0p-0h ground state and a deformed excited 2p-2h 0^+ state the order is inverted in ^{32}Mg making it a member of the Island of Inversion. Adopted from [Wim10a].
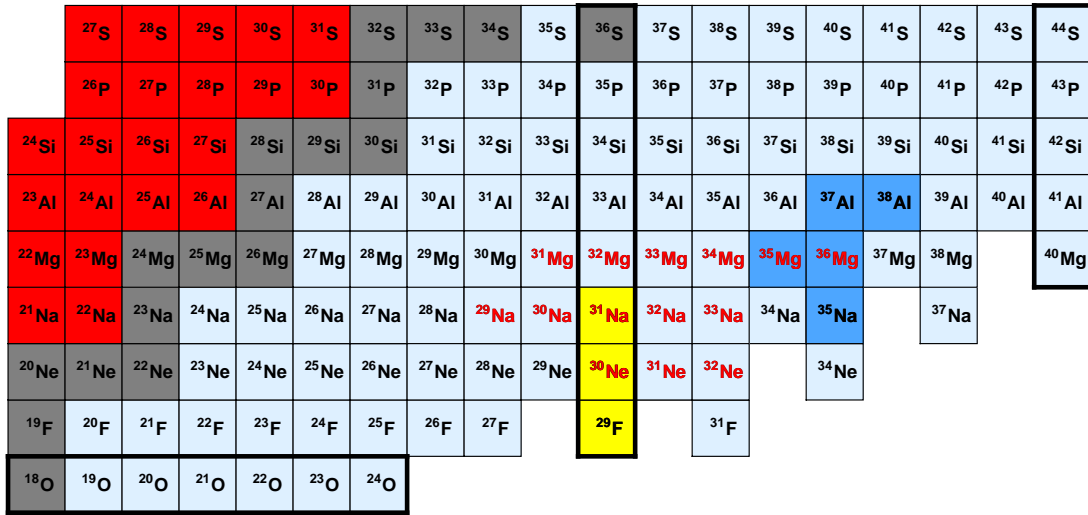
Figure 1.4: Part of the nuclear chart. The thick lines indicate the classic magic shell closures at $Z = 8$ and $N = 20$ and 28. The nuclei produced in this experiment are marked in yellow (^{30}Ne setting) and blue (^{36}Mg setting). Nuclei known to be inside the Island of Inversion are marked with a red font.

a Hamiltonian based on the V_{MU} interaction, which includes the tensor force.

1.1 Beta decay

Besides direct reactions like nucleon transfer reactions or Coulomb excitation, decay spectroscopy is an important method to investigate the nuclear structure (of exotic nuclei). Observables like the β decay half-life of a nucleus, the branching ratios to the different levels in the daughter nucleus and the energy available for the decay Q_β provide insights in the nuclear structure. The most important aspects of the β decay

will be introduced in this section.

At the β^--decay of a nucleus $^A Z$ with the nucleon number A and proton number Z

$$^A Z \to {}^A(Z+1) + e^- + \overline{\nu}_e \tag{1.2}$$

a neutron is transformed into a proton while emitting an electron and an anti-neutrino. There are two different decay modes:

- Fermi decay: The anti-neutrino and the electron are emitted with antiparallel spins. The Fermi strength B_F can be written as

$$B_F = |\langle \psi_f | \tau_\pm | \psi_i \rangle|^2. \tag{1.3}$$

  ψ_i and ψ_f are the wave functions of the initial and final state, respectively. The isospin operator $\tau_\pm$ changes the z-component of the isospin. The selection rules for an allowed Fermi decay are: No change of nuclear spin $\Delta I = 0$, no change of orbital angular momentum $\Delta L = 0$, no change of isospin $\Delta T = 0$ and no parity change. As the isospin does not change, only the transition to an isobaric analogue state is possible for a Fermi decay.

- Gamow-Teller decay: The anti-neutrino and the electron are emitted with parallel spins. The Gamow-Teller (GT) strength B_{GT} can be written as

$$B_{GT} = |\langle \psi_f | \vec{\sigma} \tau_\pm | \psi_i \rangle|^2. \tag{1.4}$$

  $\vec{\sigma}$ changes the spin of the converted nucleon and the isospin operator $\tau_\pm$ changes the z-component of the isospin. The selection rules for an allowed GT decay are: $\Delta I = 0$ or 1, $\Delta L = 0$, $\Delta T = 0$ or 1, no parity change and a $0^+ \to 0^+$ transition is not allowed.

If allowed Fermi or GT decays are not possible due to a change of parity or differences of the nuclear spin of the initial and the final state, so called "forbidden" decays which have a smaller transition rate are the only possibility for the decay. They are classified by their degree of forbiddenness which corresponds to the orbital angular momentum l of the electron and anti-neutrino relative to the nucleus:

- First forbidden ($l = 1$): $\Delta I = 0$ or 1 and parity change.

- First unique forbidden ($l = 1$): $\Delta I = 2$ and parity change.

- Second forbidden ($l = 2$): $\Delta I = 2$ or 3 and no parity change.

- Third forbidden ($l = 3$): $\Delta I = 3$ or 4 and parity change.

The half-lives (transition rates) of β decaying nuclei strongly depend on the energy that is available for the decay. To get information about the nuclear structure the comparative half-life $\log(f t_i)$ for the decay from the ground state of the mother nucleus to a specific state i with an excitation energy E_i in the daughter nucleus can be used. It consists of two parameters:

- The Fermi integral $f(Z', E_0)$ which depends on the nuclear charge Z' of the daughter nucleus and the energy available for this transition $E_0 = Q_\beta - E_i$. It corresponds to the available phase space for the decay.

- The partial half-life $t_i = t_{1/2}/P_i$ with the β decay half-life $t_{1/2}$ and the branching ratio P_i to the state i.

With Fermi's theory of the β decay [Fer34] it can be rewritten as

$$\log(ft) = \log\left(\frac{2\ln(2)\pi^3\hbar^7}{g^2 m_e^5 c^4 |M_{fi}|^2}\right) \tag{1.5}$$

with g being the strength of the weak interaction and M_{fi} the nuclear matrix element of the transition [Kra87]. This matrix element

$$|M_{fi}|^2 = g_V^2 \cdot B_F + g_{AV}^2 \cdot B_{GT} \tag{1.6}$$

depends on the Fermi and Gamow-Teller strength B_F and B_{GT} and the coupling constants for the vector current g_V and the axial-vector current g_{AV}.

Consequently the $\log(ft)$ value is only sensitive to the wave functions of the initial and final states $|\psi_i\rangle$ and $|\psi_f\rangle$ as the available phase space is taken into account. It can provide information of the structure of these states. As shown in figure 1.5 the $\log(ft)$ values depend on the classification of the transition. Consequently by measuring the
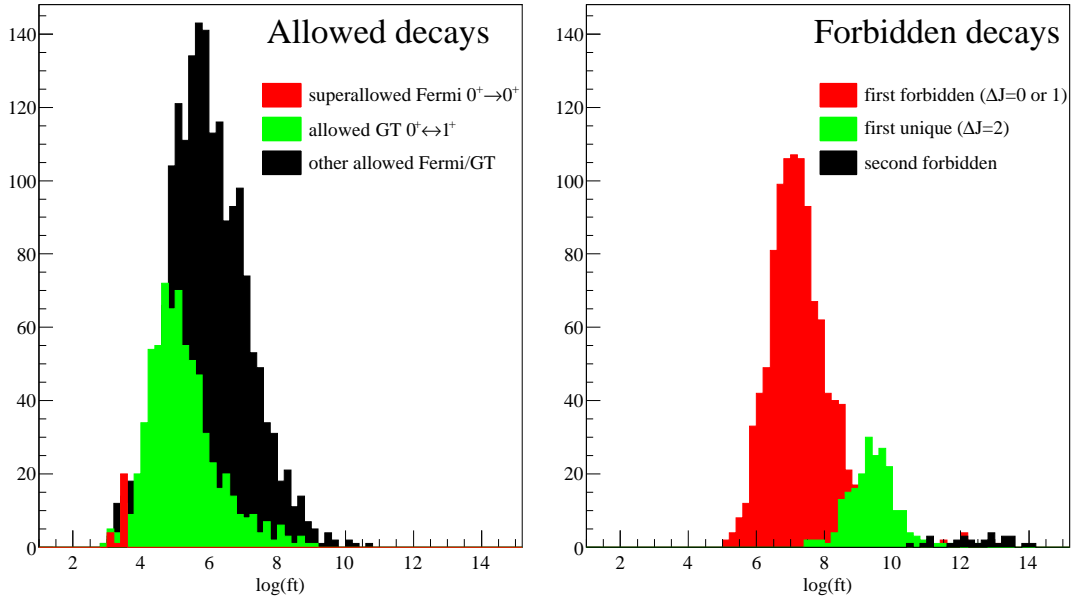

Figure 1.5: Distribution of experimental $\log(ft)$ values across the nuclear chart. Allowed decays are shown in the left histogram and forbidden decays in the right histogram. The data were taken from [Sin98].

$\log(ft)$ value of a specific transition its degree of forbiddenness can be estimated. This method will be used in chapter 5 to give a tentative spin and parity assignment for the levels populated by β decay.

Beta-delayed neutron emission

The β^- decay of a nucleus ^AZ either populates the ground state of the daughter nucleus $^A(Z+1)$ or an excited state, which decays by the emission of γ-rays or conversion electrons to the ground state. An additional decay mode for very neutron-rich nuclei is the β-delayed neutron emission. This process is only possible if the β^--decay populates the daughter nucleus in a state with an excitation energy larger than the neutron separation energy S_n. The neutron separation energy S_n of a nucleus ^AZ is defined as the difference of the binding energy (BE) of ^AZ and the isotope ^{A-1}Z with one neutron less:

$$S_n\left(^AZ\right) = BE\left(^AZ\right) - BE\left(^{A-1}Z\right) = \left[m\left(^{A-1}Z\right) + m(n) - m\left(^AZ\right)\right]c^2 \qquad (1.7)$$

If the energy of the populated level is even larger than the two-neutron separation energy S_{2n} the nucleus $^A(Z+1)$ may emit two neutrons.

$$S_{2n}\left(^AZ\right) = BE\left(^AZ\right) - BE\left(^{A-2}Z\right) = \left[m\left(^{A-2}Z\right) + 2m(n) - m\left(^AZ\right)\right]c^2 \qquad (1.8)$$

For nuclei near the valley of stability the β end-point energy Q_β is smaller than the neutron separation energy S_n. Therefore β-delayed neutron emission is not possible for these nuclei. Going "south-east" in the nuclear chart from the valley of stability towards extreme neutron-rich nuclei the general trend is that the β end-point energy Q_β increases (because the slope of the mass parabola for isobaric nuclei derived from the semi-empirical Bethe-Weizsäcker mass formula [Wei35] gets steeper) while the neutron separation energy S_n decreases. Consequently β-delayed neutron emission is possible for neutron-rich nuclei if Q_β is larger than S_n.

A schematic illustration of the β-delayed neutron emission can be seen in figure 1.6. The maximum energy available for the β-delayed one-neutron or two-neutron emission is the difference $(Q_\beta - S_n)$ or $(Q_\beta - S_{2n})$, respectively. As will be discussed further in chapter 2 only β- and γ-rays can be measured with the detector setup used in this experiment. Consequently it was not possible to directly distinguish between a "normal" β decay and a β-n or β-2n decay. The only way to tag a β-n or β-2n decay in the current experiment is the β-delayed emission of a γ-ray which can be attributed to the β-n or β-2n daughter nucleus. However, as very neutron-rich nuclei are investigated most γ-transitions in the daughter nuclei are not known and it is one of the aims of this experiment to measure new transitions. Consequently, the assignment of new γ-transitions will be done with the help of β-γ-γ coincidences and a comparison to state of the art shell model calculations.
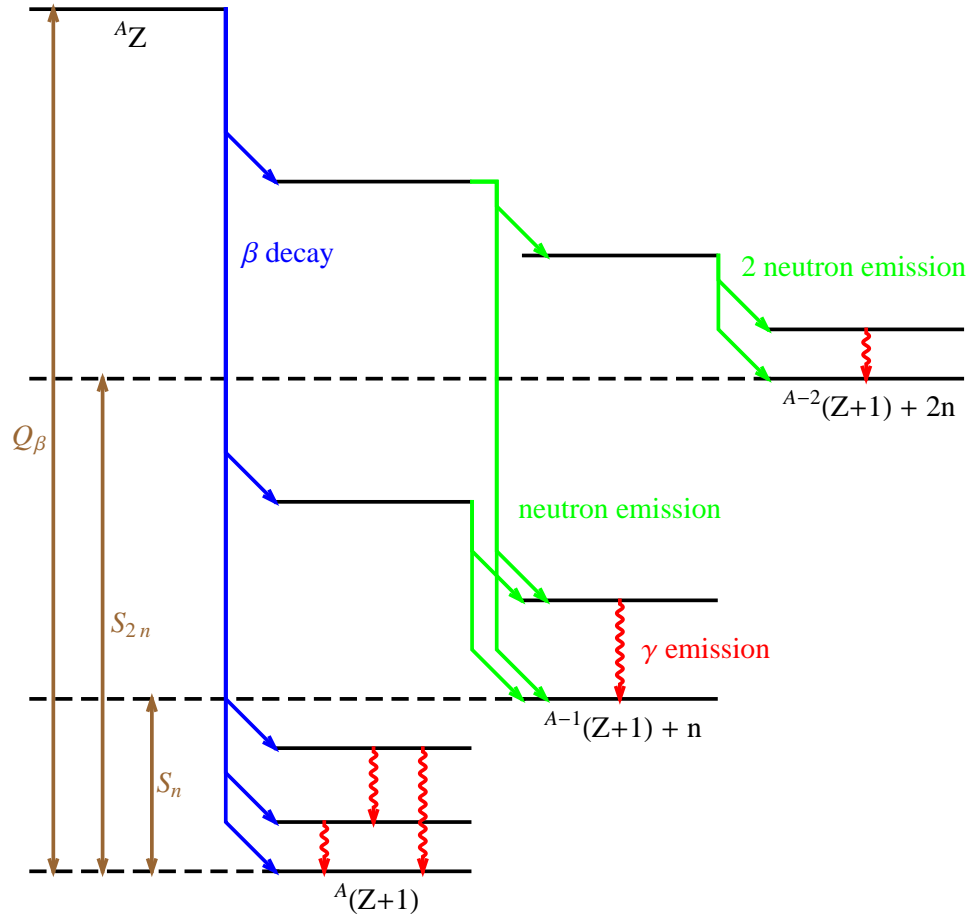
Figure 1.6: Schematic illustration of the β decay process with delayed neutrons. At the β decay of very neutron-rich nuclei the end-point energy Q_β is large. One or two neutrons can be emitted if the β decay populates levels in the daughter nucleus with an excitation energy larger than the one-neutron separation energy S_n or two-neutron separation energy S_{2n}, respectively.

1.2 Outline of this thesis

The nuclear structure of nuclei in the vicinity of the "Island of Inversion" was investigated with the experiment discussed in this thesis. Decay spectroscopy of the nuclei which are marked in yellow (^{30}Ne setting) and blue (^{36}Mg setting) in figure 1.4 was performed. The experimental details are given in chapter 2, the data analysis is explained in chapter 3 and the results and their interpretation are discussed in the chapters 4 and 5. A summary and an outlook are given in chapter 6.

Chapter 2

Experimental Setup

The experiment discussed in this thesis was performed in fall 2010 at the Radioactive Isotope Beam Factory (RIBF) [Yan07] at the RIKEN Nishina Center for Accelerator-Based Science which is located at Wako (Saitama Prefecture), Japan. Decay properties of neutron-rich nuclei in the area around ^{30}Ne and ^{36}Mg were investigated. These nuclei were produced by relativistic projectile fragmentation. Exotic relativistic nuclei from the primary target were separated and identified in flight using the BigRIPS spectrometer (see section 2.2) and stopped in an implantation detector to perform decay spectroscopy (see section 2.3). This chapter gives an overview of the experimental setup.

2.1 The RIBF accelerators and cyclotrons

A ^{48}Ca heavy ion beam was accelerated up to energies of $E = 345A$ MeV by several accelerators and stripping stages. From the electron cyclotron resonance (ECR) ion source it was injected with a charge state $Q = 10^+$ into the RIKEN Heavy-ion Linac (RILAC). Then it passed three charge strippers and four cyclotrons in the following order: A charge stripper (STP1, $Q = 16^+$), the RIKEN Ring Cyclotron (RRC) with a K value[1] of $K = 540$ MeV, a charge stripper (STP2, $Q = 20^+$), the fixed-frequency Ring Cyclotron (fRC) with $K = 570$ MeV, a charge stripper (STP3), the Intermediate-stage Ring Cyclotron (IRC) with $K = 980$ MeV and the Superconducting Ring Cyclotron (SRC) with $K = 2600$ MeV. The primary beam delivered by the SRC had an average intensity of $I = 70$ pnA[2]. A schematic overview of the RIBF with its accelerators and cyclotrons can been seen in figure 2.1.

2.2 Separation and identification

Neutron-rich nuclei were produced via relativistic projectile fragmentation of ^{48}Ca^{20+} projectiles from the SRC with an energy $E = 345A$ MeV, incident on a rotating

---

[1] K values represent the energy of a proton beam using the maximum magnetic rigidity of the cyclotron.

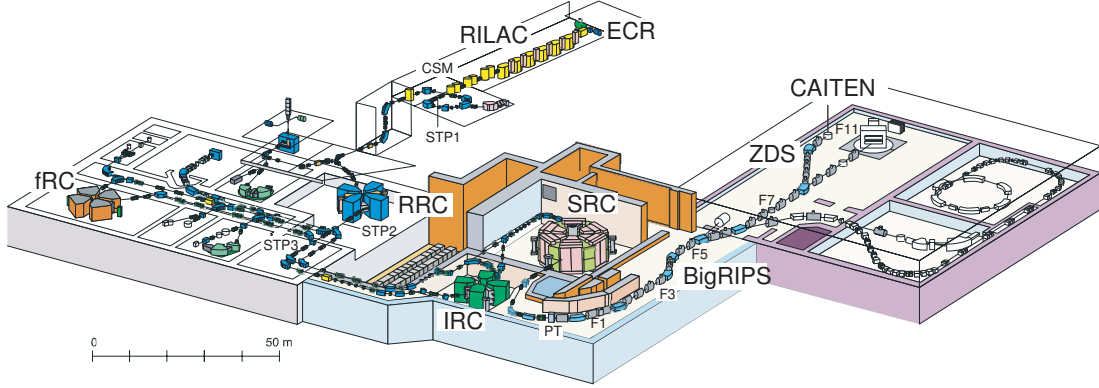[2] particle nanoampere, 1 pnA = $6.25 \cdot 10^9$ particles per second

Figure 2.1: Overview of the Radioactive Isotope Beam Factory (RIBF). In the experiment the linear accelerator RILAC and the four cyclotrons RRC, fRC, IRC and SRC were used in a row to accelerate a ^{48}Ca beam up to $345A$ MeV. It was fragmented in the primary beryllium target (PT). The resulting cocktail beam was separated and identified in the BigRIPS fragment separator. After the zero-degree spectrometer (ZDS) the fragments were implanted in the CAITEN detector. Modified illustration from [Got07].

beryllium target with a thickness of 15 mm which corresponds to an areal density of $2.8\,\mathrm{g/cm^2}$.

The nuclei of interest were separated and identified with the BigRIPS spectrometer [Kub03]. A schematic view of BigRIPS can be seen in figure 2.2. The separation of background fragments in the cocktail beam was done with the first stage of the BigRIPS fragment separator (F0 to F2). Two dipole magnets and an achromatic aluminum energy degrader located at the dispersive focus F1 were used to perform a $B\rho$-ΔE-$B\rho$ selection. The dipole magnets separate the beam with respect to the magnetic rigidity $B\rho$ and the transmission of the beam through a degrader results in an energy loss ΔE which depends on the nuclear charge Z of the transmitted fragment. The degrader had a median thickness of 15 mm and 10 mm for the ^{30}Ne and ^{36}Mg setting, respectively. The momentum acceptance was approximately $\pm 3\%$.

The second stage of BigRIPS (F3 to F7) was used to identify the transmitted fragmentation products using the ΔE-$B\rho$-velocity method. The energy loss ΔE of the ions was measured in a multi-sampling ionization chamber (MUSIC) located at F7. The magnetic rigidity $B\rho$ was determined from position measurements of parallel plate avalanche counters (PPAC) [Ohn08] at the achromatic focus F3, the dispersive focus F5 and the achromatic focus F7. The time of flight (TOF) was measured between two thin (200 μm) plastic scintillators at F3 and F7 separated by a flight path of 47 m.

With this information an unambiguous event-by-event identification of the fragments in (A, Z) is possible using:

$$B\rho = \frac{p}{Q} = \frac{m_0 \beta c}{\sqrt{1 - \beta^2}} \cdot \frac{A}{Q} \tag{2.1}$$

(βc) is the velocity of the ions, c the speed of light and m_0 the atomic mass unit. As
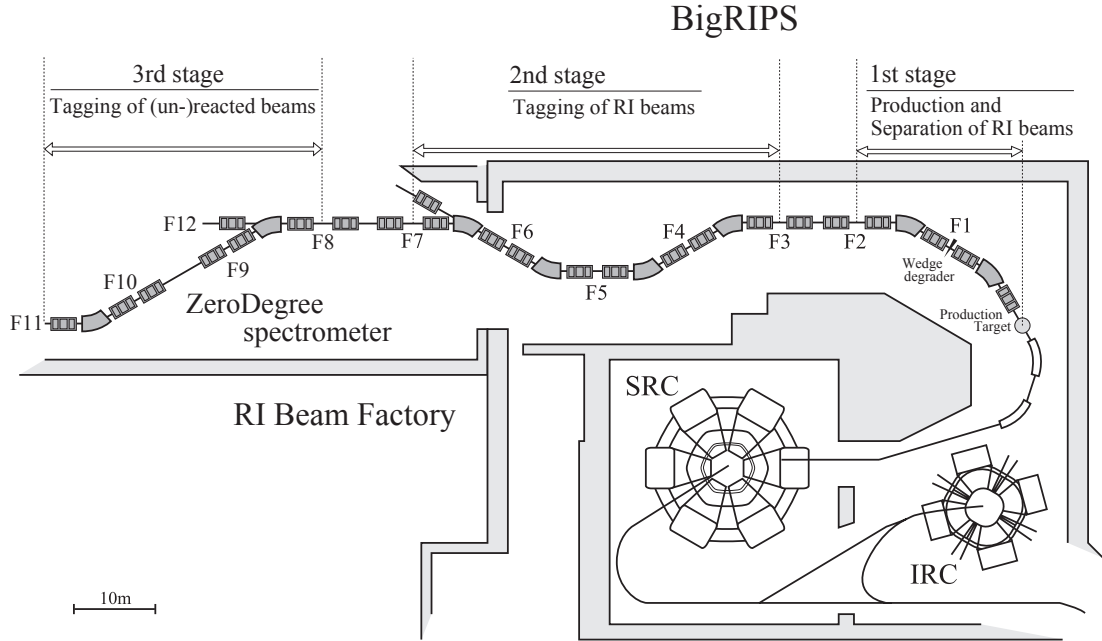
Figure 2.2: BigRIPS fragment separator and zero-degree spectrometer (ZDS). The focal planes are denoted by F1 to F12. The superconducting quadrupole triplet magnets and the room-temperature dipoles are shown schematically. The implantation detector CAITEN was placed at the end of the ZDS (F11). Picture adopted from [Aoi06].

$B\rho$ and the TOF are measured the mass over charge ratio A/Q can be derived. With precise energy loss measurements and parameterizations $f(Z, \beta)$ which are available for the energy region discussed here [Kim05], the identification for the nuclear charge Z could be performed.

$$\Delta E = f(Z, \beta) \tag{2.2}$$

The beam was shared between two experiments: The β decay experiment which is the subject of this thesis and an experiment studying direct reactions [Lee11]. The latter required a secondary target (dependent on the run: $2.54\,\mathrm{g/cm^2}$ C, $2.13\,\mathrm{g/cm^2}$ CH$_2$, $3.37\,\mathrm{g/cm^2}$ Pb). It was placed at the focal plane F8 and was surrounded by the DALI2 NaI(Tl) γ-ray detector [Tak03, Tak09]. Few nucleon removal reactions and Coulomb excitations were studied in that experiment.

Therefore behind the secondary target another identification of the beam fragments is performed in the zero-degree spectrometer (ZDS). The $\Delta E - B\rho - $ velocity method was applied again (F8 to F11): The energy loss ΔE of the ions was measured in a MUSIC located at the final focus F11, the $B\rho$ was determined from position measurements of PPAC detectors at the focal planes F9 and F11 and the TOF was measured between two thin ($200\,\mu$m) plastic scintillators at F8 and F11 with a flight path of $37\,\mathrm{m}$ in between.
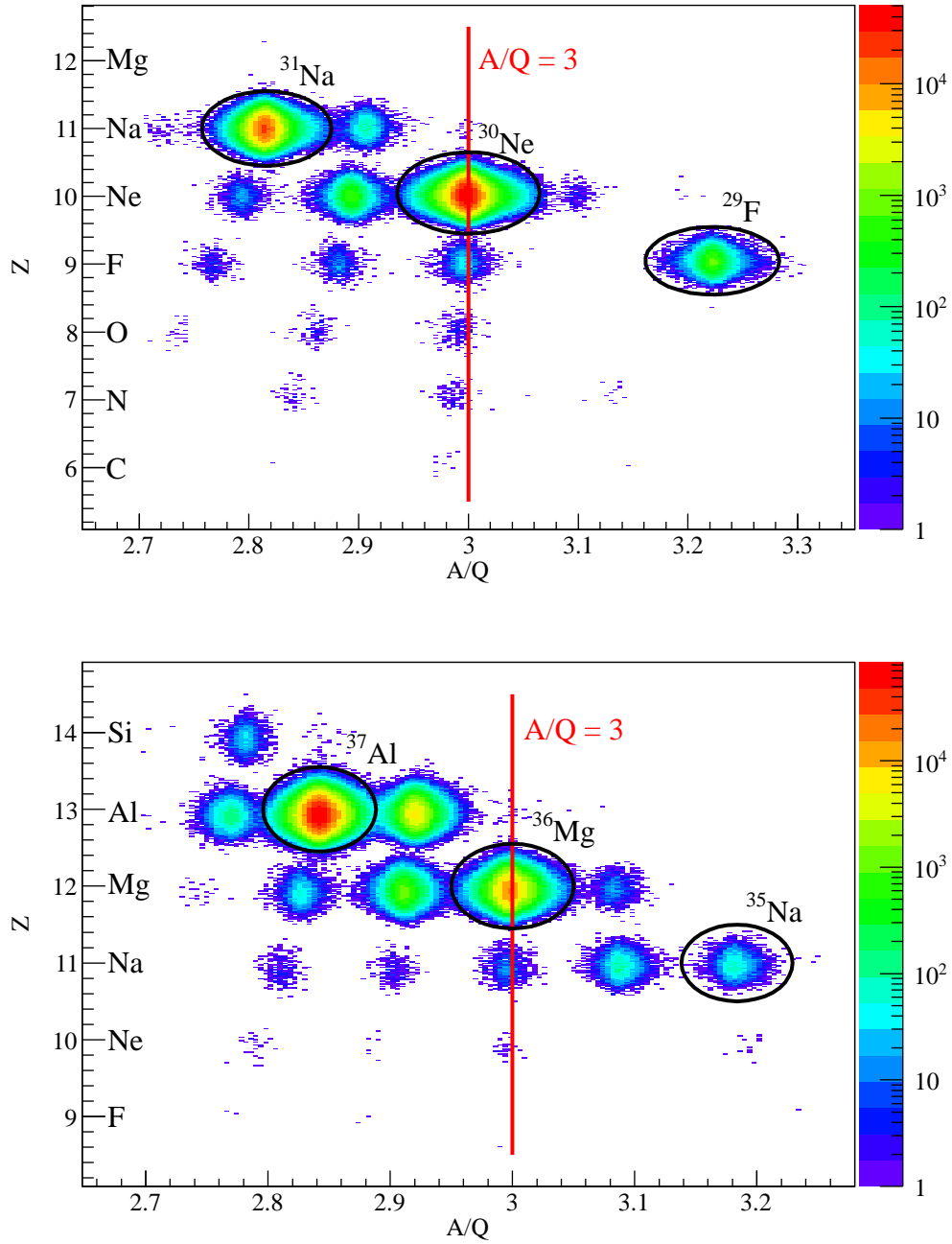
Figure 2.3: Particle identification in the ZDS between F8 and F11. The mass resolution of the ZDS is $\Delta A = 0.23$ (FWHM) and the nuclear charge resolution is $\Delta Z = 0.30$ (FWHM).
Top: ^{30}Ne setting. $N = 20$ isotones are marked in black.
Bottom: ^{36}Mg setting. $N = 24$ isotones are marked in black.

The mass resolution was $\Delta A = 0.23$ (FWHM[3]) and the nuclear charge resolution was $\Delta Z = 0.30$ (FWHM). The result of the particle identification of the ZDS can be seen in figure 2.3.

To be able to modify and control the implantation depth of the ions in the CAITEN scintillator, a remotely controlled variable thickness aluminum degrader was placed at F11 in a distance of 1 m upstream of the implantation detector.

2.3 Implantation and beta detector CAITEN

CAITEN (Cylindrical Active Implantation Target for Exotic Nuclei) is a highly segmented implantation and β detector. It can handle high implantation rates up to several kHz of heavy ion cocktail beams and is able to measure half-lives in the range of milliseconds up to several hundreds of milliseconds. It consists of two subsystems: A segmented movable hollow-cylindrical-shape plastic scintillator and a stationary ring of 24 position-sensitive photomultiplier tubes (PSPMTs) arranged on a ring inside the scintillator at the height of the beam line. Implantations and decays are detected with position and time information. Similar to a tape station the scintillator can be moved across the PSPMTs to reduce background decays. Only with this motion it is possible to handle implantation rates $R > 200\,\mathrm{Hz}$. The implanted nuclides are transported away from the implantation position and further implantations can be detected at this position. The decays of the implanted nuclides are detected at a different position and have to be correlated with the implantations in time and space. This correlation will be introduced in section 3.1.2. A schematic view of the CAITEN components is shown
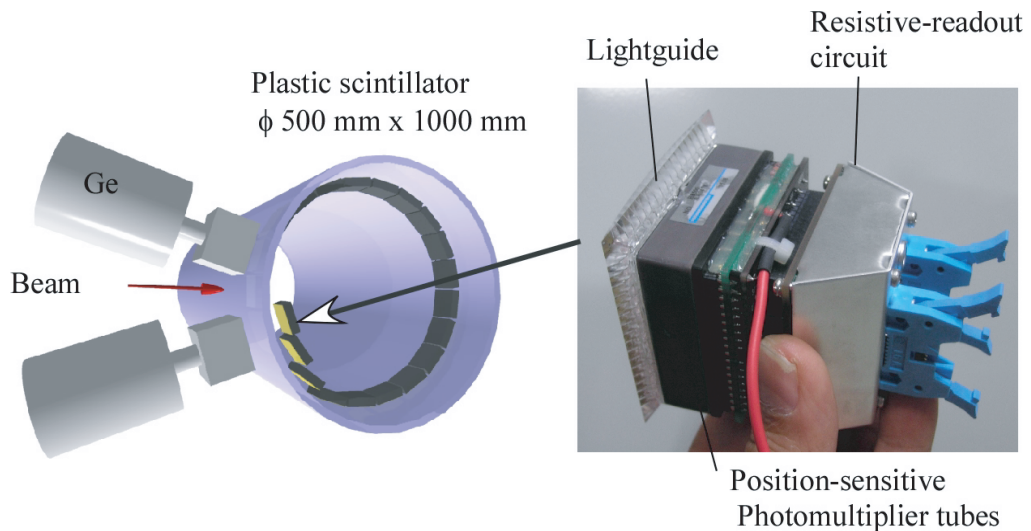
---

[3]FWHM: Full width at half maximum

Figure 2.4: *Left:* Schematic Figure of CAITEN. *Right:* Photo of a sensor module with light guide, position sensitive PMT and electronics. Adopted from [Nis07].

in the figures 2.4 and 2.5. The overall height of CAITEN is about $3\,m$ because of the sliding mechanism of the cylindrical scintillator in vertical direction.

2.3.1 Scintillator

The scintillator barrel has an outer diameter of $500\,mm$, a height of $1000\,mm$ and a thickness of $20\,mm$. It is highly segmented and is made of $4 \cdot 10^4$ REXON RP-408 [Rex] plastic pixels of the size $6 \times 6 \times 20\,mm^3$. They are separated from each other by a thin mesh made from aluminum sheets.

To reduce background events the scintillator can be rotated and moved axially with a constant velocity in vertical direction which results in a helix-shaped motion. This motion has the advantage, that the collected radioactivity in the scintillator from daughters, granddaughters and further decay generations of implanted ions is transported away from the light-collecting PSPMTs. Rotation frequencies of 20 and $40\,rpm^4$ which correspond to velocities of 500 and $1000\,mm/s$ on the surface of the scintillator were used for the ^{36}Mg and ^{30}Ne run, respectively. In addition to this fast axial motion long-lived decay products ($T_{1/2} > 200\,ms$) can be removed from the active area of the PSPMTs with a vertical movement of $2\,mm/s$.

Because of the fast motion of the scintillator, a direct optical connection of the scintillator and the stationary PSPMTs is not possible: There is an air gap of $\Delta z \approx 3\,mm$ between the scintillator and the light guides of the PSPMTs. The rotation has to be taken into account for the analysis because a correlation time of $150\,ms$ corresponds to a horizontal shift of the implantation and decay position of 75 and $150\,mm$ for the ^{36}Mg and ^{30}Ne setting, respectively. As this shift is smaller than 3 times the width of a PSPMT, it is not necessary to read out all the PSPMTs. Thus to save read out channels, only the PSPMTs numbered 0, 1, 2, 3 and 4 are read out, as shown in figure 2.5. For the data analysis the vertical movement is neglected because the correlation time of implantation and decay events is smaller than $150\,ms$ which means that the vertical shift between the implantation and decay position is smaller than $0.3\,mm$ and consequently much smaller than the position resolution of CAITEN $\Delta x = 8\,mm$ (FWHM).

2.3.2 Position-sensitive photomultiplier tubes (PSPMTs)

The light detection of the scintillator pixels is done by Hamamatsu H8500 PSPMTs [Ham]. To collect the emitted scintillation light efficiently, the PSPMTs are coupled to segmented light-guides. The PSPMTs are 64-fold segmented with a pixel size of $5.8 \times 5.8mm^2$. To reduce the number of readout channels 8 pixels of a PSPMT were connected via a horizontal resistor chain ($150\,\Omega$ per resistor). There are only two readout channels (right and left channel) for one resistor chain which is fed by 8 PSPMT anodes. In total there are 16 readout channels for one PSPMT (see figure 2.6).

The PSPMT Nr. 0 is at the beam spot position and is used for detecting implantations and decays. There is a large difference in energy deposited by an implantation (several GeVs) and a decay (up to several MeVs) event. Therefore the signal of PSPMT Nr. 0

---

^{4}rpm: Revolutions per minute
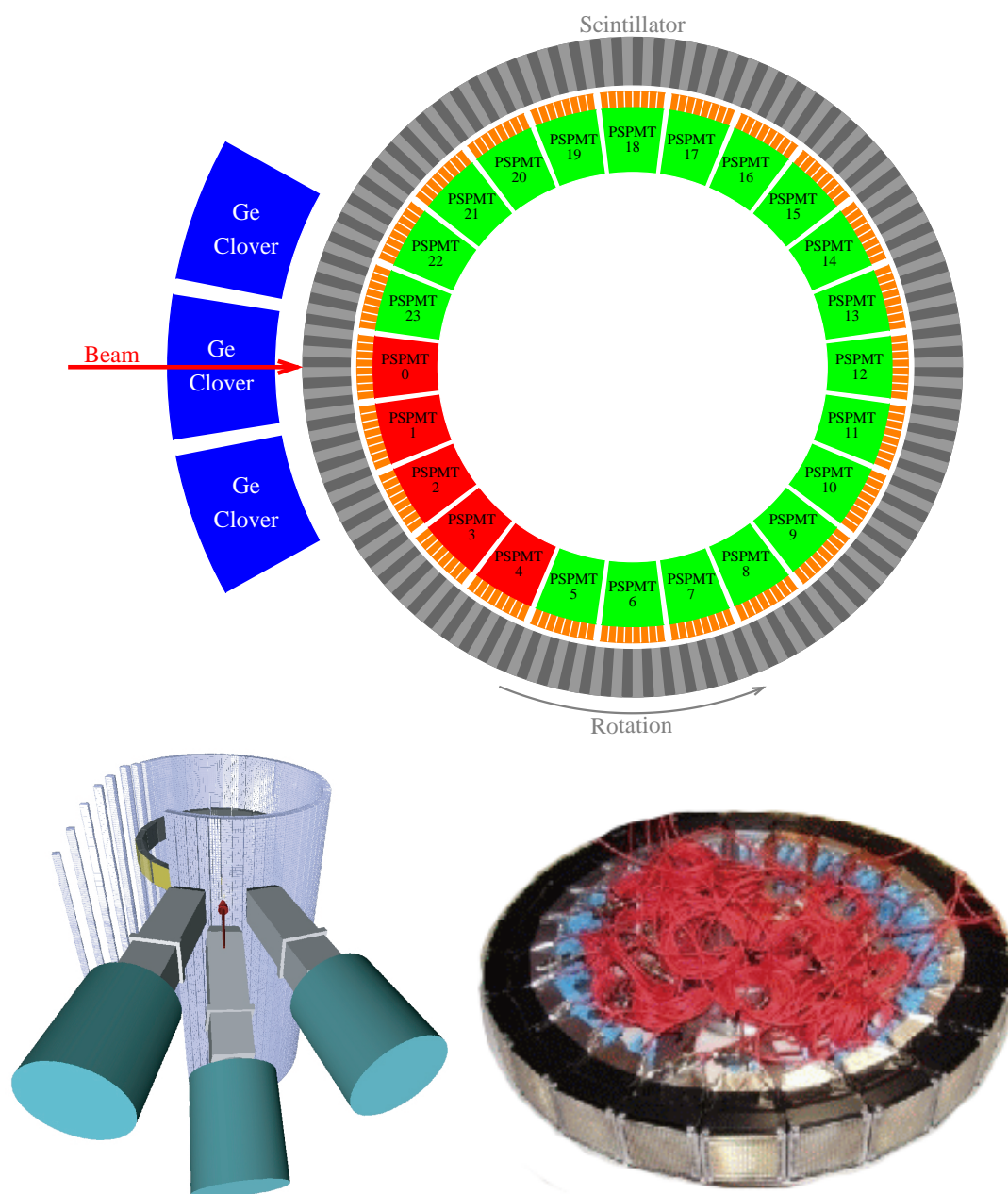
Figure 2.5: *Top:* Schematic drawing of the components of CAITEN (view from the top). The segmented scintillator is plotted in gray, the PSPMTs which were read out in red, the PSPMTs which were not read out in green, the light guides of the PSPMTs in orange and the HP-germanium clover detectors in blue. *Bottom left:* CAITEN setup in the view from the beam direction. The red arrow corresponds to the beam direction. The scintillator pixels are shown in light blue, the PSPMTs in yellow and the clover detectors in gray. *Bottom right:* Photo of the 24 PSPMTs to be placed inside CAITEN.
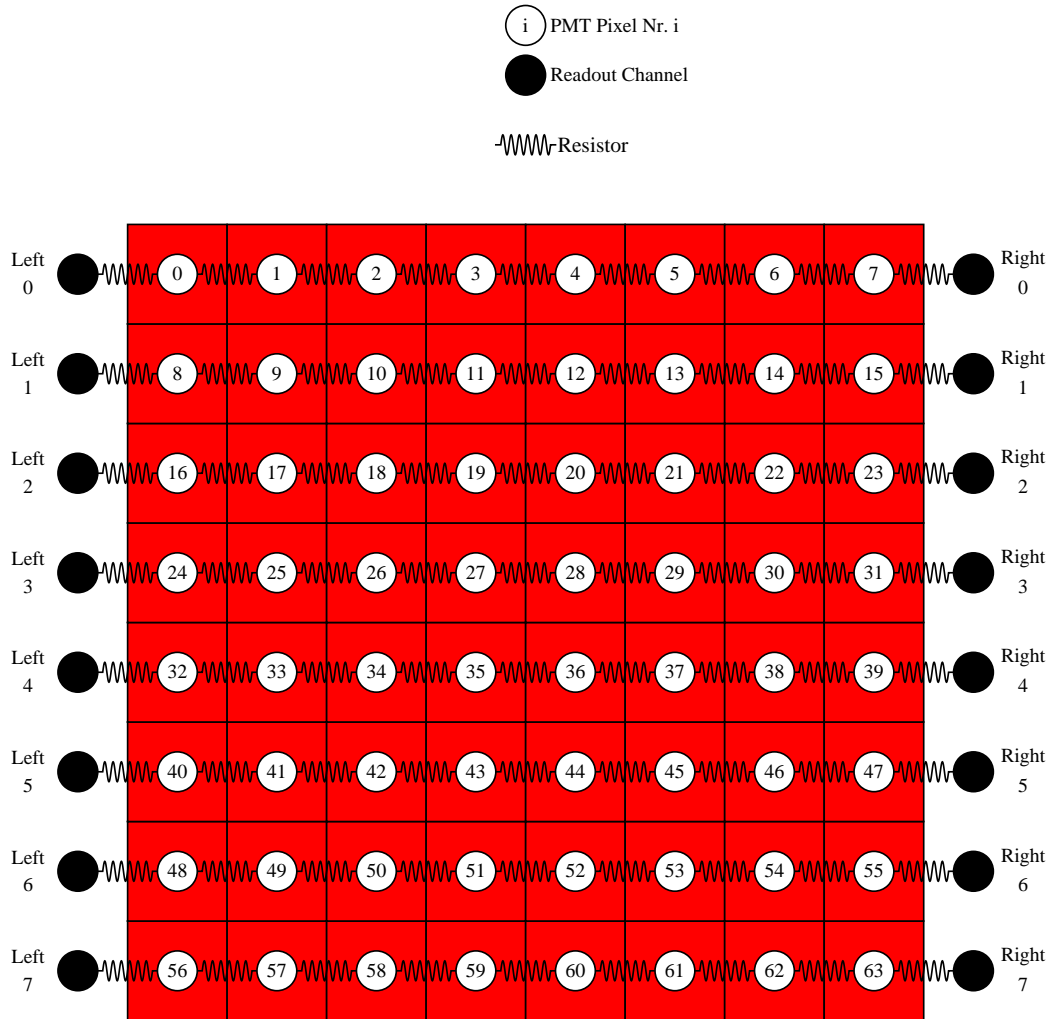
Figure 2.6: Readout of a 64-fold segmented PSPMT: 8 horizontal pixels of the PSPMT are connected via a resistor chain (each resistor has $R = 150\,\Omega$) to reduce the number of readout channels from 64 to 16. The splitting of the charge in the left and right channels of the resistor chain is used for the reconstruction of the horizontal position of a decay or implantation event. Details of the position calibration can be found in chapter 3.

is split in a high gain readout branch for decays and a low gain readout branch for implantations. The PSPMTs Nr. 1-4 detect decays but no implantations, so they are only connected to a high gain readout branch.

2.4 Germanium detectors

To detect gamma radiation, three Canberra EURISYS HP-germanium clover detectors [Can] were used. They were placed close to the implantation position of the CAITEN detector facing the scintillator surface (see figure 2.5). The distance from the surface of the scintillator to the clover detectors was less than 5 mm. With these detectors it is possible to search for β-delayed gamma-ray emission of decay products. The clover detectors consist of 4 germanium crystals, each (see figure 2.7). The single crystals have a diameter of 50 mm and a length of 70 mm. The nominal energy resolution is $\Delta E_\gamma = 2.1$ keV (FWHM) at a gamma-ray energy of $E_\gamma = 1.33$ MeV and $\Delta E_\gamma = 1.05$ keV (FWHM) at $E_\gamma = 122$ keV. In add-back mode (details can be found in section 3.2), the nominal energy resolution is $\Delta E_\gamma = 2.3$ keV (FWHM) at $E_\gamma = 1.33$ MeV [Can]. In the present experiment the energy resolution in add-back mode was $\Delta E_\gamma = 3.0$ keV (FWHM) at $E_\gamma = 1.33$ MeV

A photo of the complete decay spectroscopy setup is shown in the figure 2.8.
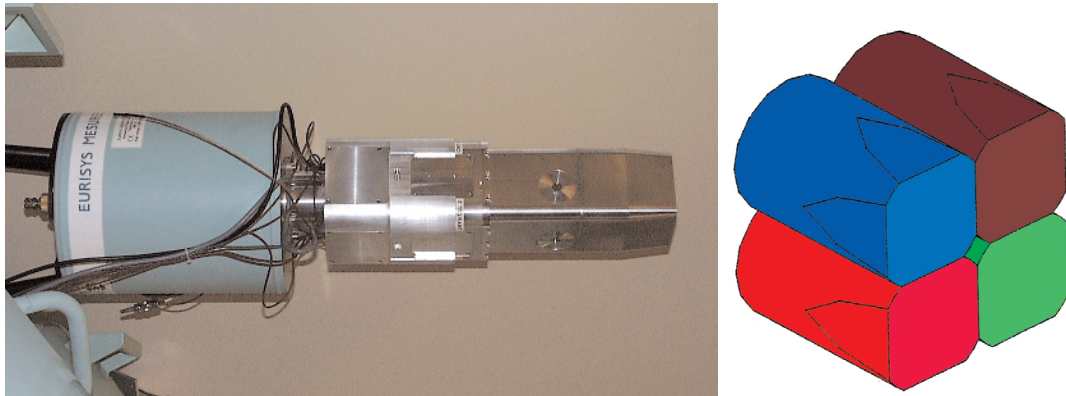
Figure 2.7: *Left:* Photo of a clover detector with its liquid nitrogen dewar. *Right:* Schematic view of germanium crystals inside a clover detector. Adopted from [Can].
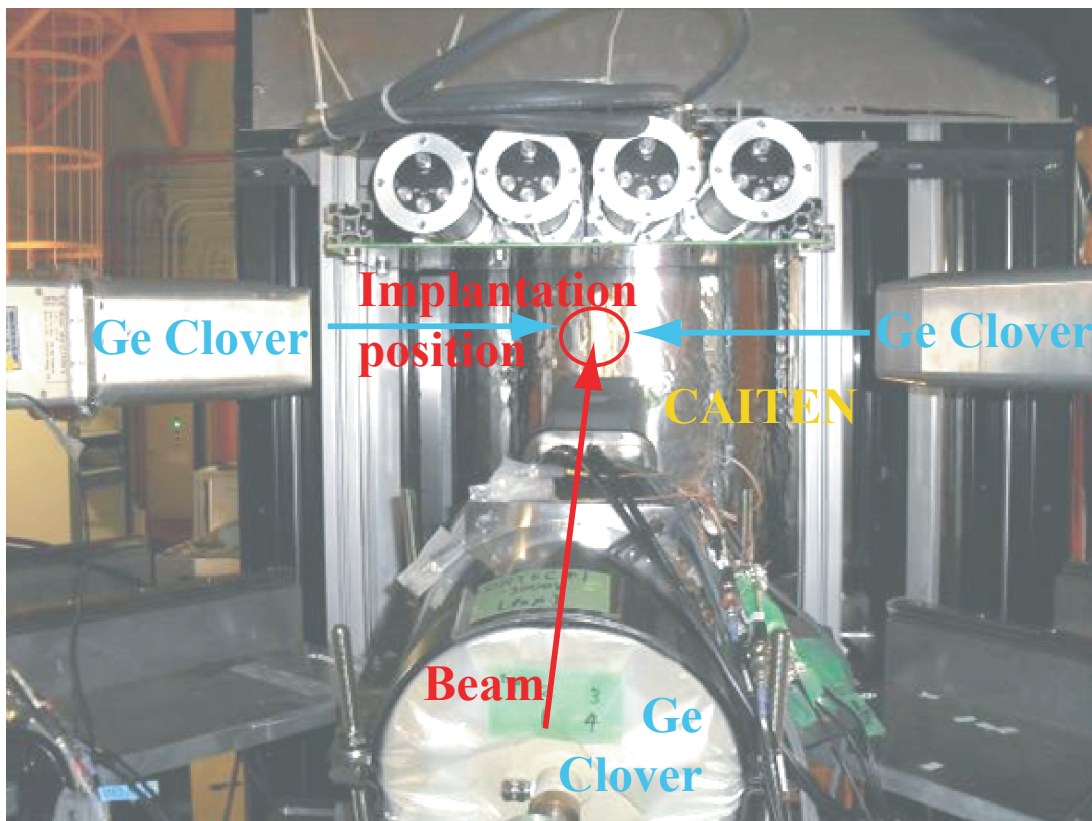
Figure 2.8: Photo of the complete decay spectroscopy setup in beam direction. The CAITEN scintillator is covered by a thin aluminum foil at the surface. To protect the scintillator from ambient light a black light-tight plastic sheet surrounds the CAITEN setup. This sheet is removed here to have a better view of the scintillator. During the measurement the clover detectors are moved closer to the implantation position than shown here.

Chapter 3

Data Analysis

In this chapter the methods used for the data analysis of the CAITEN detector The particle identification (PID) will not be discussed further as the standard method for the identification with BigRIPS and ZDS was used which was already introduced in section 2.2. The high resolution results of the identification are shown in figure 2.3. Implantations in the CAITEN detector and the PID are correlated with time stamps: The PID data acquisition and the CAITEN data acquisition are independent and both of them put a time stamp with a precision of $10\,\text{ns}$ to each event. The two time stamps are compared and if there is a match of a particle identification and an implantation event, these events get correlated. In this way each implantation event can be associated with an identified particle.

3.1 CAITEN detector

3.1.1 Position calibration

One of the issues for the position calibration is the crosstalk of light which is emitted by the plastic scintillator of CAITEN. Due to the air gap of $3\,\text{mm}$ between the scintillator and segmented light guides of the PSPMTs not only one pixel of a PSPMT detects the total amount of the emitted light but it is distributed among a few photomultiplier pixels. In addition, the scintillator pixels and segmented light guides are not aligned because of the movement of the scintillator. Consequently the position resolution becomes worse compared to a photomultiplier which is directly coupled via a light guide to a scintillator. The following methods are used to calibrate the position measurement.

Vertical calibration

For the determination of the vertical position of each PSPMT the following method is used: For each horizontal resistor chain of a PSPMT connecting a row of 8 pixels the value $Q_{\text{dep}} = \sqrt{Q_{\text{left}} \cdot Q_{\text{right}}}$ is evaluated. Q_{left} and Q_{right} are the electric charges which were detected by the two sides of a resistor chain (see subsection 2.3.2). The resistor chain with the highest value for Q_{dep} is selected to be the one where the decay or implantation appeared.

Horizontal calibration

A horizontal position calibration was carried out using a ^{90}Sr source that was fixed to the outer surface of the CAITEN scintillator rotating at a frequency of 40 rpm around the PSPMTs. The vertical velocity of the scintillator and the source was adjusted to 2 mm/s. From the timing information of the rotation and the vertical motion the exact position x_t of the source was known at all times. The measured (uncalibrated) horizontal position x_{measured} is calculated using the following formula:

$$x_{\text{measured}} = s \cdot \frac{Q_{\text{right}} - Q_{\text{left}}}{Q_{\text{right}} + Q_{\text{left}}} \tag{3.1}$$

Q_{right} and Q_{left} are the calibrated charges detected in the left and right channel, respectively. s is a scaling factor to match the size of the PSPMT.

With this information and the known position x_t a calibration was performed which depends on the following parameters:

- the time since the last rotation pulse t (a scaler gives a signal at each rotation) which determines the known position x_t,

- the PSPMT which detects the beta-particle PSPMT Nr.,

- the vertical position y which corresponds to the resistor chain which detects the largest amount of charge of an event (see subsection 2.3.2),

- the total amount of charge Q_{dep} which is deposited there,

- the measured (uncalibrated) position x_{measured}.

This leads to:

$$x_{\text{calibrated}} = x_{\text{measured}} + \Delta x(t, \text{PSPMT Nr.}, y, x_{\text{measured}}, Q_{\text{dep}}) \tag{3.2}$$

The 4 parameters PSPMT Nr., y, x_{measured} and Q_{dep} of the position correction Δx were binned. For each of these 4-dimensional bins Δx was determined by the shift of the mean value of x_{measured} from its nominal value x_t. The calibrated horizontal position is shown in figure 3.1. The average horizontal position resolution which results from the calibration is $\Delta x = 8$ mm (FWHM).

3.1.2 Correlation of implantations and decays

An important task in the analysis of the data is the correlation of implantations and decays. Due to the motion of the scintillator this correlation has to be done in time and space. The high implantation rate of ≈ 200 Hz leads to a significant amount of wrongly correlated events. To distinguish "real" correlations and random background correlations a background subtraction has to be performed. A correlation plot and the principle of the background subtraction are illustrated in figure 3.2: Here the time difference of an implantation and a decay is plotted against the position difference due
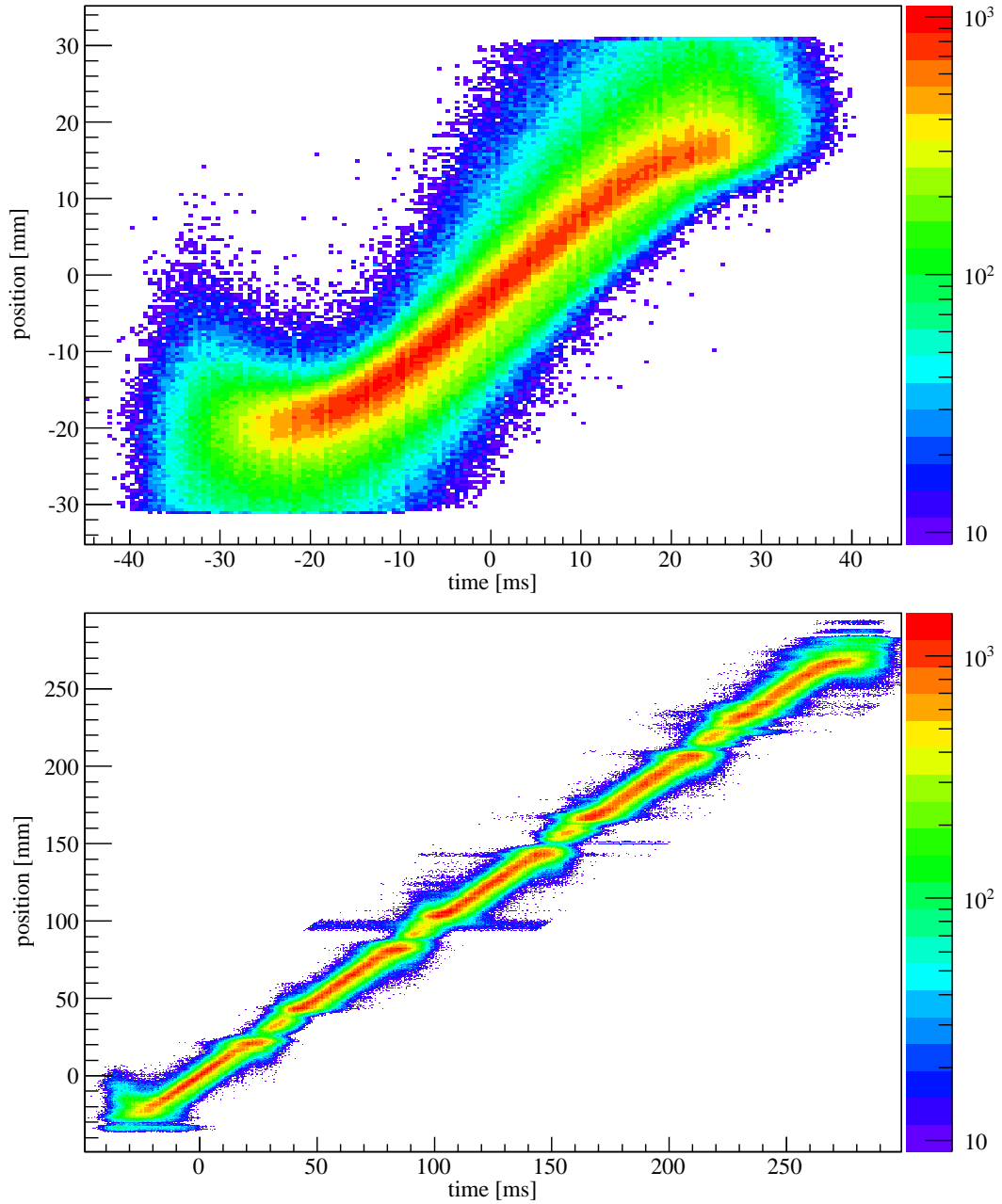
Figure 3.1: *Top:* Uncalibrated horizontal position of PSPMT Nr. 0 against the rotation time of the ^{90}Sr calibration source. *Bottom:* Calibrated horizontal position of all PSPMTs against the rotation time. The point at time $t = 0$ and position $x = 0$ corresponds to the center of PSPMT Nr. 0. The non-linearity caused by the resistor chain readout of the PSPMTs was corrected by the position calibration (see text for details). One can clearly see the positions of the five PSPMTs and the gaps in between.
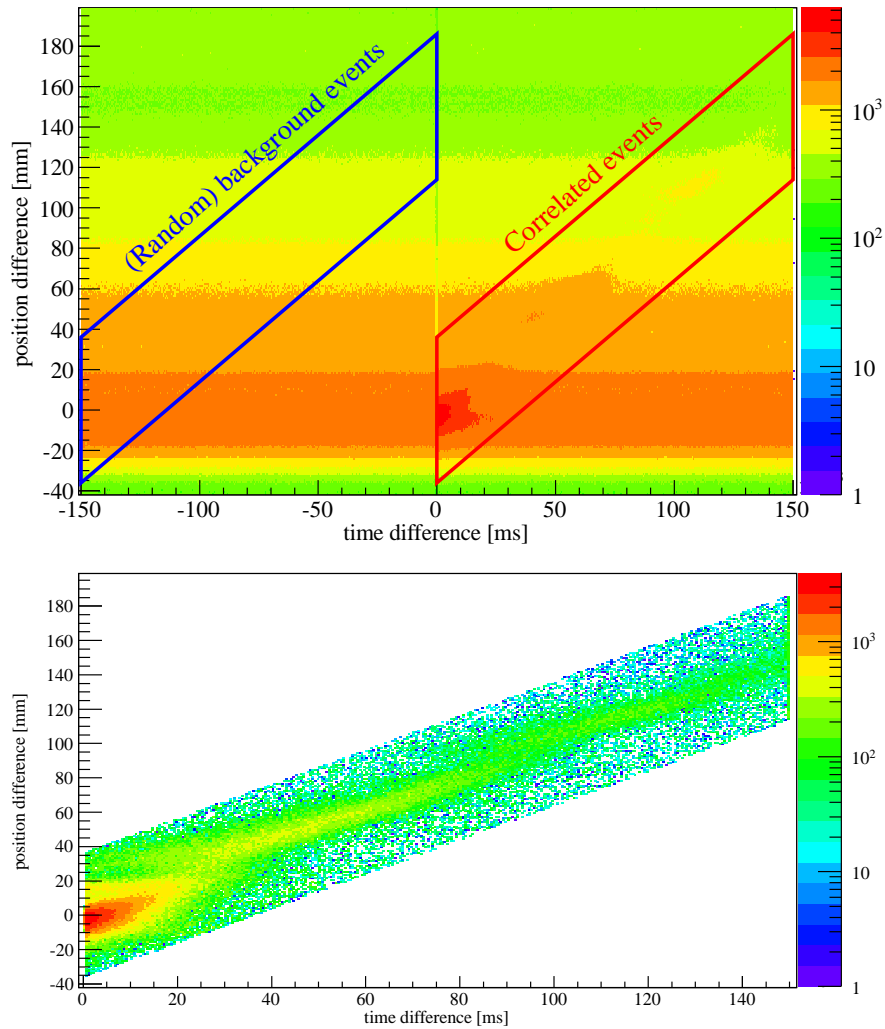
Figure 3.2: Position-time correlation of decays and implantations of ^{30}Ne. *Top:* 2D-correlation plot of all raw events. The time difference of an implantation and a decay is plotted along the x-axis while the position difference due to the rotation of the scintillator is plotted along the y-axis. The graphical cut on the right-hand side corresponds to correctly correlated events, the one on the left-hand side to (random) background events, only. The area of the two cuts is equal. *Bottom:* Background subtracted correlation spectrum: The events with a negative correlation time (inside the background cut of the spectrum at the top) are shifted in time by 150 ms and subtracted from the events with the expected correlation time. Bins with zero or a negative number of entries are plotted in white.

to the rotation of the scintillator. The graphical cut on the right-hand side of the spectrum in the top corresponds to correlated events with a positive correlation time between implantations and decays. This cut takes into account the rotation speed of $1000\,\mathrm{mm/s}$ at the Ne run. The spatial correlation has a width of $\pm 36\,\mathrm{mm}$. Due to the high implantation rate there are not only "real" correlations but also (random) background correlations in this cut. To get rid of theses background correlations there is a second graphical cut on the left-hand side of the spectrum in the top: As there is a negative correlation time between implantations and decays all events in this cut are background correlations. A subtraction of the events in the graphical cut with negative correlation time from the one with a positive correlation time is performed to quantify the amount of "real" correlations. Due to the data acquisition dead time of $t_{\mathrm{dead}} < 0.5\,\mathrm{ms}$ implantation-decay correlations with a time difference $|t_{\mathrm{diff}}| < t_{\mathrm{dead}}$ are missed. This is taken into account as only time differences $|t_{\mathrm{diff}}| > 1\,\mathrm{ms}$ are used for analysis of the half-life fits.

3.1.3 Analysis of half-life measurements

Figure 3.3 shows an example for time correlations of implantations and decays. The histogram which shows the difference of the correlated events and the random background events can be used for the half-life analysis. Because of the subtraction of the two histograms, the statistical errors of the resulting histogram get quite large, especially for decay times $\gtrsim 40\,\mathrm{ms}$. This fact is taken into account in the analysis. The maximum correlation time between implantations and decays is chosen to be $150\,\mathrm{ms}$ as the half-lives of the implanted nuclei of interest are smaller than $20\,\mathrm{ms}$.

In this analysis it has to be considered that there is not only the decay of the implanted very neutron-rich nuclides but there is a decay chain of many generations of nuclides: The mother nuclide ^{A}Z decays to a daughter nuclide $^{A}Z+1$, the daughter decays to a granddaughter $^{A}Z+2$. This chain continues for many generations of decays until it ends in the valley of stability. In addition to the "normal" β decay it is also possible to have β-delayed neutron emission after the decay of a very neutron-rich nuclide (see section 1.1). The probability to have an emission of one or two neutrons after the β decay is denoted with $P(n)$ and $P(2n)$, respectively. Consequently, the mother nuclide ^{A}Z can decay with a probability $P(n)$ to the β-n daughter $^{A-1}Z+1$ and with a probability $P(2n)$ to the β-2n daughter $^{A-2}Z+1$. A scheme of different generations of β decays can be seen in figure 3.4. In the analysis only the decays of the mother, daughter and granddaughter generations were taken into account. This is reasonable because the half-lives of the further decay generations are in the order of seconds whereas the half-lives of the investigated mother nuclides are in the order of milliseconds. In addition only the emission of up to two neutrons in one decay chain for the mother and daughter generation is considered. This assumption is justified as the probability to have more than two neutrons emitted in one decay chain is very low (for all decay chains investigated in this experiment). For the decay of the granddaughter generation the number of emitted neutrons has not to be considered as the further decay generations are neglected in the analysis.
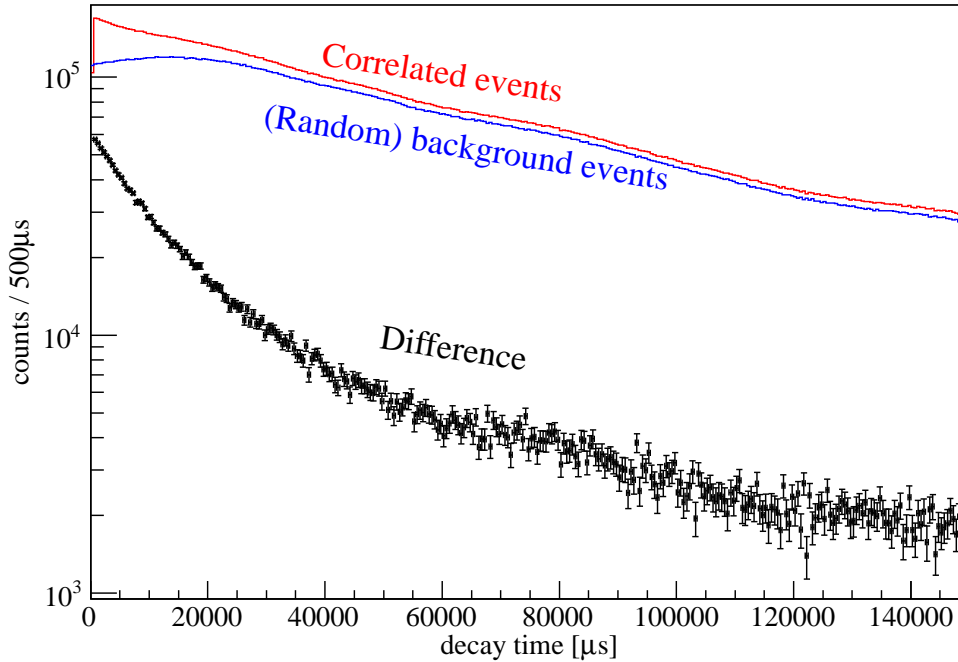
Figure 3.3: Time correlation of implantations and decays of ^{30}Ne. *Red:* Correlated events. *Blue:* (Random) background events. *Black:* Subtraction of the (random) background events from the correlated events. The background subtracted histogram can be used to determine the half-lives.
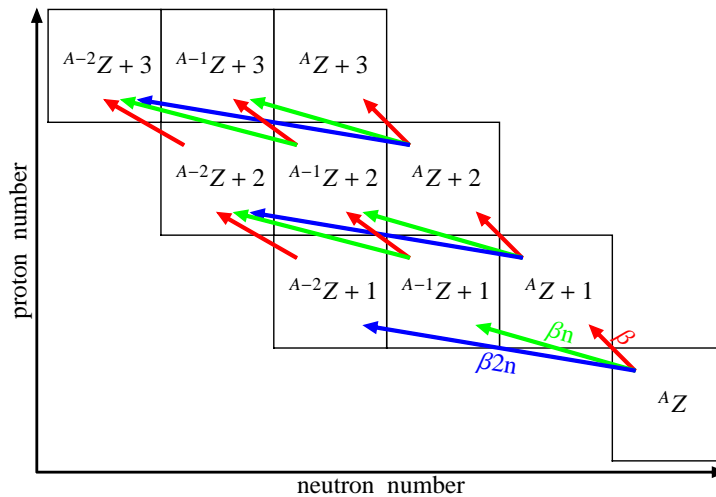
Figure 3.4: Scheme of the different generations of β decays considered in the analysis. Red arrows represent β decays without neutron emission, green and blue arrows represent decays with the β-delayed emission of one and two neutrons, respectively.

To extract the decay constants of the nuclei of interest the following mathematical considerations have to be made: Assuming that there is a mother nuclide implanted in the detector, this nuclide decays with a decay constant λ which corresponds to a half-life of $t_{1/2} = \frac{\ln 2}{\lambda}$. The probability that the mother nuclide (^{A}Z denoted with a subscript 1) exists at the time t is:

$$P_1(\lambda_1, t) = \exp(-\lambda_1 t) \tag{3.3}$$

The probability density that a decay of the mother with the decay constant λ_1 takes place in the infinitesimal interval between t and t + dt is given by:

$$f_1(\lambda_1, t) = \lambda_1 P_1(\lambda_1, t) = \lambda_1 \cdot \exp(-\lambda_1 t) \tag{3.4}$$

The probability that a daughter nuclide ^{A}Z+1 (P_{20}), a β-n daughter nuclide $^{A-1}$Z+1 (P_{21}) or a β-2n daughter nuclide $^{A-2}$Z+1 (P_{22}) exists at the time t can be calculated by solving the following differential equation with the initial conditions $P_{2x}(t = 0) = 0$:

$$\frac{\partial P_{2x}(p_{1,x}, \lambda_1, \lambda_{2x}, t)}{\partial t} = p_{1,x}\lambda_1 P_1(\lambda_1, t) - \lambda_{2x} P_{2x}(p_{1,x}, \lambda_1, \lambda_{2x}, t) \tag{3.5}$$

The subscript 2 stands for the daughter generation and the subscript x for the number of neutrons emitted after the mother decay. $p_{1,x}$ denotes the probability to have an emission of x neutrons after the β decay of the mother. So the probability that a daughter nuclide exists at the time t is:

$$P_{2x}(p_{1,x}, \lambda_1, \lambda_{2x}, t) = \frac{p_{1,x}\lambda_1}{\lambda_{2x} - \lambda_1}[\exp(-\lambda_1 t) - \exp(-\lambda_{2x} t)] \tag{3.6}$$

The probability density that a decay of a daughter nuclide with the decay constant λ_{2x} takes place in the infinitesimal interval between t and t + dt is given by:

$$f_{2x}(p_{1,x}, \lambda_1, \lambda_{2x}, t) = \lambda_{2x} P_{2x}(p_{1,x}, \lambda_1, \lambda_{2x}, t) = \frac{p_{1,x}\lambda_1\lambda_{2x}}{\lambda_{2x} - \lambda_1}[\exp(-\lambda_1 t) - \exp(-\lambda_{2x} t)] \tag{3.7}$$

The formulae for the further decay generations can be found in appendix A.1. The probability density that a decay of a mother, daughter or granddaughter nuclide takes place in the infinitesimal interval between t and t + dt is given by $f_{\text{total}}(t)$:

$$\begin{aligned}
f_{\text{total}}(t) = {}& f_1(\lambda_1, t) + \sum_{x=0}^{2} f_{2x}(p_{1,x}, \lambda_1, \lambda_{2x}, t) + f_{30}(p_{1,0}, p_{20,0}, \lambda_1, \lambda_{20}, \lambda_{30}, t) \\
& + f_{31}(p_{1,0}, p_{20,1}, p_{1,1}, p_{21,0}, \lambda_1, \lambda_{20}, \lambda_{21}, \lambda_{31}, t) \\
& + f_{32}(p_{1,0}, p_{20,2}, p_{1,1}, p_{21,1}, p_{1,2}, p_{22,0}, \lambda_1, \lambda_{20}, \lambda_{21}, \lambda_{22}, \lambda_{32}, t)
\end{aligned} \tag{3.8}$$

For the analysis of the half-life equation 3.8 is fitted to the decay curve with only two fit parameters: The decay constant of the mother nuclide λ_1 and an amplitude C. This

amplitude C is only a scaling factor as the probability density $f_{\text{total}}(t)$ is normalized (to the implantation of only one nuclide in the detector). All the other parameters are input parameters for the fit. The results of the half-life analysis of the implanted nuclei can be found in chapter 4.

3.2 Gamma detection

Three germanium clover detectors were used to detect β-delayed γ-rays. An energy calibration of the HP-Germanium clover detectors was performed with ^{207}Bi, ^{137}Cs and ^{60}Co sources. The full energy peaks of transitions were fitted and a linear energy calibration was performed.

3.2.1 Addback method

For the analysis two different methods of treating the data of the clover detectors were implemented:

- Single crystal method: Each of the four crystals of a clover detector is treated like a single detector. The energy of γ-rays which interact only by Compton scattering in a crystal can not be reconstructed in this mode.

- Addback method: All four crystals within a clover detector are treated like one large detector: The energies deposited in the four crystals are summed up. Therefore the energy of γ-rays which deposit a part of their energy via Compton scattering in one crystal and their remaining energy in another crystal of the clover can be reconstructed correctly. The γ-ray efficiency of this method is larger than with the single crystal method, especially for higher γ-ray energies. However, it is possible to have a background event instead of a Compton scattered γ-ray in a neighboring crystal. In this case the energy reconstruction with the addback method gives the wrong result.

3.2.2 Efficiency of the clover detectors

For the experimental results the relative γ-ray peak efficiencies are important. The determination of branching ratios is not possible without knowing the energy dependence of the efficiency. But a direct measurement of the efficiency for γ-rays which are emitted by implanted nuclides or their decay products is not possible. A measurement with a source would not account for the effect of the implantation depth in the scintillator. So the only way to obtain the efficiencies is a full simulation of the setup. A GEANT4 [GEA03, GEA06] simulation was carried out to calculate these efficiencies very accurately. The comparison in table 5.1 (chapter 5) of the relative intensities of β-delayed γ-rays after the decay of ^{30}Ne with a previous experiment shows the accuracy of the simulation over a wide energy range from $E_\gamma = 150$ to $2100\,\text{keV}$.

In the simulation it was assumed that the photons are emitted isotropically. The photons had to penetrate a $10\,\text{mm}$ thick layer of plastic before they could reach the
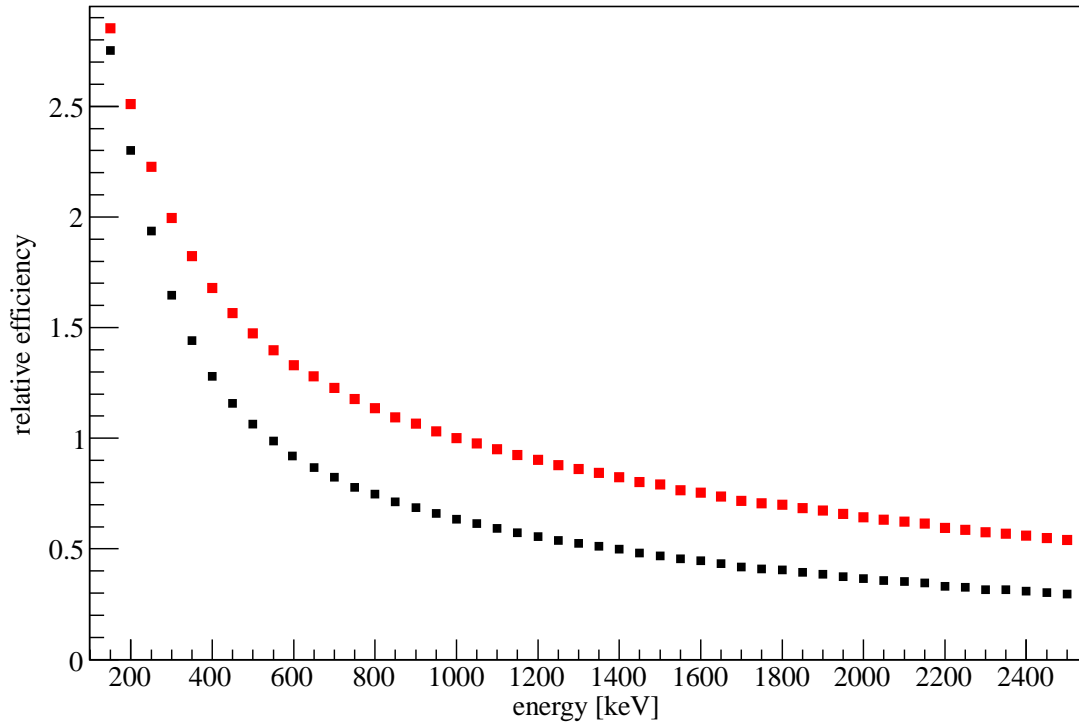
Figure 3.5: Relative full energy peak efficiency for the detection of γ-rays of different energies from $E_\gamma = 150$ to $2500\,\text{keV}$. The efficiency was derived from a GEANT4 simulation of the three clover detectors in the geometrical arrangement as shown in figure 2.5. The γ-rays were emitted from the implantation position. The efficiency with the addback method is drawn in red, the efficiency without addback in black. The data are normalized to the efficiency with addback at $E_\gamma = 1\,\text{MeV}$. The statistical errors are smaller than the used symbols.

clover detectors. The depth of the plastic layer corresponds to the average implantation depth in the CAITEN scintillator. The result of the simulation for energies from $E_\gamma = 150$ to $2500\,\text{keV}$ can be seen in figure 3.5. For energies $E_\gamma \lesssim 150\,\text{keV}$ the efficiency is very sensitive to the thickness of the dead layer of the Germanium crystal. This issue is discussed in section A.2 in the appendix. A detailed description of a γ-ray efficiency simulation of HP-Germanium detectors can be found in [Ste09].

Chapter 4

Results and interpretation of the half-life measurements

4.1 Half-life measurements using known parameters of the decay chain

As described in subsection 3.1.3 the half-life measurement with the CAITEN detector is not only sensitive to the half-life of the implanted nuclide but also to the half-lives $t_{1/2}$ and the branching ratios of β-delayed neutrons $P(n)$ and $P(2n)$ of its descendants as it is an integrated measurement which does not distinguish between the decays of different generations. Consequently one has to assume half-lives $(t_{1/2})$ and the β-delayed neutron emission probabilities ($P(n)$ and $P(2n)$) of the second and third generation to obtain a reliable result for the implanted nucleus of interest. As the known experimental values of these parameters have an uncertainty, the measured half-lives of the implanted nuclides will be presented dependent on the uncertainties of the parameters. Therefore the uncertainty of the mother half-life consists of the statistical uncertainty of the measurement and the systematic uncertainties from the input parameters of the half-life fit. To quantify the dependence of the half-life of the implanted nuclide on a parameter x, the parameter Δx is introduced which corresponds to the difference of the "real" value x_{real} and the known literature value x_{lit} divided by the uncertainty of the literature value $\sigma(x_{\text{lit}})$:

$$\Delta x = \frac{x_{\text{real}} - x_{\text{lit}}}{\sigma(x_{\text{lit}})} \tag{4.1}$$

The fit range is chosen to be ≈ 5 times the half-life of the implanted nuclide. Consequently $1 - (1/2)^5 \approx 97\%$ of the mother decays appear in this range, which is almost the complete sample. A larger range would lead to an increase of the systematic uncertainties of the descendants. This range is a compromise of collecting most of the mother decays but being as insensitive as possible to the uncertainties of the descendants. The figures 4.1 to 4.4 show the half-life fits for the implanted nuclides and table 4.1 gives the results of the fits. The example of ^{30}Ne is used here to explain how to read the table. The measured half-life $t_{1/2}(^{30}\text{Ne})$ in the experiment is 7.40 ms with a statistical uncertainty of 0.04 ms. The literature value for the half-life of the daughter ^{30}Na is

48 ± 2 ms [Lan84]. If the "real" value of the half-life of ^{30}Na is 50 ms (or 46 ms) which corresponds to $t_{1/2}(^{30}\text{Na}) + (-)\sigma(t_{1/2}(^{30}\text{Na}))$ then the measured half-life $t_{1/2}(^{30}\text{Ne})$ increases (decreases) by 0.07 ms. The same method can be applied for the branching ratio $P_{2n}(^{30}\text{Ne})$ and the half-life of the β-n daughter $t_{1/2}(^{29}\text{Na})$. The result for the half-life of ^{30}Ne is:

$$
\begin{aligned}
t_{1/2}(^{30}\text{Ne}) = \big[7.40 \pm 0.04(\text{stat.}) \pm 0.07 \left(\text{sys. } \Delta t_{1/2}(^{30}\text{Na})\right) \\
\pm 0.02 \left(\text{sys. } \Delta P_{2n}(^{30}\text{Ne})\right) \pm 0.01 \left(\text{sys. } \Delta t_{1/2}(^{29}\text{Na})\right) \big] \text{ ms}
\end{aligned}
\tag{4.2}
$$

In the same way the results for the other implanted nuclides can be read. The input parameters for the half-life fits can be found in the appendix in table A.1 and A.2.

Comparing the results of the half-lives measured in this work with literature values there is good agreement within the mutual 1σ uncertainties for all nuclei but ^{35}Mg and ^{36}Mg. The literature half-life $t_{1/2}(^{35}\text{Mg})_{\text{lit}} = 70(40)$ ms [Eva12, Ree95] has a very large uncertainty which includes the result of this work $t_{1/2}(^{35}\text{Mg})_{\text{this work}} = (11.25 \pm 0.49(\text{stat.}) \pm 0.19(\text{sys.}))$ ms within 1.5σ. $t_{1/2}(^{36}\text{Mg})_{\text{lit}} = 3.9(1.3)$ ms [Eva12, Gré04] is consistent with the result of this work $t_{1/2}(^{36}\text{Mg})_{\text{this work}} = (7.63 \pm 0.06(\text{stat.}) ^{+0.48}_{-0.75}(\text{sys.}))$ ms within 1.8σ. The total uncertainties (sum of statistical und systematic uncertainties) of the half-lives measured in this work of ^{29}F, ^{30}Ne and ^{35,36}Mg are smaller than the corresponding uncertainties of the literature half-lives. For ^{31,35}Na und ^{37,38}Al the systematic uncertainties dominate the total uncertainties. They can get smaller if the half-lives of the descendants and the $P(n)$ and $P(2n)$ values are measured with a higher precision.

	measured $t_{1/2}$ [ms]	statistical error [ms]	χ^2/ndf	Δt_{20} [ms]	$\Delta P(n)$ [ms]	Δx [ms]	literature $t_{1/2}$ [ms] [Eva12]
^{29}F	2.67	0.10	0.85	0.00	0.16	Δt_{21} 0.02	2.5(3)
^{30}Ne	7.40	0.04	1.16	0.07	0.00	ΔP_{2n} 0.02, Δt_{21} 0.01	7.3(3)
^{31}Na	17.53	0.18	1.08	0.15	0.16	Δt_{21} 0.05	17.0(4)
^{35}Na	2.44	0.31	0.86	0.10	-0.16	Δt_{21} 0.29	1.5(5)
^{35}Mg	11.25	0.49	0.89	0.02	0.17	Δt_{21} 0.21	70(40)
^{36}Mg	7.63	0.06	1.03	$^{+0.27}_{-0.54}$	-0.21		3.9(13)
^{37}Al	11.85	0.06	1.02	$^{+0.93}_{-2.11}$	1.27		10.7(13)
^{38}Al	8.67 *	0.15	0.89	$^{+0.90}_{-2.21}$	0.00		7.6(6)

Table 4.1: Measured half-lives and uncertainties. All half-lives and uncertainties are given in milliseconds, the χ^2/ndf is a measure for the quality of the fit. t_{20} and t_{21} correspond to the half-life of the daughter and β-n daughter. $P(n)$ and $P(2n)$ are the probabilities to have an emission of one or two neutron after the mother decay. An explanation of how to read the table can be found in the text. (*) Half-life of daughter ^{38}Si not known experimentally, from systematics [Aud03]: $t_{1/2}(^{38}\text{Si}) = 90(60)$ ms.
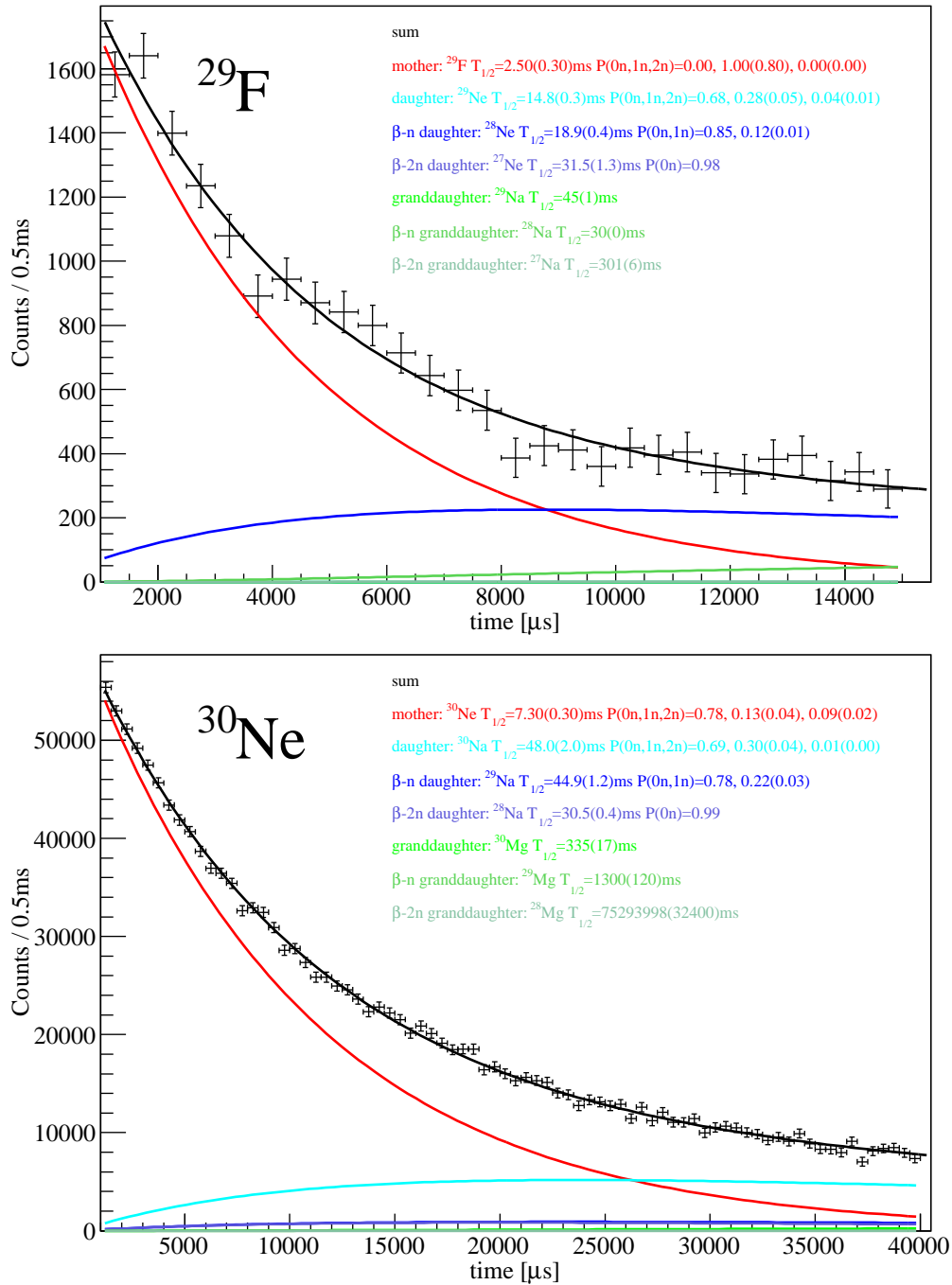
Figure 4.1: Experimental decay curves and fitted results for ^{29}F (top) and ^{30}Ne (bottom). Aside from the total fit curves the contributions from the mother, daughter and granddaughter decay modes are shown. The literature half-lives of the mother nuclei ^{29}F and ^{30}Ne are the start values for the fits. All the other half-life, $P(n)$ and $P(2n)$ values shown in the figure are input parameters for the fit.

Figure 4.2: Decay measurement and fit of the different contributions for ^{31}Na (top) and ^{35}Na (bottom).

Figure 4.3: Decay measurement and fit of the different contributions for ^{35}Mg (top) and ^{36}Mg (bottom).

Figure 4.4: Decay measurement and fit of the different contributions for ^{37}Al (top) and ^{38}Al (bottom).

4.2 Half-life measurements with coincident gamma-rays

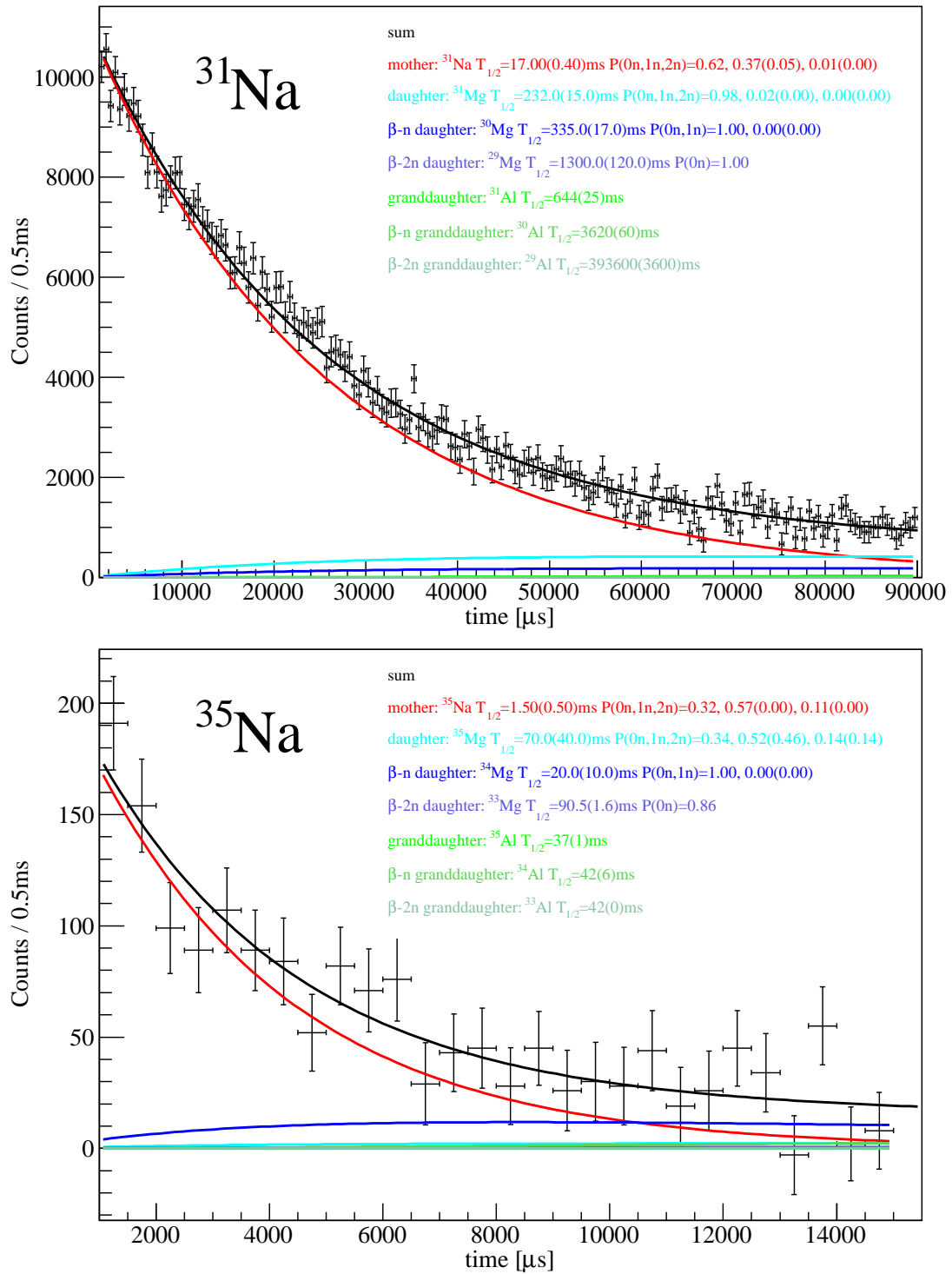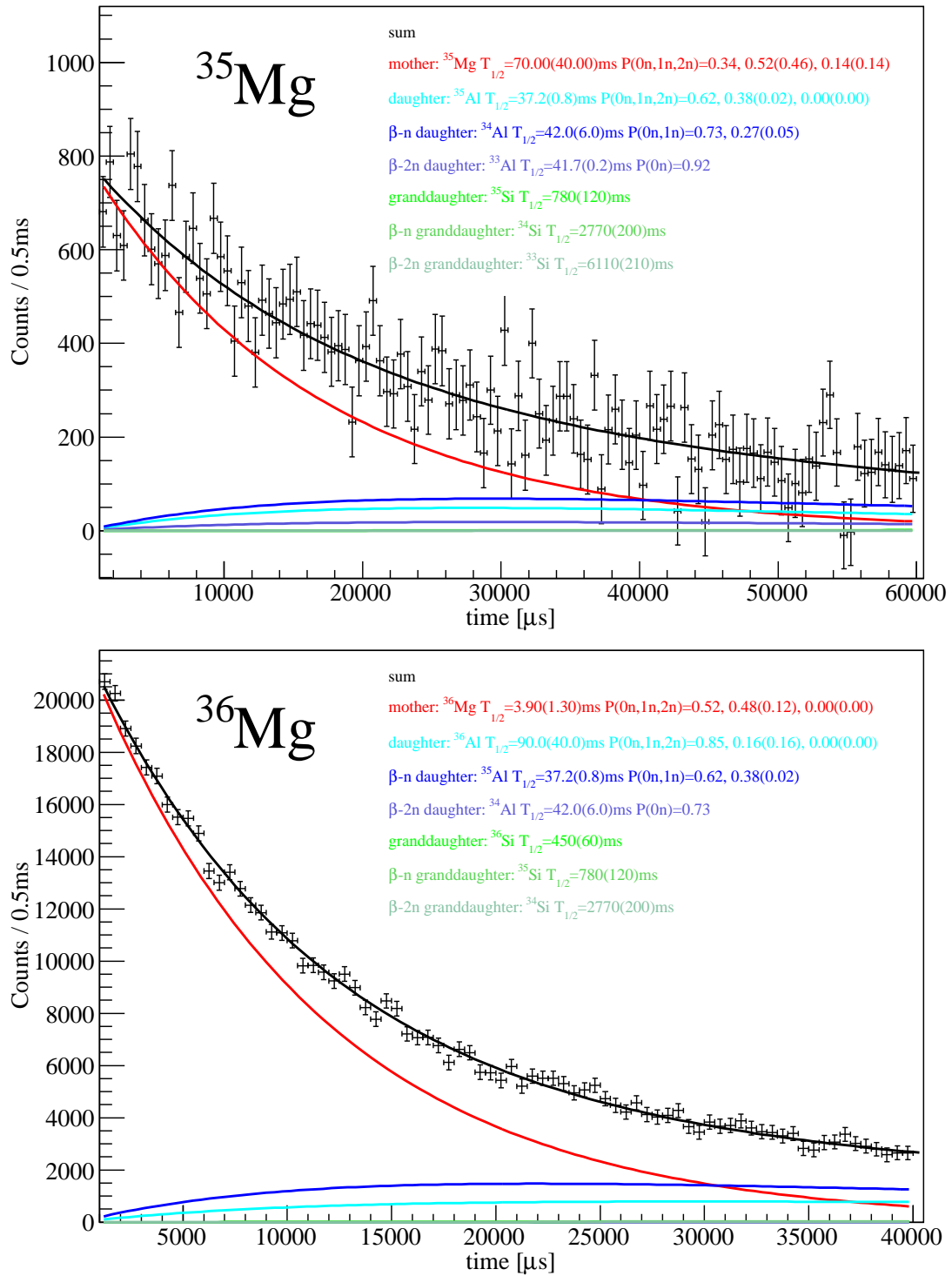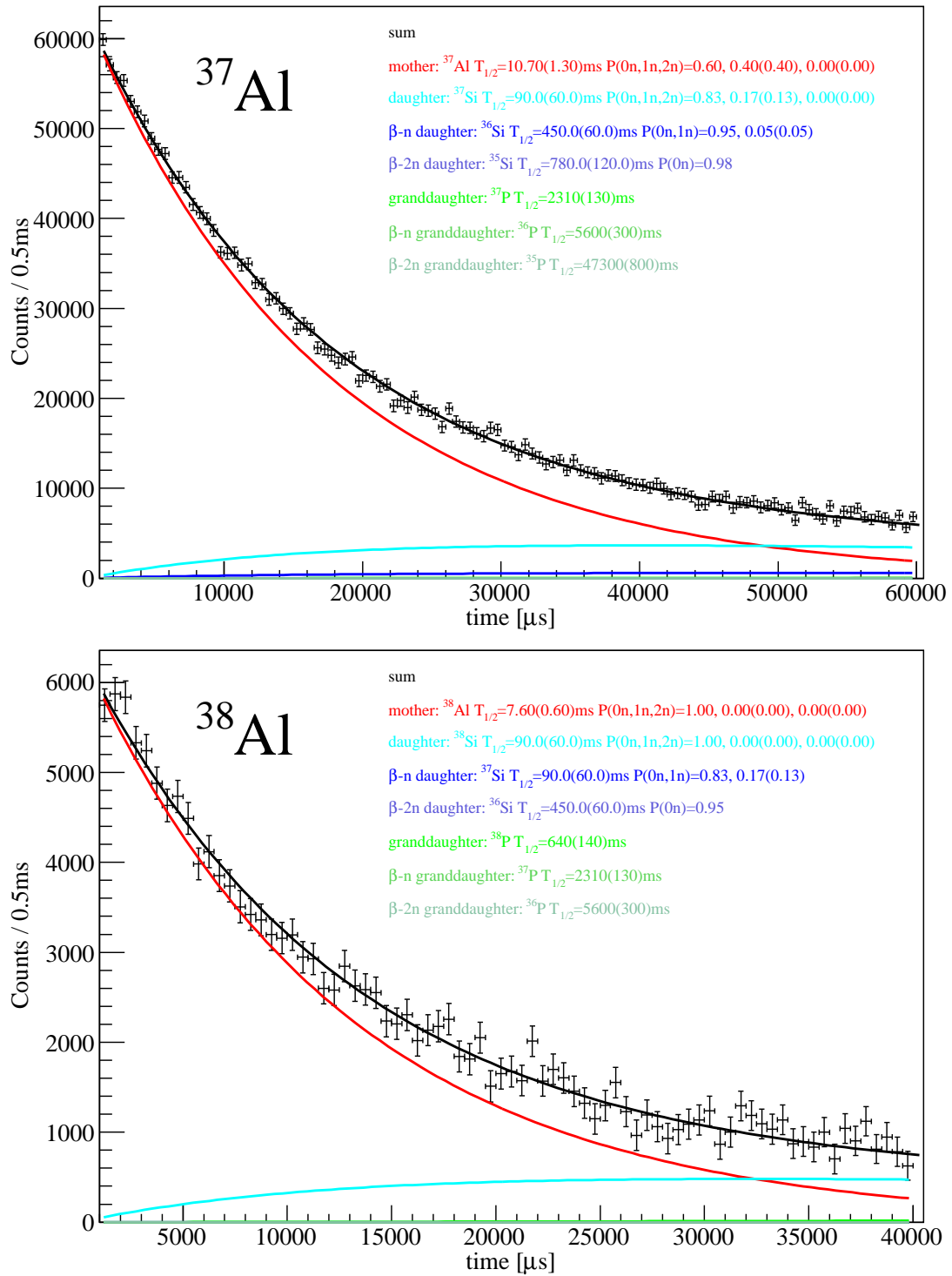Another method to determine half-lives without additional input parameters from the decay chain is the measurement of decays with coincident γ-rays which originate from the β decay daughter. However since it is necessary to have a β-γ coincidence the efficiency of this method is reduced by the small γ-ray efficiency. Therefore it can only be applied for the decay of nuclides which are implanted with high statistics. In the present case it can be used for the decays of ^{30}Ne and ^{37,38}Al. The advantage of a β-γ coincidence is that the detected decay can be assigned unambiguously to a decay of the implanted nuclide (The only exception would be a β-n decay of ^{31}Ne or ^{38}Al). A decay of a β-daughter nuclide or from a further decay generation does not have a coincidence with a γ-ray with a specific energy. The background subtraction which was introduced in section 3.1.2 was used here, too.

The half-life of ^{30}Ne is determined by decays with coincident γ-rays with an energy of 151, 367, 410, 1598, 1963 or 2113 keV. These γ-rays originate from the deexcitation in the β decay daughter ^{30}Na. For the half-life of ^{37}Al γ-rays in the β decay daughter ^{37}Si with an energy of 156, 562, 717, 1115 or 1270 keV and for ^{38}Al γ-rays in the daughter ^{38}Si with an energy of 418, 1074, 1159 or 1470 keV are used (see sections 5.2 and 5.3 for details). The figures 4.5 and 4.6 show the decay curves of ^{30}Ne and ^{37,38}Al using
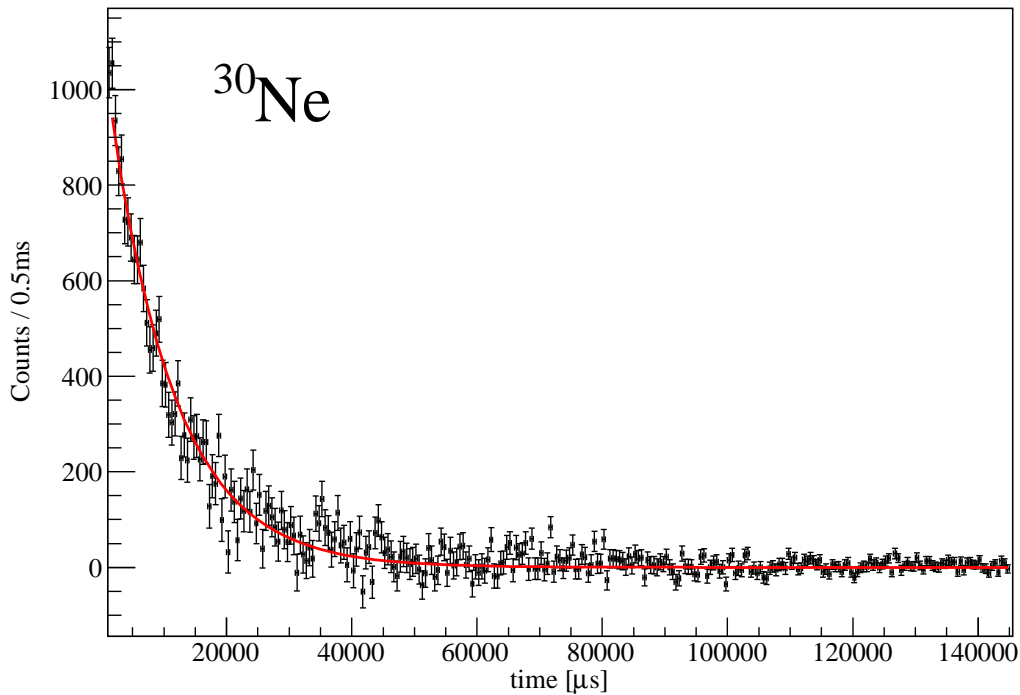
Figure 4.5: β decay curve for ^{30}Ne measured with coincident γ-rays with an energy of 151, 367, 410, 1598, 1963 or 2113 keV. The red line corresponds to an exponential decay fit (equation 4.3).
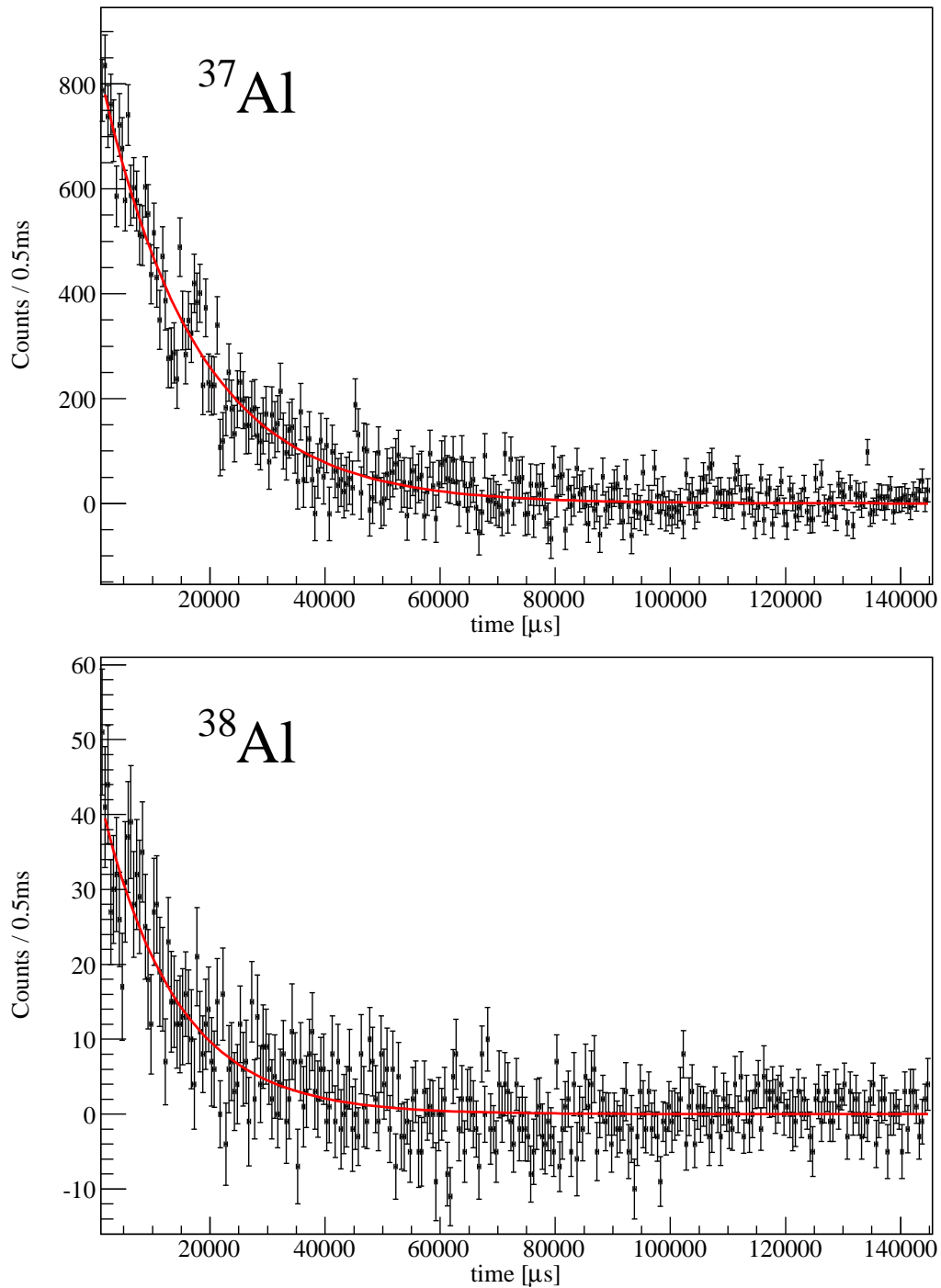
Figure 4.6: β decay curves measured with coincident γ-rays. *Top:* Decays of ^{37}Al coincident to γ-rays with an energy of 156, 562, 717, 1115 or 1270 keV. *Bottom:* Decays of ^{38}Al coincident to γ-rays with an energy of 418, 1074, 1159 or 1470 keV.

coincident γ-rays. The decay curve is fitted with an exponential function $f(t)$ with two fit parameters: A scaling factor C and a decay constant $\lambda = \ln 2/t_{1/2}$:

$$f(t) = C \cdot \exp\left(-\lambda t\right) \tag{4.3}$$

The resulting half-lives of ^{30}Ne and ^{37}Al are consistent with the previous literature values but with a smaller uncertainty (see table 4.2). The measured half-life of ^{38}Al is almost consistent with the literature value and the uncertainty is similar to the one of the literature value.

	measured $t_{1/2}$ [ms]	statistical uncertainty [ms]	χ^2/ndf	literature $t_{1/2}$ [ms] [Eva12]
^{30}Ne	7.18	0.22	1.25	7.3(3)
^{37}Al	11.5	0.4	1.00	10.7(13)
^{38}Al	9.0	0.7	0.92	7.6(6)

**Table 4.2:** Resulting half-lives and uncertainties measured with coincident γ-rays. The half-lives and uncertainties are given in milliseconds, the χ^2/ndf is a measure for the quality of the fit.

4.3 Summary of the results of the half-life measurements

Table 4.3 shows the results of the half-life measurements. Within the 1σ uncertainties the results of section 4.1 and 4.2 agree with each other. In addition they agree with the present literature values and have a smaller uncertainty (except ^{38}Al which has a similar uncertainty because of the small statistics in this experiment).

Theoretical shell model predictions [Wil83] for the half-lives of $N = 20$ isotones calculated in the sd valence space result in $t_{1/2}^{\text{theo}}(^{29}\text{F}) = 2.7\,\text{ms}$, $t_{1/2}^{\text{theo}}(^{30}\text{Ne}) = 3.7\,\text{ms}$ and $t_{1/2}^{\text{theo}}(^{31}\text{Na}) = 12\,\text{ms}$. The prediction for ^{29}F agrees very well with the measured half-life. For ^{30}Ne and ^{31}Na there is an agreement within a factor of 2. As ^{30}Ne and ^{31}Na are known to be inside the Island of Inversion a valence space which also includes the neutron pf shell was needed to give better predictions for these nuclei. The theoretical predictions from Möller and collaborators [Möl97] were obtained by quasi-particle random phase approximation (QRPA).

	$t_{1/2}$ [ms] this work from section 4.1	$t_{1/2}$ [ms] this work from section 4.2	$t_{1/2}$ [ms] sd shell calculation [Wil83]	$t_{1/2}$ [ms] QRPA calculation [Möl97]	$t_{1/2}$ [ms] literature [Eva12]
^{29}F	2.67(10)(18)		2.7	2.3	2.5(3)
^{30}Ne	7.40(4)(10)	7.18(22)	3.7	14	7.3(3)
^{31}Na	17.5(2)(4)		12	6.6	17.0(4)
^{35}Na	2.4(3)(6)			3.3	1.5(5)
^{35}Mg	11.3(5)(4)			34	70(40)
^{36}Mg	7.6(1)($^{+5}_{-8}$)			18	3.9(13)
^{37}Al	11.8(1)($^{+22}_{-34}$)	11.5(4)		6.8	10.7(13)
^{38}Al	8.7(2)($^{+9}_{-22}$)	9.0(7)		5.0	7.6(6)

Table 4.3: Summary of the results of the half-life measurements and comparison to the results of the sd shell calculations [Wil83] and QRPA calculations [Möl97]. All numbers are given in milliseconds. Statistical and systematic uncertainties of the measurements are given in brackets.

Chapter 5

Results and interpretation of the gamma-ray spectroscopy

With β-delayed γ-ray spectroscopy a reconstruction of the level schemes of β-daughters of implanted nuclei and the determination of branching ratios to the different states in the daughter are possible. The results of the γ-ray spectroscopy are discussed in this chapter.

5.1 Decay of ^{30}Ne

Figure 5.1 shows the β-delayed γ-ray spectrum after the decay of ^{30}Ne. As pointed out for the half-life measurements in section 3.1.2 a background subtraction is necessary to distinguish between random and real coincidences of implantations and decays. The red spectrum in figure 5.1 shows the γ-rays without any background subtraction within 10 ms after an implantation. Also γ-rays lines which do not originate from the ^{30}Ne decay chain can be seen in this spectrum (e.g. a line with an energy of 171 keV which originates from ^{31}Mg after the decay of ^{31}Na). These wrongly correlated γ-rays disappear in the background subtracted spectrum in figure 5.1 which is plotted in black.

The background subtracted γ-ray spectrum is generated by the subtraction of the γ-ray spectrum with a negative correlation time of implantations and decays from the γ-ray spectrum with a positive correlation time. Both time windows have a width of 10 ms. Background lines vanish by the subtraction. The statistical uncertainties of the resulting spectrum are calculated the following way: Let x_{pos} and x_{neg} be the entries of a bin in the γ-ray spectrum with positive and negative correlation time. Then $x_{\text{sub}} = x_{\text{pos}} - x_{\text{neg}}$ is the bin entry in the background subtracted spectrum. With the statistical errors $\Delta x_{\text{pos}} = \sqrt{x_{\text{pos}}}$ and $\Delta x_{\text{neg}} = \sqrt{x_{\text{neg}}}$ the statistical error of the entry in the background subtracted spectrum becomes

$$\Delta x_{\text{sub}} = \sqrt{\Delta x_{\text{pos}}^2 + \Delta x_{\text{neg}}^2} = \sqrt{x_{\text{pos}} + x_{\text{neg}}}. \tag{5.1}$$

Consequently the statistical errors Δx_{sub} at the photopeak energies of background lines are larger than the errors at energies with no background lines. At the photopeak
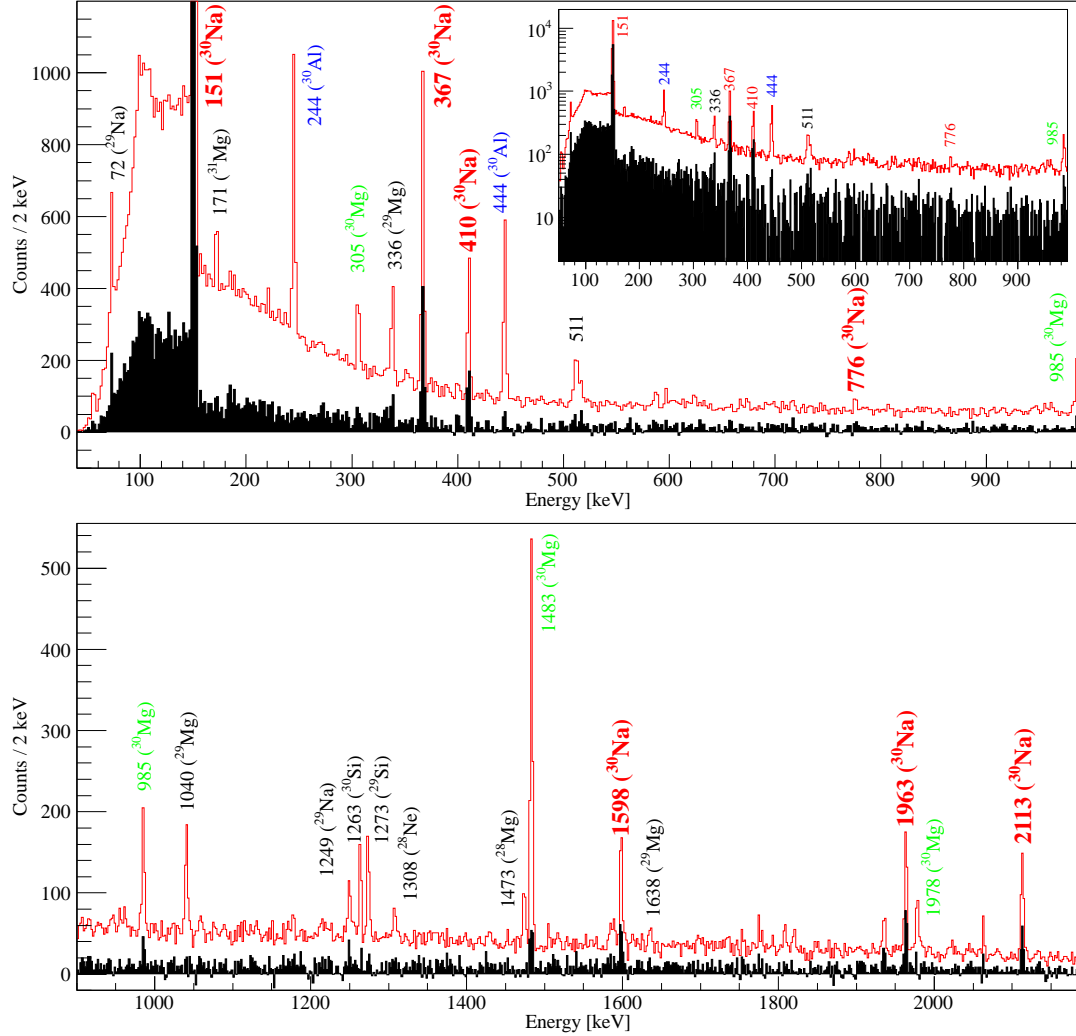
Figure 5.1: β-delayed γ-ray spectrum after the decay of ^{30}Ne. The black (red) spectrum corresponds to implantation-decay correlations within 10 ms after an implantation with (without) background subtraction. Lines from transitions in the daughter ^{30}Na, the granddaughter ^{30}Mg and the great-granddaughter ^{30}Al are marked in red, green and blue, respectively.

energies both x_{pos} and x_{neg} are large in comparison to energies without background peaks.

Six γ-rays marked in red with energies of 151, 367, 410, 1598, 1963 and 2113 keV appear in the background-subtracted spectrum. They all correspond to transitions in the daughter nucleus ^{30}Na which is the β decay daughter of ^{30}Ne. In addition there may be a very low intensity line at 776 keV. In a previous β decay experiment [Tri07a, Tri07b] these β-delayed γ-rays were already measured.

In the spectrum without background subtraction also lines which correspond to transitions in the granddaughter ^{30}Mg (305, 985, 1483 and 1978 keV), the great granddaughter ^{30}Al (244 and 444 keV), the β-n daughter ^{29}Na (72 and 1249 keV), the β-n granddaughter ^{29}Mg (336, 1040 and 1638 keV) and the β-2n granddaughter ^{28}Mg (1473 keV) can be seen. The lines at 1263 and 1273 keV originate from the stable nuclei ^{30}Si and ^{29}Si, respectively, which are at the end of the decay chains of ^{30}Ne.

There are 2 background lines with a different origin: The lines at 171 keV (transition in ^{31}Mg) and 1308 keV (transition in ^{28}Ne, will be discussed in section 5.6). These lines are background lines which appear after the β decay of ^{31}Na and the β-n decay of ^{29}F. ^{31}Na and ^{29}F are implanted in the CAITEN detector with a high rate (see particle identification in figure 2.3 of section 2.2).

In addition to this single γ-ray spectrum it is possible to use γ-γ coincidences to obtain information on where to place the different transitions in the level scheme. Figure 5.2 shows γ-γ coincidence spectra after the decay of ^{30}Ne. The following coincidences are measured: The transition at 151 keV is coincident to the lines at 367, 410, 776, 1598 and 1963 keV. The 367 keV transition is coincident to the 410 and 1598 keV lines.

To distinguish between γ-rays which are emitted by the β decay daughter (or β-n daughter) and γ-rays from further decay generations the time evolution of the γ-ray spectrum can be taken into account. Figure 5.3 shows the background subtracted γ-ray spectrum after an implantation-decay correlation of ^{30}Ne for four different time windows: These windows range from 0 to 10 ms, 10 to 20 ms, 20 to 30 ms and 30 to 40 ms for the time difference between implantation and decay. As the half-life of ^{30}Ne is measured to be 7.40 ± 0.04(stat.) ± 0.10(sys.) ms most of the decays of ^{30}Ne appear in the time window from 0 to 10 ms whereas most of the decays of the daughter and granddaughter nuclei appear in the other time windows. It can be seen in figure 5.3 that the γ-rays with an energy of 151, 367, 410, 1598, 1963 and 2113 keV are predominantly measured in the time window from 0 to 10 ms and can consequently be attributed to the β decay of ^{30}Ne. The γ-rays after the secondary β decay from the daughter ^{30}Na to the granddaughter ^{30}Mg with the energies of 985, 1483 and 1978 keV have their

energy [keV]	intensity [%] this experiment	intensity [%] [Tri07b, Eva12]
151	100(3)	100(13)
367	13(1)	12(3)
410	7.2(1.0)	8(1)
776	0.8(0.7)	2(1)
1598	5.3(1.4)	6(2)
1963	8.5(1.8)	6(2)
2113	8.7(2.1)	5(2)

Table 5.1: Relative intensities of β-delayed γ-rays after the decay of ^{30}Ne, normalized to the γ-ray at an energy of 151 keV and corrected for efficiency.
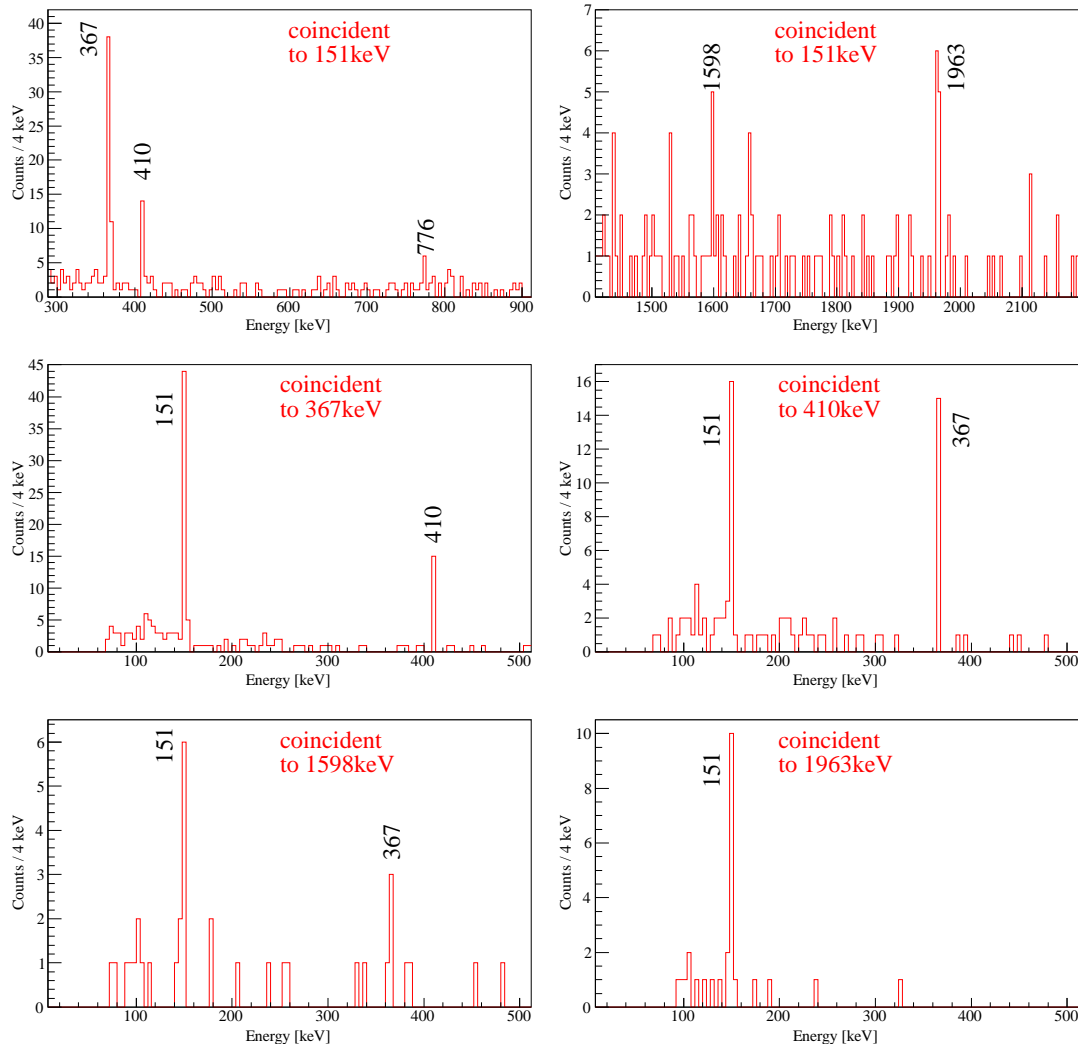
Figure 5.2: γ-γ coincidence spectra after the decay of ^{30}Ne within 10 ms after an implantation, gated on the transitions indicated in the spectra. The transition at an energy of 151 keV is coincident to the transitions at 367, 410, 776, 1598 and 1963 keV. The lines at an energy of 367 and 410 keV are in mutual coincidence. In addition there is a coincidence between the 367 and 1598 keV lines.

maximum intensities in the time windows from 10 to 40 ms after an implantation.

Table 5.1 shows a comparison of the relative γ-ray intensities of this experiment with a previous measurement [Tri07b]. The relative γ-ray efficiencies discussed in section 3.2.2 were taken into account. The statistical uncertainties of the bin contents in the background-subtracted γ-ray spectrum discussed before were used to obtain the uncertainties of the intensities. The results for the intensities of this experiment and [Tri07b] agree very well. With the information from the single γ-ray spectrum,
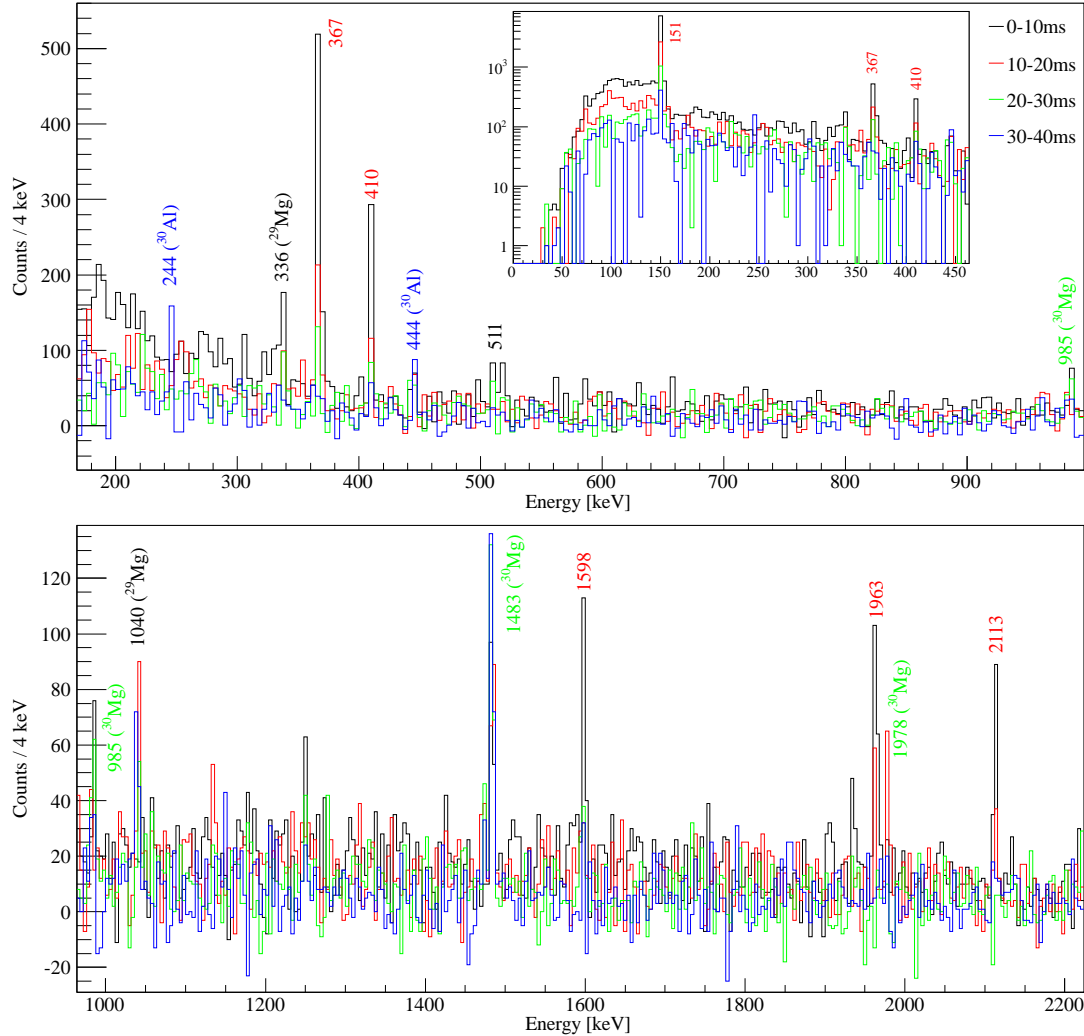
Figure 5.3: Background subtracted β-delayed γ-ray spectrum after an implantation-decay correlation of ^{30}Ne. The black, red, green and blue spectra correspond to implantation-decay correlation time windows from 0 to 10 ms, 10 to 20 ms, 20 to 30 ms and 30 to 40 ms, respectively. Lines from transitions in the daughter ^{30}Na, the granddaughter ^{30}Mg and the great-granddaughter ^{30}Al are marked in red, green and blue, respectively.

the γ-γ coincidence spectra and the time evolution of the transitions a construction of a (partial) level scheme of the β decay daughter ^{30}Na is possible. Following the argumentation in [Tri07a] the 151 keV transition has the highest intensity and should be a ground state transition from a 151 keV level. The 1963 keV line is coincident to 151 keV and there is a transition with the sum energy of 2113 keV. So there is an excited level at 2113 keV. As the sum peak of the coincident transitions with the energies 367
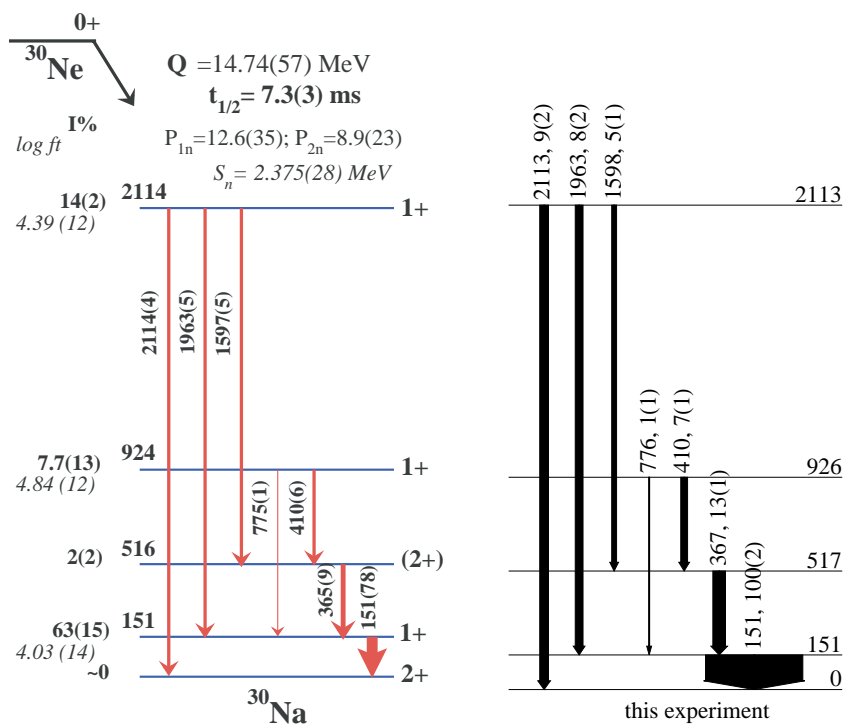
Figure 5.4: *Left:* Experimental level scheme of ^{30}Na from [Tri07b]. The transitions are labeled with their energies in keV and their absolute intensities in %. *Right:* Level scheme of ^{30}Na from this experiment. The transitions are labeled with their energies in keV and their (efficiency corrected) relative intensities in % normalized to the transition with an energy of 151 keV.

and 1598 keV is 1963 keV and these three transitions are coincident to the 151 keV transition there is an excited level at 516 keV which is fed by the 1598 keV transition and deexcited by the 367 keV transition. The low intensity transition at 776 keV is the sum peak of the 367 and 410 transition. All these three transitions are coincident to 151 keV, so there is an excited level at 925 keV which is deexcited by the 410 and 776 keV transitions.

The resulting level scheme of the β decay daughter nucleus ^{30}Na with excited states at 151, 516, 925 and 2113 keV is shown in figure 5.4. This experiment reproduces the results of [Tri07a, Tri07b] in a very good agreement. This fact proves that the methods of the analysis of this experiment are reliable and produce accurate results.

5.2 Decay of ^{37}Al

The β-delayed γ-ray spectrum after the decay of ^{37}Al is shown in figure 5.5. Previously unknown γ-lines with energies of 156, 562, 717, 1115, 1202, 1270 and 1504 keV were measured for the first time. The γ-lines with an energy of 1409 and 1441 keV correspond
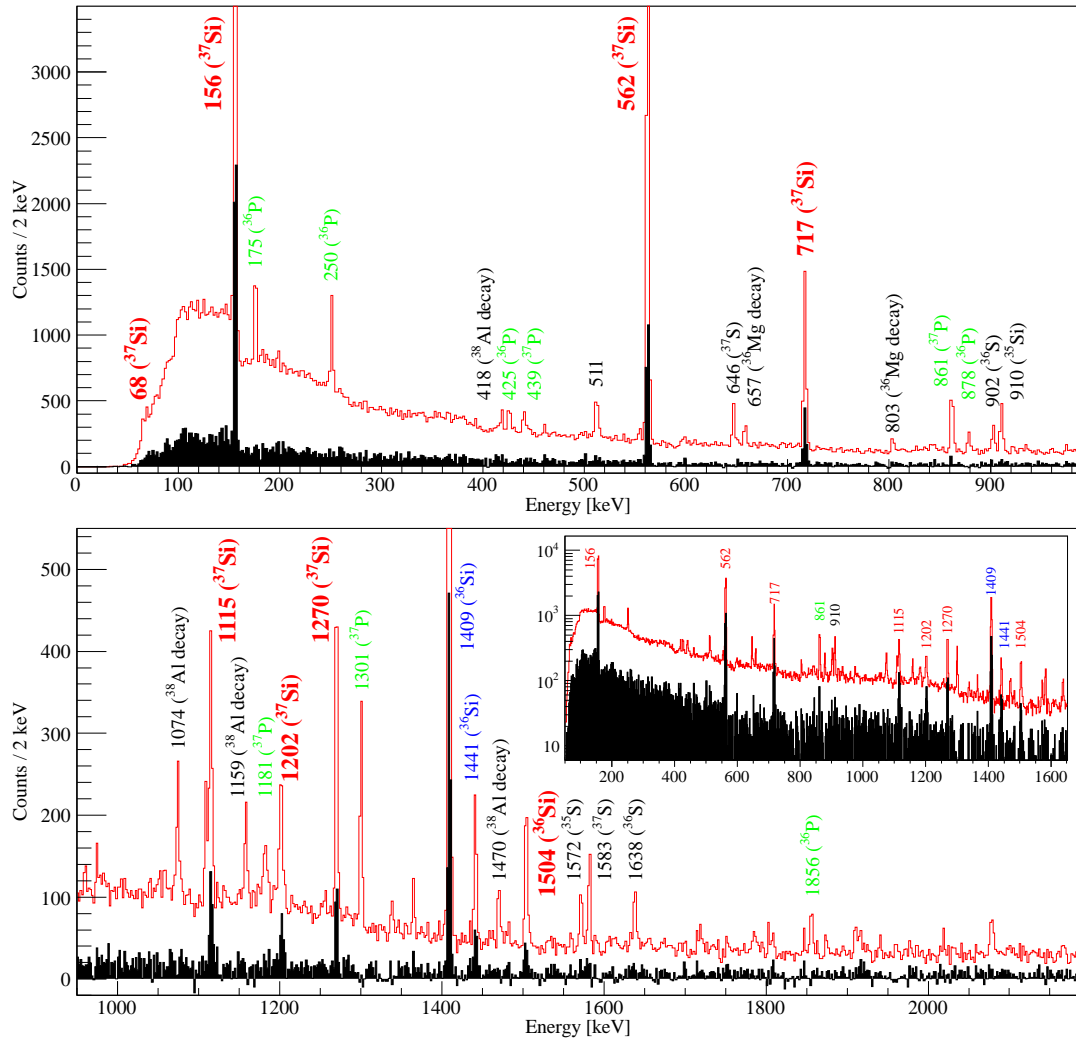
Figure 5.5: β-delayed γ-ray spectrum after the decay of ^{37}Al. Previously unknown lines from transitions in the daughter ^{37}Si and the β-n daughter ^{36}Si are marked in red. Known lines in the β-n daughter ^{36}Si and the (β-n) granddaughters ^{36,37}P are marked in blue and green, respectively.

to the $2_1^+ \rightarrow 0_{gs}^+$ and $4_1^+ \rightarrow 2_1^+$ transitions in the β-n daughter ^{36}Si, respectively [Lia06]. All other lines disappear in the background subtracted spectrum because they do not originate from the ^{37}Al decay.

As shown in figure 5.6 all previously unknown lines are prompt lines which have their maximum intensity within the first time window from 0 to 10 ms of an implantation-decay correlation.

The γ-γ coincidence spectra in figure 5.7 show the coincidence of the 156 keV line with the lines at 562 and 1115 keV and the coincidence of the 1504 keV line with the
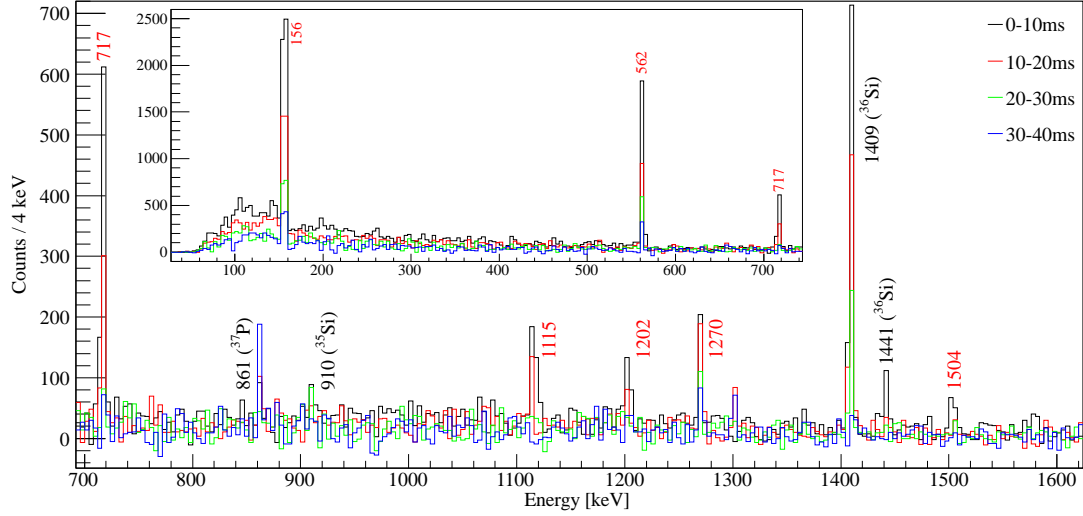
Figure 5.6: Background subtracted β-delayed γ-ray spectrum after the decay of ^{37}Al. The black, red, green and blue spectra correspond to implantation-decay correlations time windows with a width of 10 ms (see legend). Previously unknown lines from transitions in the daughter ^{37}Si and the β-n daughter ^{36}Si are marked in red.

line at 1409 keV. As the 1409 keV line originates from ^{36}Si, the 1504 keV line must be a transition in ^{36}Si, too. As the sum of 156 and 562 keV is 717 keV and the sum of 156 and 1115 keV is 1270 keV, the 717 and 1270 keV lines are the sum peaks of these transitions. Table 5.2 shows the relative intensities of the measured transitions. As the 156 keV line has the largest intensity it should be a ground state transition. Consequently the 562 and 717 keV lines originate from a level at an energy of 717 keV and the 1115 and 1270 keV lines originate from a level at an energy of 1270 keV. It is not clear where to place the 1202 keV line in the level scheme of ^{37}Si. No coincident γ-rays could be measured with this line. So it is uncertain that this line originates from ^{37}Si or the β-n decay to ^{36}Si. However theoretical calculations (see section 5.2.2) suggest that it originates from ^{37}Si.

In the recent Atomic Mass Evaluation [Wan12] the Q_β value of ^{37}Al is $Q_\beta(^{37}$Al$) = 16.40(15)$ MeV and the one-neutron and two-neutron separation energies of the daughter nucleus ^{37}Si are quoted to be $S_n = 2.27(11)$ MeV and $S_{2n} = 8.38(9)$ MeV. The Pandemonium effect[1] [Har77] should not play an important role in ^{37}Si because it has a small neutron separation energy and therefore all states which are populated beyond the neutron separation energy decay via neutron emission.

---

[1]Pandemonium effect: Low intensity β-delayed γ-rays may be unobserved because of the detection efficiency. If these unobserved transitions populate excited states the β-branching ratios to these states must be altered as they are deduced from the measured γ-ray intensities which populate and deexcite these states.
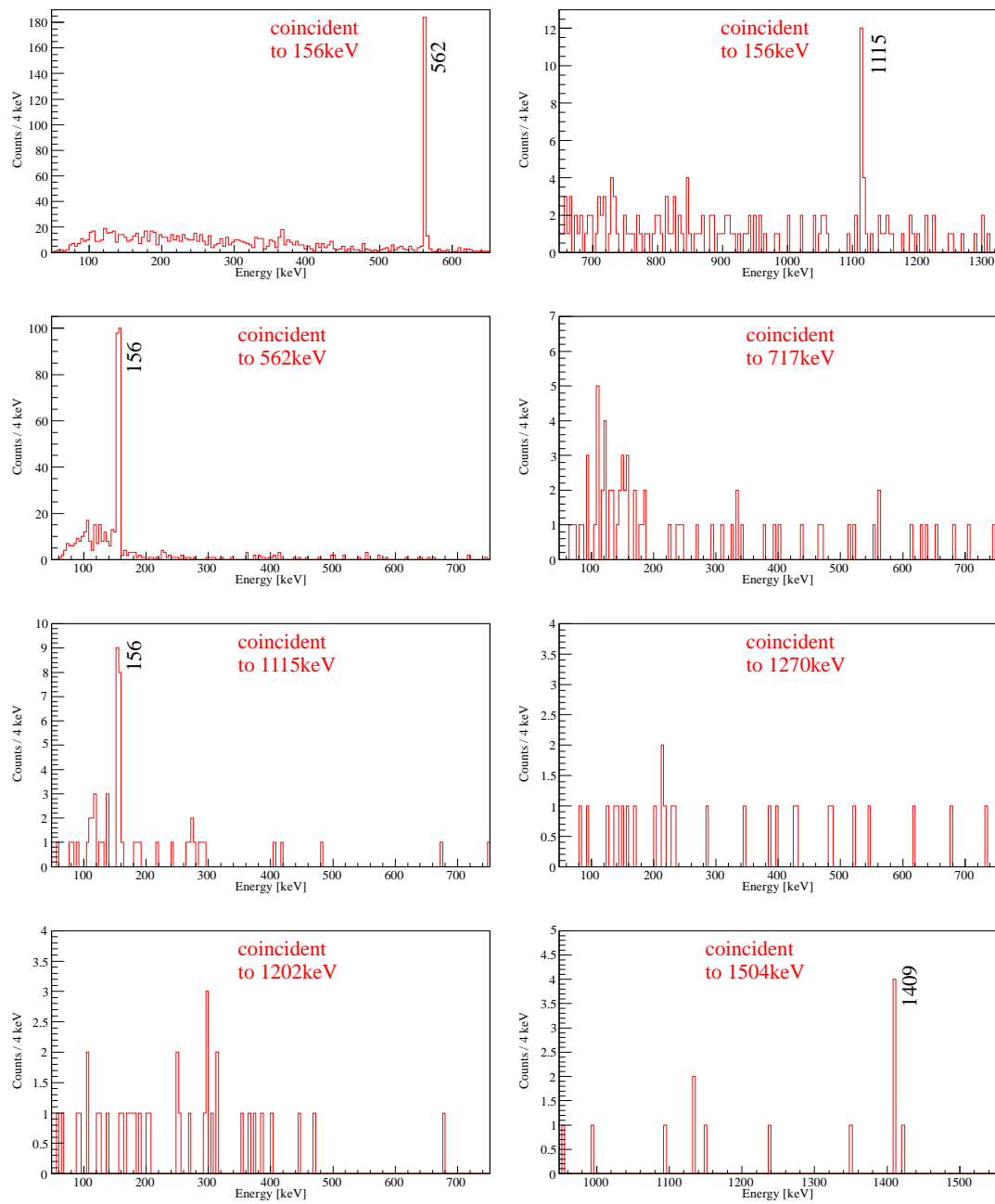
Figure 5.7: γ-γ coincidence spectra after the decay of ^{37}Al within 10 ms after an implantation, gated on the transition indicated in the spectra. The line at 156 keV is coincident with the lines at 562 and 1115 keV. A comparison of the numbers of the 156-562 keV and 156-1115 keV coincident events is consistent with the assumption that each 562 or 1115 keV transition is followed by a 156 keV transition. The line at 1504 keV is coincident with the line at 1409 keV, which originates from ^{36}Si.

energy [keV]	intensity [%] this experiment	origin
156	100(4)	^{37}Si (this work)
562	95(6)	^{37}Si (this work)
717	40(4)	^{37}Si (this work)
910	2(3)	^{35}Si [Num01]
1115	14(4)	^{37}Si (this work)
1202	11(4)	^{37}Si (this work)
1270	16(4)	^{37}Si (this work)
1409	71(7)	^{36}Si [Lia06]
1441	9(3)	^{36}Si [Lia06]
1504	10(3)	^{36}Si (this work)

Table 5.2: Relative intensities of β-delayed γ-rays after the decay of ^{37}Al, normalized to the γ-ray at an energy of 156 keV and corrected for efficiency.

5.2.1 Shell model calculations for ^{37}Si

^{37}Si has an odd number of neutrons ($N = 23$). In the "normal" 0 particle 0 hole (0p-0h) configuration there is a closed $N = 20$ core and 3 neutrons occupy the fp-shell. The orbital angular momentum is $l = 1\hbar$ for a neutron in the p-subshells and $l = 3\hbar$ in the f-subshells. The parity for each nucleon is $P = (-1)^l$. So a neutron in the fp-shell has a negative parity. Consequently 0p-0h states in ^{37}Si with three neutrons in the fp-shell have a negative parity, too. Only with a 1p-1h (or 3p-3h) configuration positive parity states are possible in ^{37}Si. Figure 5.8 shows an illustration of the β decay of ^{37}Al to ^{37}Si. The shell gaps at the classical magic numbers 8, 20, 28 and 40 are marked with dashed lines. An allowed Gamow-Teller transition is only possible to positive parity states in ^{37}Si.

Two calculations with the SDPF-U and SDPF-MU interactions were performed to compare the experiment with the shell model:

SDPF-U

This shell model calculation was carried out with the code ANTOINE [Cau99, Cau04, Cau05]. For the calculation the SDPF-U effective interaction [Now09] was used. With this effective interaction it is possible to perform large-scale shell-model calculations in the sd-pf valence space for nuclei with proton number ranging from $Z = 8$ to $Z = 20$ and neutron number from $N = 20$ to $N = 40$.

Two different calculations were performed:

- "neutrons only": Calculations with a closed $Z = 14$ core and a neutron fp-valence space. Only the $\pi d_{5/2}$ subshell is open for protons. The valence neutrons can occupy the $\nu f_{7/2}$, $\nu p_{3/2}$, $\nu f_{5/2}$ and $\nu p_{1/2}$ subshells beyond a closed $N = 20$ core.

- "full": Calculations with a full sd proton and fp neutron valence space. The
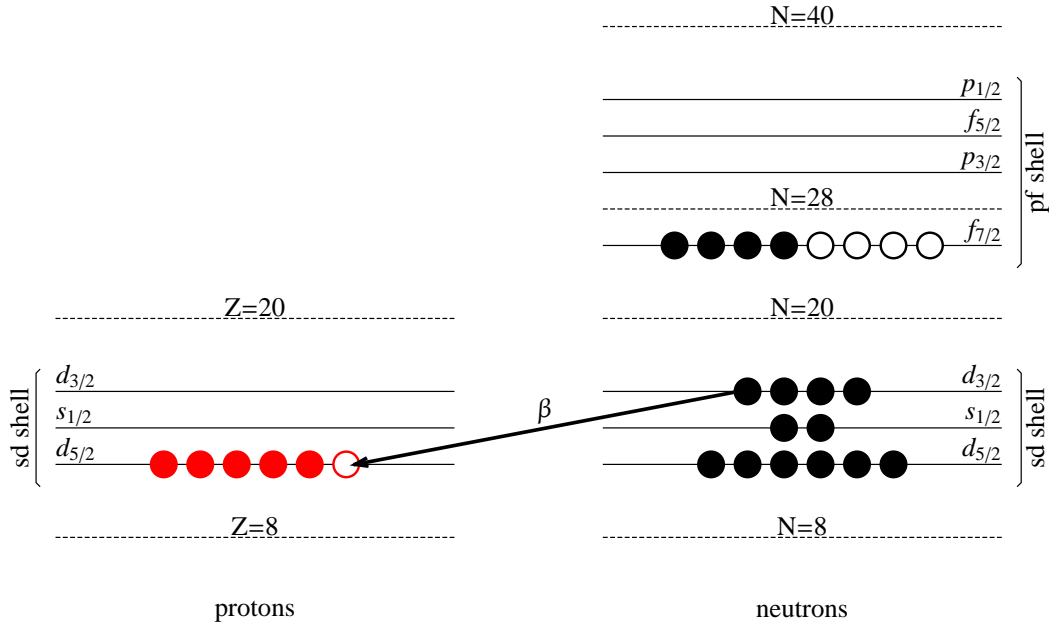
Figure 5.8: Schematic illustration of the ^{37}Al β decay. Filled circles represent particles, open circles holes. A $d_{3/2}$ neutron gets transformed into a $d_{5/2}$ proton. The ^{37}Si levels fed by the β decay have a $(\nu d_{3/2})^{-1}$ configuration. The transitions of a $d_{3/2}$ neutron into a $d_{3/2}$ proton or of a $s_{1/2}$ neutron into a $s_{1/2}$ proton are allowed Gamow-Teller decays, too. But these decays have two unpaired protons in the final state and therefore the excitation energy is not decreased by the pairing energy. Consequently these transitions populate states with energies which are probably beyond the neutron separation energy in ^{37}Si and decay by β-delayed neutron emission.

> $\pi d_{5/2}$, $\pi s_{1/2}$ and $\pi d_{3/2}$ subshells beyond a $Z = 8$ core are open for protons and the $\nu f_{7/2}$, $\nu p_{3/2}$, $\nu f_{5/2}$ and $\nu p_{1/2}$ subshells beyond a closed $N = 20$ core are open for neutrons.

Only states with no intruder configuration were calculated (no particle-hole excitations across the $N = 20$ shell gap). The single-particle energies (SPEs) for the different orbits on a core of ^{16}O are the following: $0d_{5/2} = 3.70\,\text{MeV}$; $1s_{1/2} = 2.92\,\text{MeV}$; $0d_{3/2} = 1.90\,\text{MeV}$; $0f_{7/2} = 6.22\,\text{MeV}$; $1p_{3/2} = 6.31\,\text{MeV}$; $0f_{5/2} = 11.45\,\text{MeV}$; $1p_{1/2} = 6.48\,\text{MeV}$ [Now09]. The shell model calculation can also predict the subshell components of the different states. The (electric) effective charges used in the calculations were $q_\pi = 1.35$ and $q_\nu = 0.35$, respectively, as suggested in [Now09]. The magnetic charges were quenched in the spin part by a factor of $q = 0.75$ [Sie11]. Instead of using the bare values of $g_{\text{s bare proton}} = 5.586$ and $g_{\text{s bare neutron}} = -3.826$ the quenched values of $g_{\text{s quench proton}} = 4.1895$ and $g_{\text{s quench neutron}} = -2.8695$ were used for protons and neutrons, respectively. For the magnetic orbital charges $g_{\text{L proton}} = 1.1$ and

$g_{\text{L neutron}} = -0.1$ were used.

SDPF-MU

With the SDPF-MU interaction [Uts12] both negative parity states in the 0p-0h configuration and positive parity states in the 1p-1h space are obtained. So for negative parity states the valence space is equal to the one for the "full" SDPF-U calculations. For positive parity states particle-hole excitations across the $N = 20$ shell gap are allowed. The single-particle energies (SPEs) and two-body matrix elements (TBMEs) used in the SDPF-MU calculations are based on previous existing interactions: The SPEs and TBMEs of the sd shell are taken from USD [Bro88], and the TBMEs of the pf shell from GXPF1B [Hon05, Hon08]. The SPEs of the pf shell are determined by requesting their effective SPEs on top of the ^{40}Ca closed shell equal to the SPEs of GXPF1B [Uts12]. The sd-pf cross-shell interaction is given by a monopole-based universal interaction V_{MU} [Ots08, Ots10], which includes the tensor force (see chapter 1).

The B_{GT} value (without the quenching factor) is defined as

$$B_{GT}(i \rightarrow f) = \frac{|\langle f|\sigma\tau_-|i\rangle|^2}{(2J_i + 1)}. \tag{5.2}$$

The initial and final states are denoted with $|i\rangle$ and $|f\rangle$, the angular momentum of the initial state is J_i. The isospin operator which changes the z-component of the isospin of the nucleon and transforms a neutron into a proton is τ_- and the spin operator σ changes the spin of the transformed nucleon.

To compare theoretical B_{GT} values to experimental values (see next section), a quenching factor is needed. Although there is little knowledge about the quenching factor in this model space, the standard quenching factor for the pf shell $q = 0.77$ is used and the (electric) effective charges used in the calculations were $q_\pi = 1.20$ and $q_\nu = 0.45$, respectively [Uts13].

5.2.2 Comparison of the experimental and SDPF-MU level schemes

Figure 5.9 shows a comparison of the experimental level scheme and shell model calculations for ^{37}Si. An interpretation of the experimental data is given in the following subsections.

Ground state and excited states at 156, 717 and 1270 keV

The experimental results in this section show that there are excited states in ^{37}Si with energies of 156, 717 and 1270 keV. The relative γ-intensities (see table 5.2) suggest that the 156 keV level is not directly populated by the β decay but is fed by γ-transitions from the 717 and 1270 keV levels. These two levels are likely to be directly populated by the β decay as no γ-transitions feeding these levels have been observed. The ground state of the β decay parent nucleus ^{37}Al is calculated to have $J^P = 5/2^+$ with both the SDPF-MU and SDPF-U effective interactions. Thus, assuming that the ground state
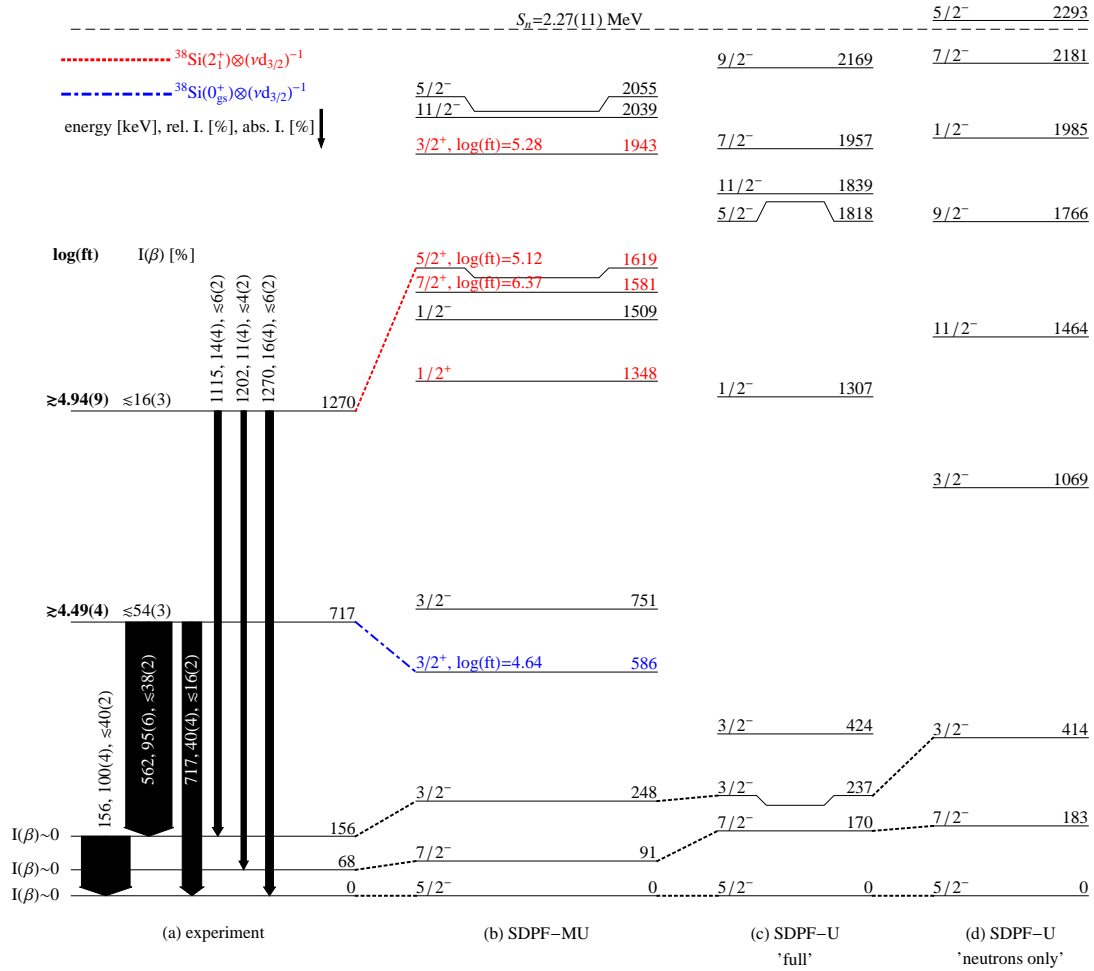
Figure 5.9: Comparison of the experimental level scheme and shell model calculations of ^{37}Si.

(a) Experimental level scheme. The γ-transitions are labeled with the γ-energy in keV, the γ-intensities relative to the 156 keV transition in % and the absolute γ-intensities in %.

(b) Shell model calculation using the SDPF-MU interaction.

(c) Shell model calculation with the SDPF-U interaction using the 'full' valence space.

(d) SDPF-U using the 'neutrons only' valence space.

Both calculations with SDPF-U do not include neutron intruder configurations in the model space and therefore only negative parity states are calculated.

in ^{37}Al is indeed a $5/2^+$ level an allowed Gamow-Teller (GT) transition is only possible to $3/2^+$, $5/2^+$ or $7/2^+$ states in ^{37}Si. Only these J^P values are possible for the 717 and 1270 keV levels. The SDPF-MU calculation predicts five states with an even parity below the neutron separation energy of $S_n = 2.27(11)$ MeV [Wan12]. All these states

are dominated by a 1-hole configuration in the neutron $d_{3/2}$ shell relative to the even-even ^{38}Si nucleus: The $3/2_1^+$ state is dominated by a ^{38}Si $(0_{gs}^+) \otimes (\nu d_{3/2})^{-1}$ configuration, while the other positive parity states $1/2_1^+$, $3/2_2^+$, $5/2_1^+$ and $7/2_1^+$ are dominated by a ^{38}Si $(2_1^+) \otimes (\nu d_{3/2})^{-1}$ configuration. A simplified illustration of the β decay of ^{37}Al to ^{37}Si is shown in figure 5.8: A $d_{3/2}$ neutron gets transformed into a $d_{5/2}$ proton by an allowed Gamow-Teller decay. The transitions of a $d_{3/2}$ neutron into a $d_{3/2}$ proton or of a $s_{1/2}$ neutron into a $s_{1/2}$ proton are allowed Fermi or Gamow-Teller decays, too. But at these decays the final states have no closed proton $d_{5/2}$ subshell and therefore the excitation energy is not decreased by the pairing energy. Consequently these transitions populate states with energies which are probably beyond the neutron separation energy in ^{37}Si and decay by β-delayed neutron emission. So only the Gamow-Teller strength B_{GT} but not the Fermi strength B_F must be considered for decays to states in ^{37}Al with excitation energies smaller than the neutron separation energy S_n. The ^{37}Si levels fed by the β decay have a $(\nu d_{3/2})^{-1}$ configuration.

The calculated B_{GT} and $\log(ft)$ values are shown in table 5.3. The B_{GT} value for the decay to the $3/2_1^+$ state is the largest one because this state has a large overlap of its wave function with the ground state of ^{37}Al, which has a predominant 0^+ configuration in the neutron part of its wave function. Comparing the excitation energies and the $\log(ft)$ values of the SDPF-MU calculation with the experiment the 717 keV state is likely to correspond to the $3/2_1^+$ state. This assignment is reasonable as the $3/2_1^+$ state has the smallest calculated $\log(ft)$ value of all states and is close in the excitation energy to the 717 keV state. Although the 1270 keV state is close in energy to the $1/2_1^+$ state in the SDPF-MU calculation, this spin-parity assignment is not possible because it cannot be populated in an allowed β decay from the $5/2^+$ ground state of ^{37}Al. Therefore the 1270 keV state should correspond to the $5/2_1^+$ state although the calculated excitation energy is 0.35 MeV too high. The high location of the $5/2_1^+$ state compared to the experiment is partly accounted for by the predicted properties of the 2_1^+ state in ^{38}Si. From the weak coupling picture the four states with the ^{38}Si $(2_1^+) \otimes (\nu d_{3/2})^{-1}$ configuration are located higher than the $3/2_1^+$ state by the excitation energy of the 2_1^+ state of ^{38}Si. The SDPF-MU interaction locates the 2_1^+ state of ^{38}Si about 0.2 MeV higher than the experimental value. An illustration of this deviation can be seen in figure 5.10. Another explanation for the deviation of the excitation energy of the 1270 keV state in comparison to the SDPF-MU calculation is given by the angular-coupling of two-body matrix elements. In the ideal weak coupling picture

E [keV]	J^P	B_{GT}	$\log(ft)$
586	$3/2_1^+$	0.1505	4.64
1581	$7/2_1^+$	0.0028	6.37
1619	$5/2_1^+$	0.0492	5.12
1943	$3/2_2^+$	0.0341	5.28

Table 5.3: SDPF-MU calculation of $\log(ft)$ and B_{GT} values for the positive parity states in ^{37}Si, which could be populated by an allowed β decay.
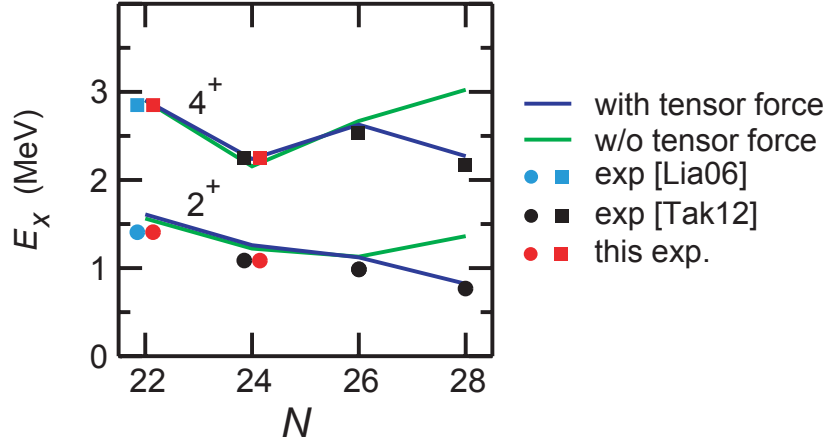
Figure 5.10: Energies of the 2_1^+ and 4_1^+ levels of Si isotopes with an even neutron number from $N = 22-28$. The blue, black and red symbols are experimental data from [Tak12], [Lia06] and this experiment, respectively. The blue (green) lines are SDPF-MU calculations with (without) the cross-shell tensor force. The excitation energy of the 2_1^+ state in ^{38}Si ($N = 24$) is 0.2 MeV too high compared to experimental results. Adopted from [Uts12].

the $1/2_1^+$, $3/2_2^+$, $5/2_1^+$, and $7/2_1^+$ states are located at the same excitation energy. This degeneracy is broken as seen in the calculation due to the angular-momentum dependence of interaction matrix elements. Because of these reasons the deviation in the excitation energy of the $5/2_1^+$ state is possible.

As the 156 keV state is populated by transitions from the $3/2_1^+$ and $5/2_1^+$ states it should be assigned to the $3/2_1^-$ state in the SDPF-MU calculation. An assignment of the 156 keV state to the $7/2_1^-$ state which is also near in excitation energy can be excluded because this would lead to a γ-feeding of a $7/2^-$ state from a $3/2^+$ state by an M2/E3 transition which cannot compete with a E1 transition from the $3/2_1^+$ state to the $5/2_1^-$ ground state. The ground state is populated, in addition to the 156 keV transition, by transitions from the $3/2_1^+$ state at 717 keV and the $5/2_1^+$ state at 1270 keV. These transitions can compete with the 562 and 1115 keV E1 transitions to the 156 keV state. Thus an assignment of the ground state to the $7/2_1^-$ state in the SDPF-MU calculation can be excluded as in this case the 717 keV transition would have a multipolarity of M2/E3 and could not compete with the 562 keV transition. Consequently the ground state can be unambiguously assigned to the $5/2_{gs}^-$ state from the shell model calculation. With this assignment the multipolarities of the 717 and 1270 keV transitions are both E1.

Placement of the 1202 keV transition

For the measured γ-transitions with the energy of 1202 keV the following scenario is suggested: As this transition is not in coincidence with the other measured transitions

(see figure 5.7) it should neither populate the 156 keV state nor the 717 keV state because then a coincidence with the 156, 562 or 717 keV lines should be measured: If the 1202 keV transition was emitted in coincidence with the 156 keV line one would expect about 11 detected events in the γ-γ coincidence spectrum (from a comparison of the relative γ-intensities). But no coincident events were measured. A population of the 1270 keV level can also be excluded as then the 1202 keV line would originate from a state which has an excitation energy larger than the neutron separation energy $S_n = 2.27(11)$ MeV [Wan12]. Consequently the 1202 keV transition must either populate the $5/2_1^-$ ground state or the $7/2_1^-$ first excited state.

The 1202 keV transition could originate from a 1202 keV state which is deexcited by a ground state transition. In this assumption the 1202 keV state can only correspond to the $7/2_1^+$ state in the SDPF-MU level scheme as it should be directly populated by the β decay and this state is the only one close in excitation energy. But as the calculated $\log(ft)$ value for this state is very large it should only be populated by less than a percent of all β decays of ^{37}Al which is inconsistent with the observed intensity for this transition. Therefore, this assumption is unlikely. A better placement of the 1202 keV line is a transition from the 1270 keV state to a possible 68 keV state. The 68 keV state can be assigned to the $7/2_1^-$ state in the SDPF-MU calculation. The non-observation of the 68 keV ground state transition can be explained by four possible reasons: A small amount of feeding to this state (only the low-intensity 1202 keV line feeds this state), a possibly small γ-ray efficiency below 100 keV (see section A.2 in the appendix), a large conversion coefficient and most important a large amount of background causing large statistical fluctuations in the background subtracted γ-ray spectrum at this energy. So it is consistent to have 3 transitions with the energies of 1115, 1202 and 1270 keV which deexcite the 1270 keV state. They have a similar intensity and are all E1 transitions.

However since this transition is not coincident with any other transitions in ^{37}Si, it can not be excluded that the 1202 keV transition originates from states in ^{36}Si or ^{35}Si which are populated by β-delayed one- or two-neutron emission. If this is the case then the probabilities for β-delayed neutron emission discussed later would increase.

Spin and parity assignments

Table 5.4 shows the suggested spin and parity assignment for the ground state and the excited levels in ^{37}Si. With these assignments from the comparison of the experimental results with the SDPF-MU calculations the γ-transitions with 562, 717, 1115, 1202 and 1270 keV are all E1 transitions. The only observed transition with another multipolarity is the M1/E2 ground state transition from the 156 keV state. The non-observed 68 keV transition from the inferred first excited state to the ground state should also have an M1/E2 multipolarity.

log(ft) values and beta-delayed neutron emission

There is no direct way to determine the β-delayed neutron branching ratios $P(n)$ and $P(2n)$ of ^{37}Al with this experiment. The method of comparing the intensities

E_{exp} [keV]	β-branching [%]	$\log(ft)_{\text{exp}}$	$E_{\text{SDPF-MU}}$ [keV]	J^P	$\log(ft)_{\text{SDPF-MU}}$
0	~ 0		0	$5/2^-_1$	
68	~ 0		91	$7/2^-_1$	
156	~ 0		248	$3/2^-_1$	
717	$\leq 54(3)$	$\geq 4.49(4)$	586	$3/2^+_1$	4.64
1270	$\leq 16(3)$	$\geq 4.94(9)$	1691	$5/2^+_1$	5.12
^{36}Si	$P(n) \geq 29(3)$				
^{35}Si	$P(2n) \geq 1(1)$				

Table 5.4: β-branching ratios, $\log(ft)$ values and tentative spin and parity assignments of the levels in ^{37}Si. The $\log(ft)$ values calculated with the SDPF-MU interaction are shown for comparison. The β-branching ratios, $P(n)$ and $P(2n)$ values are normalized and their sum is 100%.

of γ-transitions in granddaughter nuclei $^{35-37}$P is not applicable as the β-branching ratios of the decays of $^{35-37}$Si are not known. But it is possible to give a lower limit for $P(n)$ and $P(2n)$: Assuming that the ground state of ^{36}Si is not populated by a β-n decay of ^{37}Al there is an emission of the 1409 keV $2^+_1 \to 0^+_{gs}$ line in ^{36}Si after each of these decays. The same estimate can be done for the β-2n decay to ^{35}Si and the 910 keV $3/2^-_1 \to 7/2^-_{gs}$ transition. With these assumptions one can convert the relative γ-intensities of table 5.2 into upper limits for β-branching ratios and lower limits for $P(n)$, $P(2n)$ and $\log(ft)$ values shown in table 5.4. The experimental $\log(ft)$ values are calculated with the input parameters $Q_\beta(^{37}\text{Al}) = 16.40(15)$ MeV [Wan12], the experimental half-life $t_{1/2}(^{37}\text{Al}) = 11.5(4)$ ms derived in section 4.2 and the β-branching ratios. For the states at 717 and 1270 keV there is a good agreement of their experimental $\log(ft)$ values of $\log(ft)_{717\,\text{keV}} \geq 4.49(4)$ and $\log(ft)_{1270\,\text{keV}} \geq 4.94(9)$ with the $\log(ft)$ values of the SDPF-MU calculation 4.64 and 5.12. The lower limits of the β-delayed neutron branching ratios are $P(n) \geq 29(3)$ and $P(2n) \geq 1(1)$. For the probability of a β-delayed neutron emission of ^{37}Al there is a preliminary result of $P_x(n) = \sum_{i=1}^{\infty} i \cdot P(in) = 55(11)$ % [Yon99] which is a composition of the probabilities for β-delayed (multi-)neutron emission.

Comparison of the SDPF-MU and SDPF-U calculations

As only negative parity states are calculated with the SDPF-U interaction only these states can be compared to the calculation with the SDPF-MU interaction. Experimentally only 3 negative parity states are populated by γ-rays: The $5/2^-_{gs}$ ground state and the $7/2^-_1$ and $3/2^-_1$ excited states with the lowest excitation energies. The experimental relative energies of all these three states are reproduced well by both the SDPF-MU and the SDPF-U 'full' calculation in a good agreement. As the SDPF-U 'neutrons only' calculation restricts the valence space for protons, it produces a deviation from the 'full' calculation. Such a deviation of the 'neutrons only' to the 'full' SDPF-U

calculation was also reported in ^{39}Si and ^{41}Si [Soh11].

5.2.3 Data from a previous Coulomb excitation experiment

There was no experimental information about any excited level in ^{37}Si except from an experiment performing Coulomb excitation [Ibb99]. This reference reports a γ-ray transition at an energy of 1437(27) keV. However the authors are not sure about the origin of the 1437(27) keV γ-ray. [Ibb99]: "The observed γ rays in ^{35}Al and ^{37}Si could possibly result from stripping reactions in the target, leading to neighboring isotopes of Al and Si, respectively. Since the γ-ray yield in these two nuclei is small, this possibility could not be discounted by examination of the measured scattered-particle energy."

Since the Coulomb excitation proceeds predominantly via E2 transitions [Ibb99] only negative parity states can be populated in that experiment as there is a $5/2^-$ ground state. This is complementary to the β decay experiment that only populates positive parity states. So neither a confirmation nor an exclusion of a 1437 keV transition attributed to ^{37}Si is possible with the present experimental data. Comparing this excitation energy to the SDPF-MU calculation in figure 5.9 a possible candidate for the measured 1437 keV state is the $1/2_1^-$ state at 1509 keV which is close in energy and cannot be directly populated by the β decay due to its spin and parity.

5.3 Decay of ^{38}Al

The β-delayed γ-ray spectrum after the decay of ^{38}Al is shown in figure 5.11. Previously unknown γ-lines with energies of 68, 156, 418, 1074, 1159, 1470, 2211 and 3656 keV were measured for the first time. All other lines disappear in the background subtracted spectrum because they do not originate from the ^{38}Al decay (except the γ-line with an energy of 156 keV which corresponds to the $3/2_1^- \rightarrow 5/2_{gs}^-$ transitions in the β-n daughter ^{37}Si as shown in the previous section). As shown in figure 5.12 all previously unknown lines are prompt lines which have their maximum intensity within the first time window from 0 to 10 ms of an implantation-decay correlation. Consequently they all correspond to a deexcitation in the daughter ^{38}Si or in the β-n or β-2n daughters ^{36,37}Si. Table 5.5 gives the efficiency corrected relative intensities of the β-delayed γ-rays after the decay of ^{38}Al.

A recent publication [Tak12] reports on the results of an in-beam γ-ray spectroscopy experiment studying the very neutron rich isotopes ^{38,40,42}Si. This experiment was performed during the same BigRIPS campaign as the CAITEN experiment discussed in this thesis. ^{38}Si was investigated by a multi-nucleon removal reaction in a carbon target. Three γ-peaks at the energies 1071(12), 1168(22) and 1284(26) keV were measured (see appendix section A.4 for details). The 1071(12) keV transition corresponds to the $2_1^+ \rightarrow 0_{gs}^+$ transition. According to [Tak12] either the peak at 1168(22) keV or at 1284(26) keV is the $4_1^+ \rightarrow 2_1^+$ transition. Comparing these results to the β-delayed γ-rays at the decay of ^{38}Al the 1074 keV peak is most probable the $2_1^+ \rightarrow 0_{gs}^+$ transition and the 1159 keV line is a candidate for the $4_1^+ \rightarrow 2_1^+$ transition.
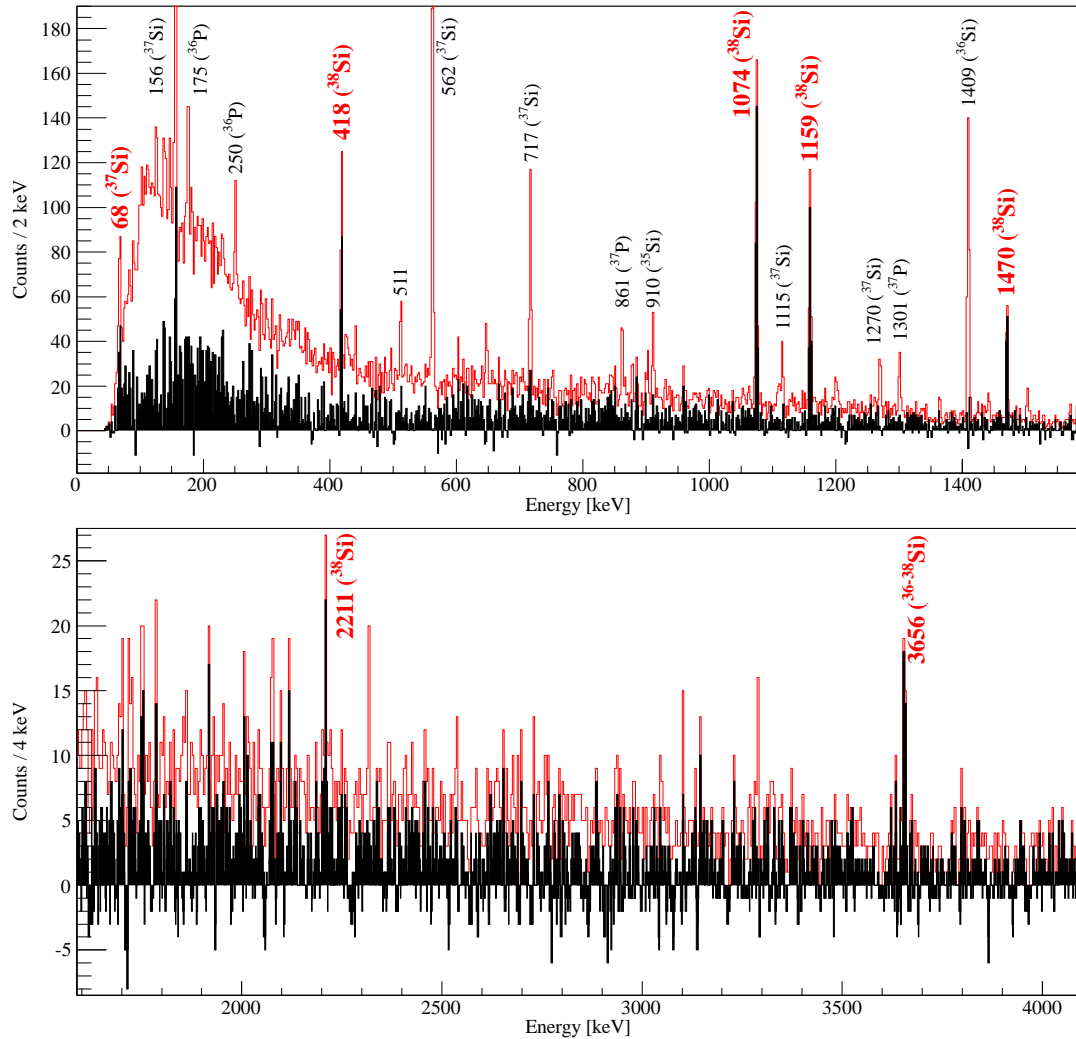
Figure 5.11: β-delayed γ-ray spectrum after the decay of ^{38}Al. The black (red) spectrum corresponds to implantation-decay correlations with(out) background subtraction within 10 ms after an implantation. Lines which could originate from the daughter ^{38}Si are marked in red.

The energy available for the β decay of ^{38}Al is $Q_\beta(^{38}\text{Al}) = 20.38(26)$ MeV and the neutron separation energies of ^{38}Si are $S_n = 5.65(11)$ MeV and $S_{2n} = 7.92(10)$ MeV [Wan12]. There is no experimental result for the β-delayed neutron emission probability except a preliminary one of $P_x(n) = \sum_{i=1}^{\infty} i \cdot P(in) = 84(19)\%$ [Yon99]. This value is a composition of the probabilities for β-delayed (multi-)neutron emission.

A γ-γ coincidence spectrum after the decay of ^{38}Al is shown in figure 5.13. Gating on the 1074 keV transition there are four coincident events at 418 keV, two events at 1470 keV and one event each at 1159 and 2211 keV. By the shape of this coincidence
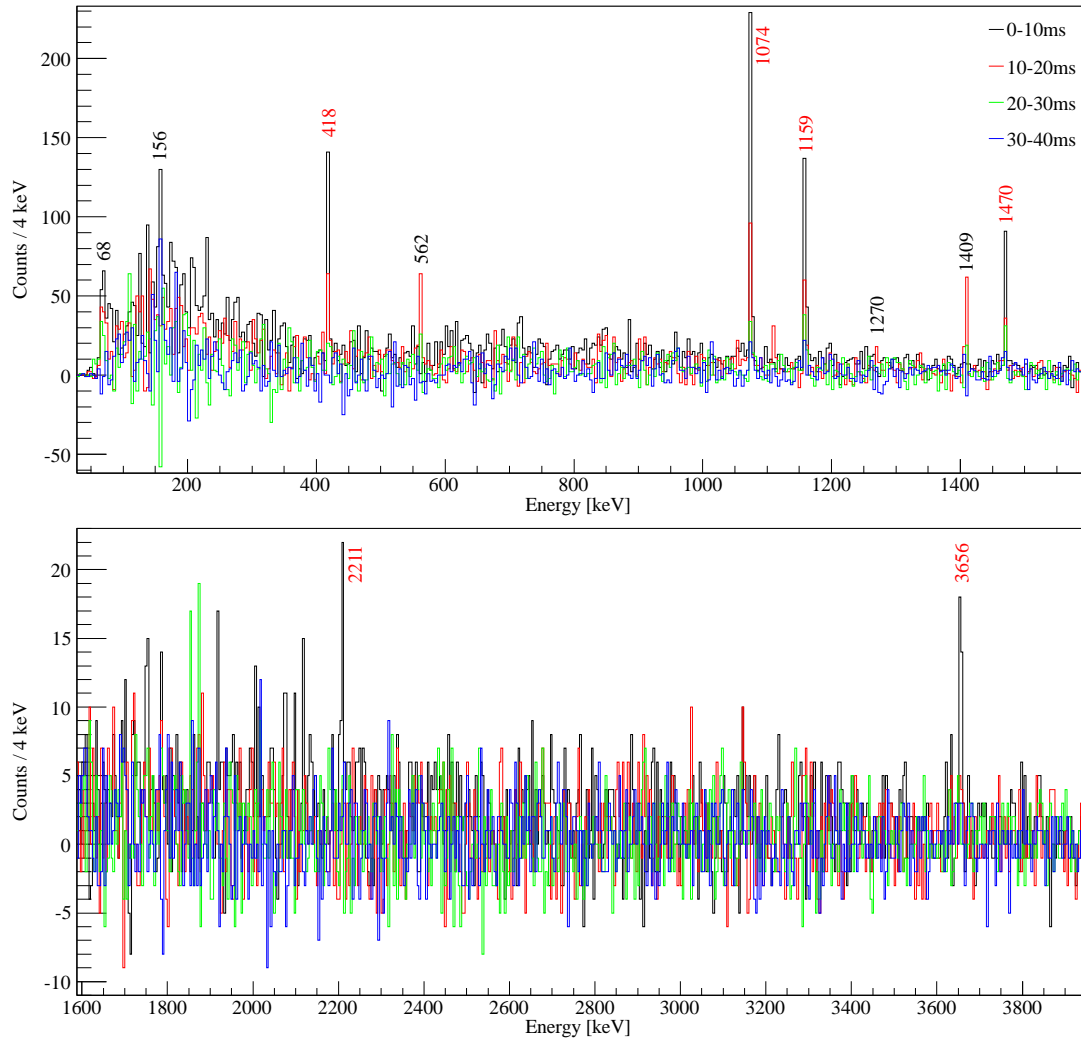
Figure 5.12: Background subtracted β-delayed γ-ray spectrum after the decay of ^{38}Al. The black, red, green and blue spectra correspond to implantation-decay correlations time windows with a width of 10 ms (see legend). Lines from transitions in the daughter ^{38}Si are marked in red.

spectrum one can estimate the energy dependent probability to have a background event at a specific energy: In a 4 keV interval at 418, 1159, 1470 and 2211 keV this probability is approximately 15%, 6%, 4% and 2%, respectively. Only a small number of coincident events compared to the number of coincidences measured after the decay of ^{37}Al (see appendix section A.5 for the details of the calculation of the expected number of coincident events) is expected. The table 5.6 shows the detected numbers of coincident events and the expected number of coincident events assuming a cascade of two γ-rays. Assuming that each of the transitions is followed by a 1074 keV transi-
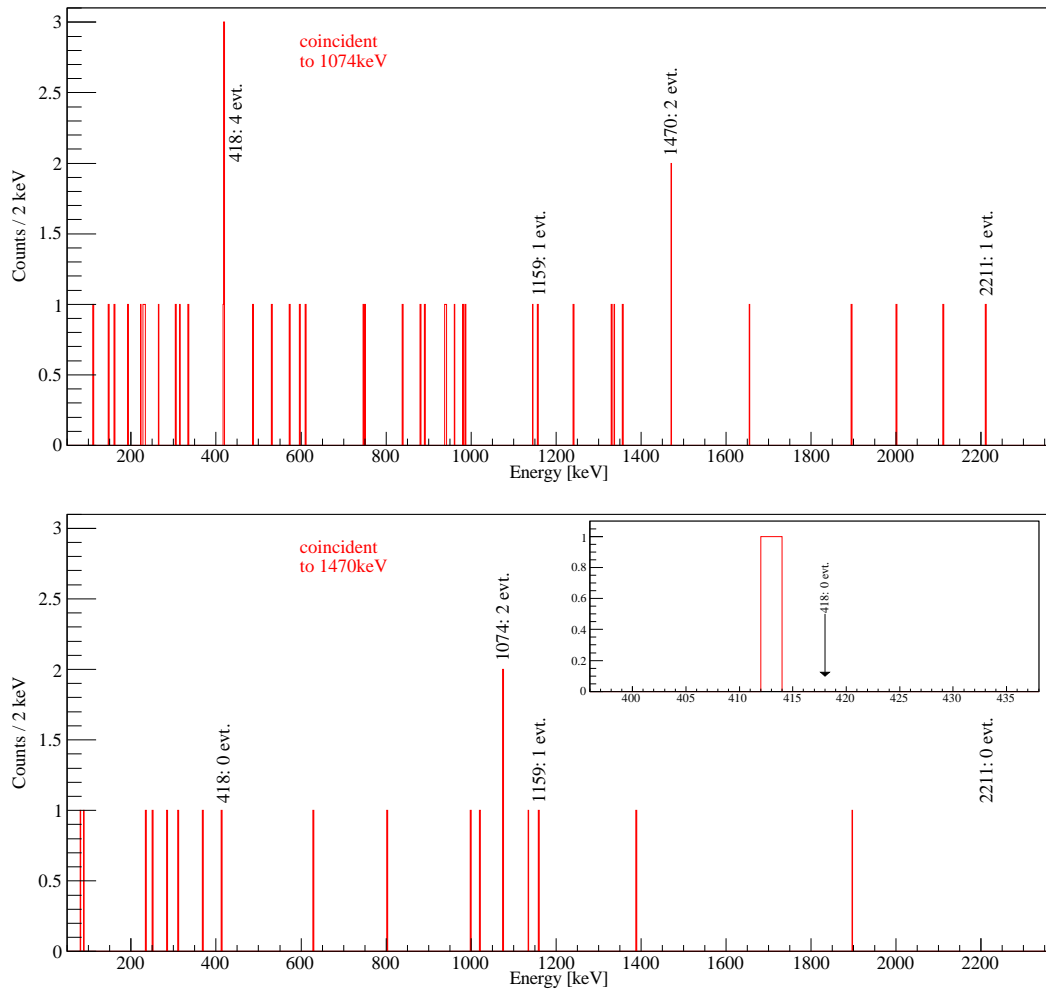
Figure 5.13: γ-γ coincidence spectra after the decay of ^{38}Al within 10 ms after an implantation.
Top: Gated on the 1074 keV transition: The line at 1074 keV is coincident with four events at 418 keV, two events at 1470 keV and one event each at 1159 and 2211 keV.
Bottom: Gated on the 1470 keV transition: Two events at 1074 keV and one event at 1159 keV are measured.

tion approximately three coincident events at 418 keV, three events at 1159 keV, two events at 1470 keV and one event at 2211 keV are expected. Consequently the 418 keV transition can be assigned to a deexcitation in ^{38}Si which appears in the same cascade like the 1074 keV line. Four background events at (418 ± 2) keV can be excluded with a confidence level of 4.3σ (99.998%). In addition it is very probable that also the 1470 and 2211 keV lines are transitions in a cascade with 1074 keV. As there are two coincident events at 1470 keV and one coincident event at 2211 keV, these are exactly the

energy [keV]	intensity [%] this experiment	origin
68	> 7(2)*	^{37}Si
156	15(7)	^{37}Si
418	32(5)	^{38}Si
1074	100(12)	^{38}Si
1159	59(7)	^{38}Si
1470	42(5)	^{38}Si
2211	20(4)	^{38}Si
3656	16(4)	$^{36-38}$Si

Table 5.5: Relative intensities of β-delayed γ-rays after the decay of ^{38}Al, normalized to the γ-ray at an energy of 1074 keV and corrected for efficiency.
(*) The γ-ray efficiency below 100 keV is not known very accurately (see section A.2 in the appendix). In addition, as only γ-rays can be detected, the intensity of deexcitations by conversion are missed.

	1074 keV	1159 keV	1470 keV	2211 keV	3656 keV
418 keV	4/3	0/3	0/3	0/1	0/1
1074 keV		1/3	2/2	1/1	0/0
1159 keV			1/2	0/1	0/0
1470 keV				0/1	0/0
2211 keV					0/0

Table 5.6: Detected/expected number of coincident γ-γ events after the decay of ^{38}Al assuming that there is a cascade of γ-rays with the energy indicated in the top row and the left column. Within a confidence level of 2σ the following statements can be made: For cells marked in green coincident events were detected and the numbers of detected and expected events are consistent. A coincidence can be excluded for cells marked in red. Due to the very small number of expected events no statement is possible for cells marked with no color.

expected number of coincident events. They are no background with a probability of 96 and 98%, respectively. One coincident event is measured at 1159 keV, which is no background with a probability of 94%. As three events are expected at this energy if there was a cascade of the 1159 and 1074 keV lines the measured one event lies within a 2σ window of the expected number.

In the bottom part of figure 5.13 the γ-γ coincidence spectrum gated on the 1470 keV is shown. In addition to two coincident events with the 1074 keV transition, which were already discussed, there is one coincident event at 1159 keV. This event is no background with a probability of 97%. The expected number of measured coincidences is 2 if the 1470 keV transition is followed by a 1159 keV line. So a 1470-1159 keV coincidence is very likely. The sum energy of the transitions at 1159 and 1470 keV is equal to the

sum of the transitions at 2211 and 418 keV. Consequently there may be two cascades which connect states with an energy difference of 2629 keV. No statement can be made about a 2211-418 keV coincidence as only one coincident event is expected but no event is detected. A coincidence of the 418 keV line with the lines at 1159 and 1470 keV is unlikely (it can be excluded with a confidence level of 2σ) as no coincident events are detected but three events are expected if there was a coincidence. So a scenario with 2 parallel cascades is further supported by this non-observation.

The 68 keV line is likely to originate from a strong β-n decay branch to the 68 keV state in ^{37}Si. In contrast to after the decay of ^{37}Al, it is visible after the decay of ^{38}Al as the energy-dependent background is smaller by more than a factor of five. No statement can be made about the origin of the 3656 keV line except that it is emitted by one of the daughters $^{36-38}$Si after the decay of ^{38}Al. The expected numbers of coincident events with the 3656 keV line are equal or smaller than one for the 418, 1074, 1159, 1470 and 2211 keV transitions and no coincident event was detected.

5.3.1 Shell model calculation of the mother nucleus ^{38}Al

An important information for the interpretation of the β-delayed γ-rays is the spin and parity of the ground state of the mother nucleus ^{38}Al. A shell model calculation for ^{38}Al with the SDPF-MU effective interaction gives the following results: The ground state is calculated to be a $J^P = 0^-$ state. Above it low-lying states with $J^P = 5^-$ (391 keV), 2^- (449 keV) and 3^- (490 keV) are located. A calculation of the excitation energies of positive-parity states results in 2437 keV for the 0_1^+ state, 871 keV for the 1_1^+ state, 1007 keV for the 2_1^+ state, 1376 keV for the 3_1^+ state, 1073 keV for the 4_1^+ state and 1871 keV for the 5_1^+ state. These positive-parity states have a neutron 6p-1h configuration with respect to the $N = 20$ shell gap. Although the validity of SDPF-MU for unnatural parity states of Al isotopes has not been tested, it is not very likely that the ground state of ^{38}Al is a positive parity state [Uts13]. The order of the low-lying 0^-, 2^-, 3^- and 5^- states may differ from the calculation as their excitation energy is only a few hundred keV. So the ground state can have any of these spin and parity assignments. An additional possibility is the existence of an isomer: The first excited state could be the 3^- or 5^- state above a 0^- ground state. Then the β decay half-life of the isomer can probably compete with the half-life of the gamma decay with a E3 or E5 multipolarity.

5.3.2 Experimental level scheme and shell model calculation of ^{38}Si

Construction of the experimental level scheme

Figure 5.14 shows the experimental level scheme and shell model calculations for ^{38}Si. The 1074 keV line is assigned to the $2_1^+ \rightarrow 0_{\mathrm{gs}}^+$ transition and the 1159 keV line to the $4_1^+ \rightarrow 2_1^+$ transition as already discussed, resulting in an energy of 2233 keV for the 4_1^+ state. The sum energy of the transitions at 1159 and 1470 keV is equal to the sum of the transitions at 2211 and 418 keV. So it is very likely that there are two cascades with these energies which connect states with an energy difference of 2629 keV. As discussed
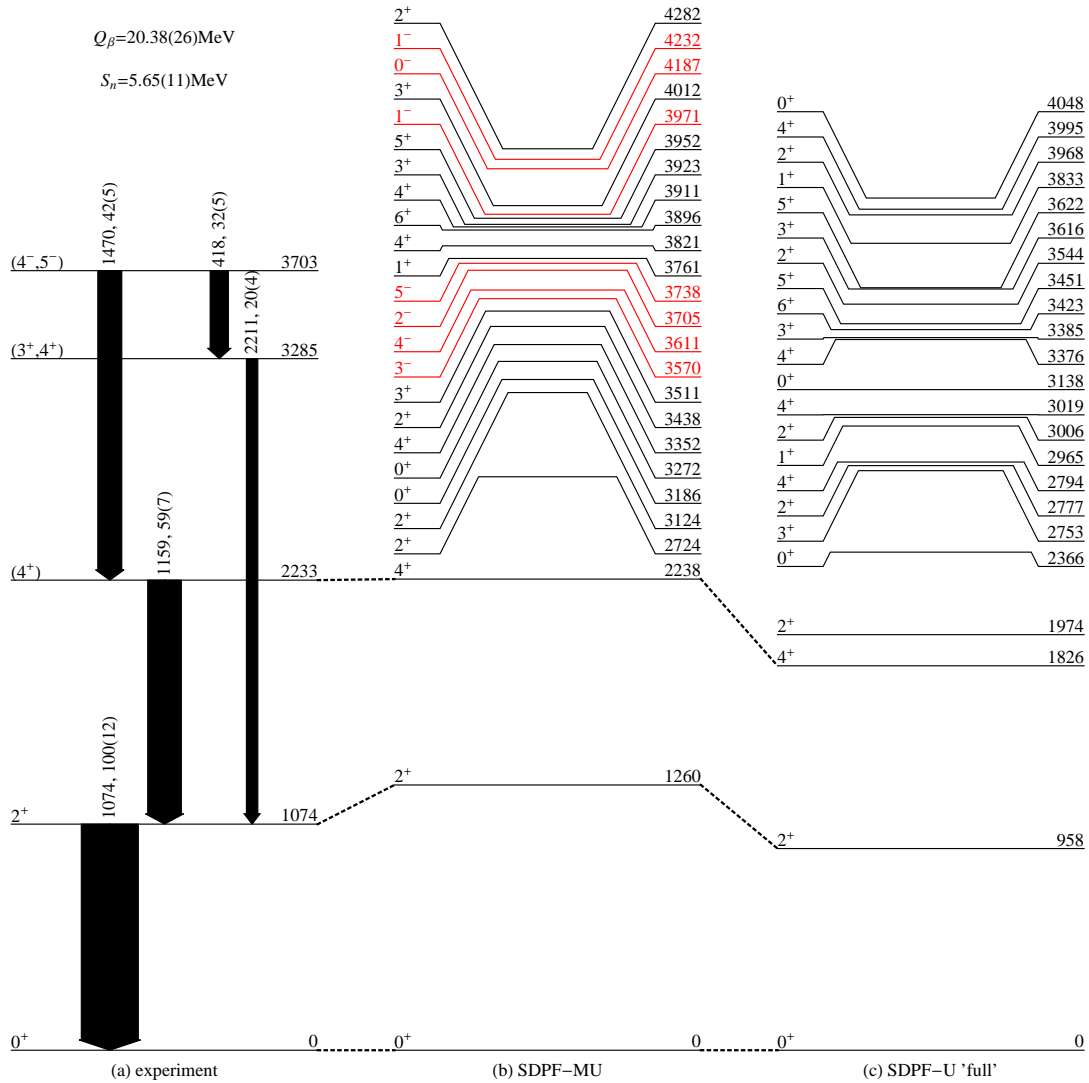
Figure 5.14: Comparison of the experimental level scheme and shell model calculations of ^{38}Si.

(a) Experimental level scheme. The γ-transitions are labeled with the γ-energy in keV, the γ-intensities relative to the 1074 keV transition in %. (b) Shell model calculation using the SDPF-MU interaction. (c) Shell model calculation with the SDPF-U interaction using the 'full' valence space. Both for SDPF-MU and SDPF-U excited states are calculated up to ~ 4 MeV.

before each of these four transitions is coincident to the 1074 keV line. Consequently a level at 3703 keV is proposed, which is connected to the 2233 keV level by a 1470 keV transition. The second cascade from the level at 3703 keV can either be a 2211 keV transition populating an excited state at 1492 keV followed by a 418 keV transition or

vice versa with an intermediate state at 3285 keV.

Comparison to the SDPF-MU shell model calculation

The SDPF-MU shell model calculation in figure 5.14 shows excited states in ^{38}Si up to ~ 4 MeV. The energy of the 2_1^+ level in the calculation differs by 0.2 MeV from the experimental result and the energy of the 4_1^+ states matches the experiment almost exactly. As no level is calculated to have an excitation energy of ~ 1.5 MeV the order of the 418-2211 keV cascade from the 3703 keV level can be deduced from this calculation: A cascade from the 3703 keV level, which is deexcited by a 2211 keV transition to a 1492 keV state followed by a 418 keV transition to the 2_1^+ state at 1074 keV, can be excluded. Consequently there is an excited state at 3285 keV, which is fed by a 418 keV transition from the 3703 keV level and is deexcited by a 2211 keV transition to the 2_1^+ state at 1074 keV.

As the ground state of ^{38}Al is calculated to have $J^P = 0^-$, 2^-, 3^- or 5^- an allowed β decay is only possible to states in ^{38}Si with a negative parity. The level at 3703 keV has the largest feeding intensity for the β decay and should therefore be a negative parity state. In the shell model calculation four states with $J^P = 2^-$, 3^-, 4^- and 5^- have excitation energies similar to the 3703 keV level. As the 2_1^+ state is not populated by deexcitations of this level a $J^P = 2^-$ or 3^- assignment can be excluded for the 3703 keV level but a 4^- or 5^- is favored. Consequently the ground state of ^{38}Al can tentatively be assigned to be a 3^- or 5^- state and the 1470 keV transition to the state at 2233 keV has a E1 multipolarity. The 418 keV transition can compete with the 1470 keV transition although its energy is ~ 3.5 times smaller. Therefore this transition must also have an E1 multipolarity and the state at 3285 keV must have $J^P = 3^+ - 6^+$. With this J^P restriction only one 3^+ and one 4^+ state (at 3511 keV and 3352 keV) in the SDPF-MU calculation have similar excitation energies as the level at 3285 keV in the experiment. So a $(3^+, 4^+)$ assignment for this level is favored. From the level at 3285 keV γ-rays to 2^+ states at energies around ~ 3 MeV (present in the SDPF-MU calculation) or the 4_1^+ state may be missed due to their low intensity. Consequently the 2211 keV transition deexciting the 3285 keV state can have a smaller intensity compared to the 418 keV transition feeding this state. The $\log(ft)$ value for the 3703 keV state can be estimated with the assumption that all β decays to ^{38}Al must emit a 1074 keV line and the sum of the intensities of the 68, 156 and 3656 keV lines is taken into account as a different branch of the β-feeding. With this method a $\log(ft)$ value of 4.44(9) is calculated for the 3703 keV state (with $t_{1/2} = 7.6(6)$ ms [Gré04], $Q_\beta = 20.38(26)$ MeV [Wan12] and a total branching ratio of 54(8)% to the 3703 keV state) supporting an allowed β decay to this state.

Only the calculation of positive parity states is possible with the SDPF-U interaction due to the restriction of the valence space with no excitation across the N=20 shell gap. Whereas the energy of the 2_1^+ state only has a deviation of 0.1 MeV to the experimental result the 4_1^+ energy differs by 0.4 MeV.

5.4 Decay of ^{36}Mg

The β-delayed γ-ray spectrum after the decay of ^{36}Mg is shown in figure 5.15: In the background-subtracted spectrum there are γ-rays at the energies 658, 804, 910, 1109 and 1409 keV. All other transitions disappear in the background-subtracted spectrum. The 910 and 1409 keV lines originate from the nuclei ^{35}Si and ^{36}Si, respectively, as already discussed in section 5.2. The energy available for the β decay of ^{36}Mg is $Q_\beta = 14.43(47)$ MeV and the one- and two-neutron separation energies of the daughter ^{36}Al are $S_n = 1.90(12)$ MeV and $S_{2n} = 7.12(12)$ MeV, respectively [Wan12]. The time evolution of the transitions is shown in figure 5.16. The 658 and 804 keV transitions are prompt lines which predominantly appear in the time window 0-10 ms after an implantation of ^{36}Mg. So they must originate from a deexcitation in one of the daughter nuclei $^{34-36}$Al. For the 1109 keV line the number of entries in the time window 0-10 ms is only half of those in the time window 10-20 ms. With the short half-life for ^{36}Mg of $7.6^{+0.5}_{-0.8}$ ms (this work) there should be at least a factor of two more decays in the first time window than in the second one, if the 1109 keV line originates from a daughter $^{34-36}$Al after the decay of ^{36}Mg. Consequently this 1109 keV line can be attributed to a γ-ray transition in one of the granddaughters $^{34-36}$Si as the half-lives of $^{34-36}$Al are $t_{1/2}(^{34}$Al$)$ =56.3(5) ms [Num01], $t_{1/2}(^{35}$Al$)$ = 37.2(8) ms [Eva12] and $t_{1/2}(^{36}$Al$)$ = 90(40) ms [Eva12], which is much longer than the time window of 10 ms. The 910 and 1409 keV lines which are also emitted by the granddaughter generation have their maximum intensities in the later time windows, too.

The reference [Pri01] reports a 657 ± 9 keV transition in ^{34}Al which was measured during a Coulomb excitation experiment. It connects an excited $(4)^-$ state with the 4^- ground state of ^{34}Al [Him08]. So it is very likely that the 658 keV line measured after the β decay of ^{36}Mg corresponds to this transition. For the 804 and 1109 keV lines no transitions can be found in literature. So from the present data one can only attribute them to the decay generations: The 804 keV line is a transition in a daughter $^{34-36}$Al and the 1109 keV line is a transition in a granddaughter $^{34-36}$Si nucleus, respectively. Table 5.7 gives a summary of the relative intensities and the origin of the measured transitions after the decay of ^{36}Mg.

If there was a cascade of two coincident γ-rays after the decay of ^{36}Mg one would expect only a small number of detected coincident events compared to the number of coincidences measured after the decay of ^{37}Al (see appendix section A.5). No coincident event of a pair of γ-rays with the energies 658, 804, 910, 1109 and 1409 keV was detected. If the 804 keV line was a transition in ^{34}Al which is emitted in coincidence with the 658 keV line one would expect four detected coincident events of this pair of γ-rays. As no events were measured one can exclude this assumption with a confidence level of 2σ. The same assumption can be made for the 1109 keV line with the 910 keV transition in ^{35}Si and the 1409 keV transition in ^{36}Si as it is not clear in which of the granddaughters $^{34-36}$Si the 1109 keV line is emitted. If the 1109 keV line is emitted in coincidence with the 910 or 1409 keV line, respectively, one would expect one detected coincident event. Neither for the 1109-910 keV pair nor the 1109-1409 keV pair a coincident event was measured. But as the expected number of coincident events is only one no statement
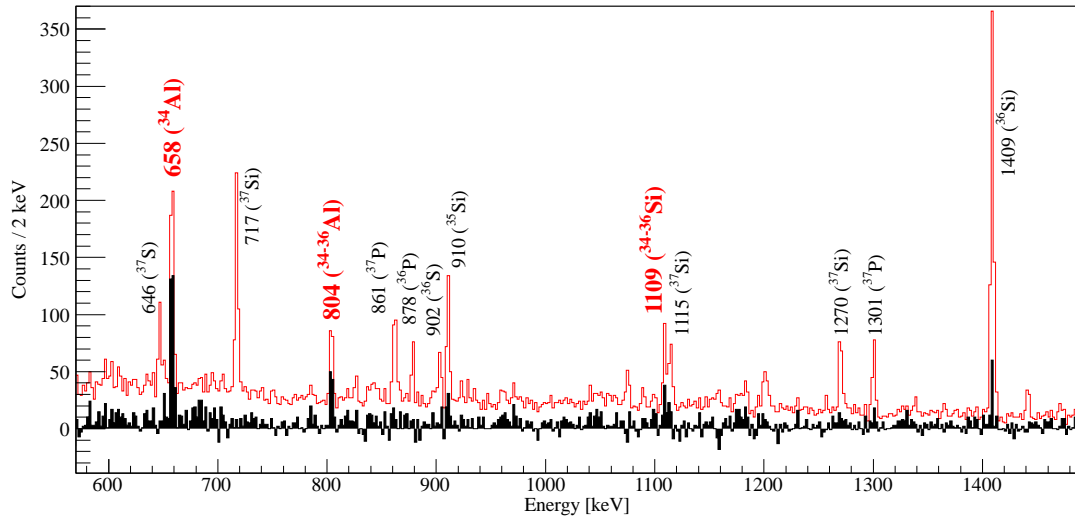
Figure 5.15: β-delayed γ-ray spectrum after the decay of ^{36}Mg. The black (red) spectrum corresponds to implantation-decay correlations with(out) background subtraction within 10 ms after an implantation.
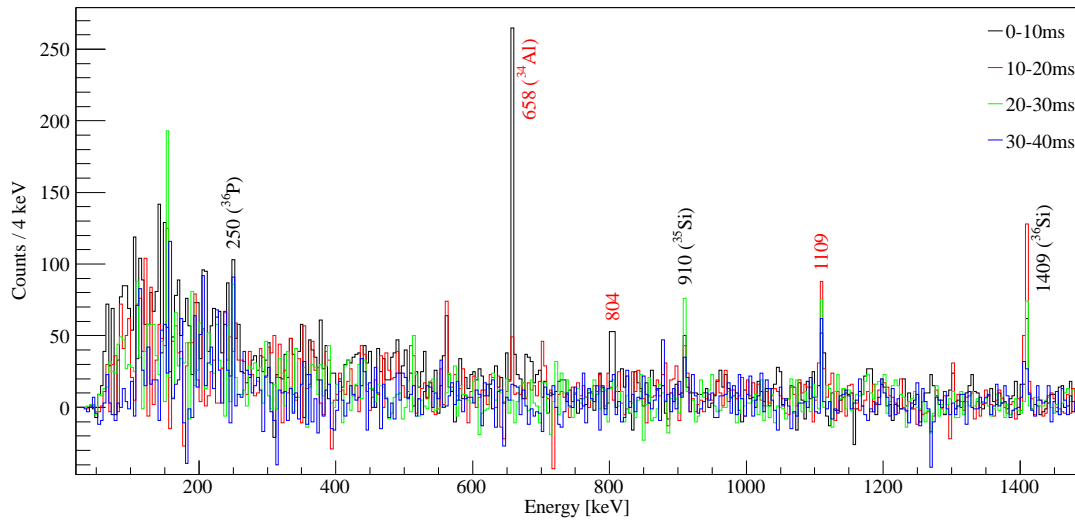

Figure 5.16: Background subtracted β-delayed γ-ray spectrum after the decay of ^{36}Mg. The black, red, green and blue spectra correspond to implantation-decay correlations time windows with a width of 10 ms (see legend).

can be made about the coincidences of the 1109 keV line due to the low statistics. For the probability of a β-delayed neutron emission of ^{36}Mg there is a preliminary result of $P_x(n) = \sum_{i=1}^{\infty} i \cdot P(in) = 48(12)\,\%$ [Yon99] which is a composition of the probabilities for β-delayed (multi-)neutron emission. It cannot be compared to the results of this work.

energy [keV]	intensity [%] this experiment	origin
658	100(10)	^{34}Al [Pri01, Him08]
804	42(9)	$^{34-36}$Al (this work)
910	21(11)*	^{35}Si [Num01]
1109	33(10)*	$^{34-36}$Si (this work)
1409	36(21)*	^{36}Si [Lia06]

Table 5.7: Relative intensities of β-delayed γ-rays after the decay of ^{36}Mg, normalized to the γ-ray at an energy of 657 keV and corrected for efficiency.
(*) The relative intensities are given in the time window of 0-10 ms after an implantation. As the 910, 1109 and 1409 keV lines do not originate from a daughter nucleus their relative intensities change in the later time windows.

5.5 Decay of ^{35}Na

The β-delayed γ-ray spectrum after the decay of ^{35}Na is shown in figure 5.17. In the background-subtracted spectrum there is only one γ-ray at the energy 661 keV. The time evolution of the γ-ray spectrum is shown in figure 5.18. The 661 keV line only appears in the first time window from 0 to 10 milliseconds after an implantation of ^{35}Na. Consequently it can be attributed to a transition in one of the daughter nuclei $^{33-35}$Mg after the ^{35}Na β decay as the half-life of the mother nuclide $t_{1/2}(^{35}$Na$) = 2.4(0.9)$ ms (this work) is much shorter than the 10 ms time window. The half-lives of the daughter nuclei $^{33-35}$Mg $t_{1/2}(^{33}$Mg$) = 90.5(1.6)$ ms [Eva12], $t_{1/2}(^{34}$Mg$) = 20(10)$ ms [Lan84] and $t_{1/2}(^{35}$Mg$) = 70(40)$ ms [Eva12] are longer than the 10 ms time window. So if the transition was in a granddaughter nucleus after the β decay there would not only be entries in the first time window after an implantation but also in the later time windows. The energy available for the β decay of ^{35}Na is $Q_\beta = 22.2(6)$ MeV and the one- and two-neutron separation energies of the daughter ^{35}Mg are $S_n = 0.75(18)$ MeV and $S_{2n} = 5.47(18)$ MeV, respectively [Wan12]. For the probability of a β-delayed neutron emission after the decay of ^{35}Na there is no experimental result available in literature. A calculation of [Möl97] gives the results $P(n) = 57\%$ and $P(2n) = 11\%$.

There are two possible nuclei to assign the 661 keV line:

1. It may originate from the deexcitation of the 2_1^+ state to the 0^+ ground state in the β-n daughter nucleus ^{34}Mg. The excitation energy of this state was reported in four papers to be 685(16) keV [Ele06], 659(14) keV [Chu05], 660(10) keV [Yon01] and 656(7) keV [Iwa01], respectively.

2. A transition in the β-daughter ^{35}Mg is reported to be at an energy of 670(8) keV [Gad11].

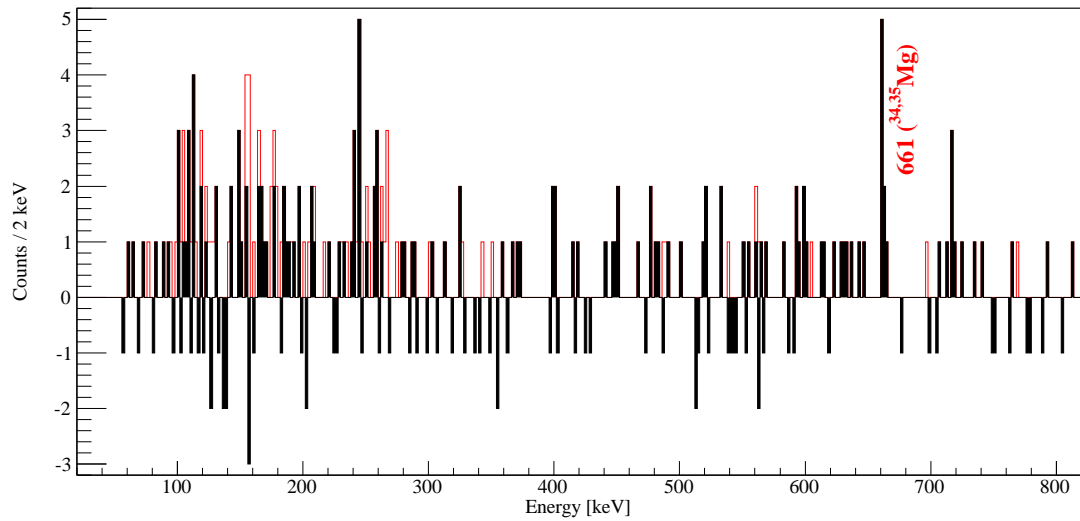With the present experimental data one cannot distinguish whether the 661 keV line is a transition in ^{34}Mg or ^{35}Mg.

Figure 5.17: β-delayed γ-ray spectrum after the decay of ^{35}Na. The black (red) spectrum corresponds to implantation-decay correlations with(out) background subtraction within 10 ms after an implantation.
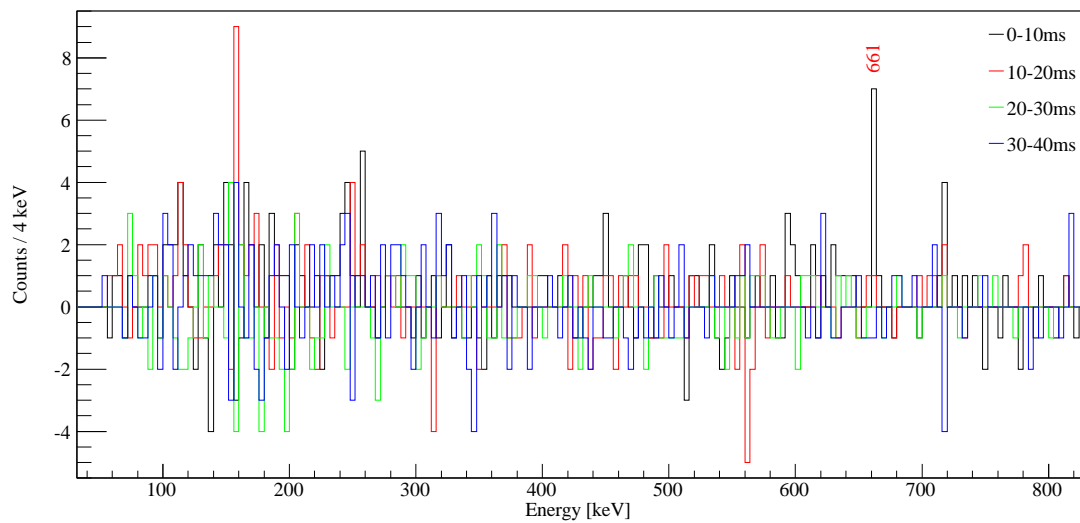

Figure 5.18: Background subtracted β-delayed γ-ray spectrum after the decay of ^{35}Na. The black, red, green and blue spectra correspond to implantation-decay correlations time windows with a width of 10 ms (see legend).

5.6 Decay of ^{29}F

The β-delayed γ-ray spectrum after the decay of ^{29}F is shown in figure 5.19. In the background-subtracted spectrum there are two lines at an energy of 1308 and 1590 keV. In addition the two lines at 444 and 1483 keV are background transitions in ^{30}Al and

^{30}Mg, respectively. They disappear in the background-subtracted spectrum as they are emitted by the granddaughter and great-granddaughter after the β decay of ^{30}Ne, which is the nuclide implanted with the largest intensity. The time evolution of the γ-ray spectrum is shown in figure 5.20. Both the 1308 and 1590 keV lines only appear in the
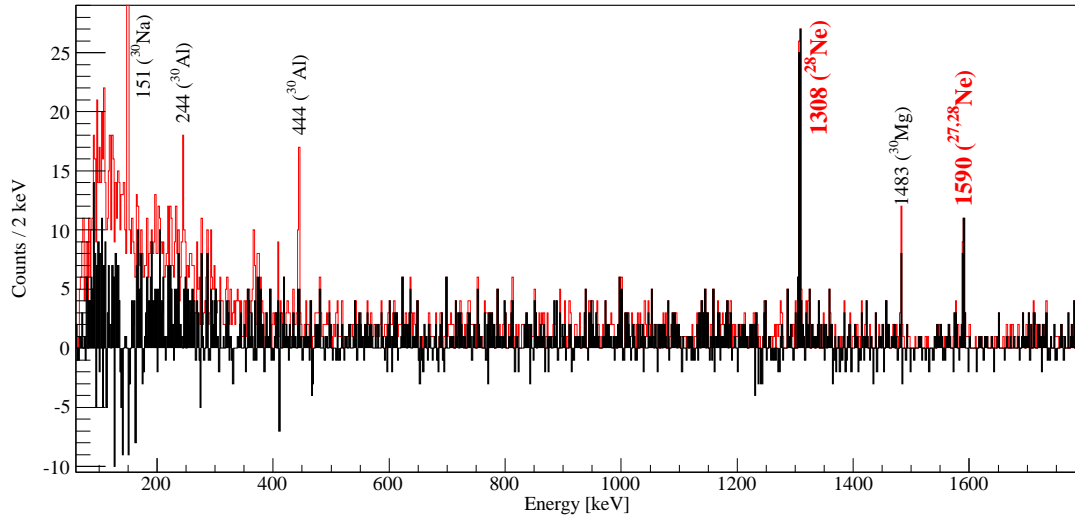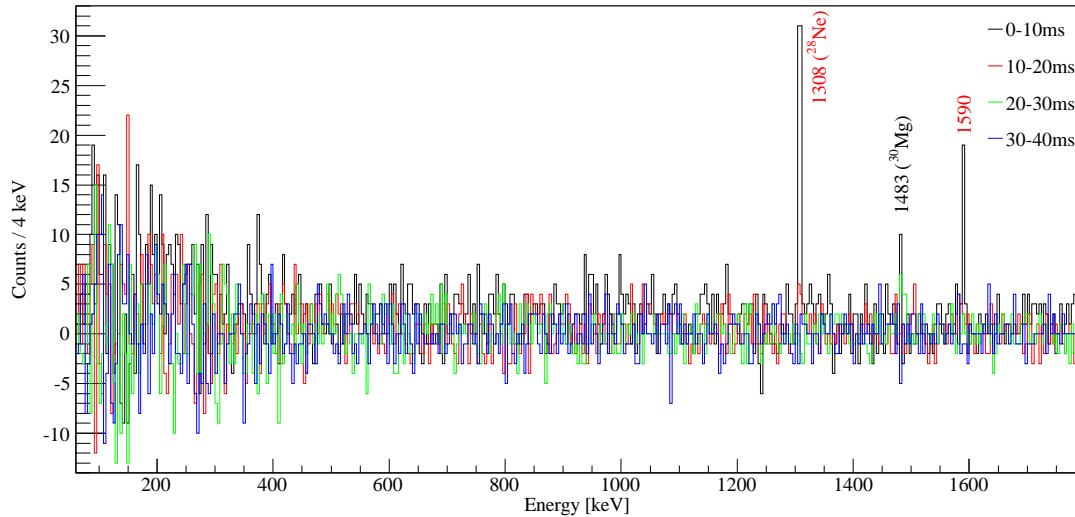

Figure 5.19: β-delayed γ-ray spectrum after the decay of ^{29}F. The black (red) spectrum corresponds to implantation-decay correlations with(out) background subtraction within 10 ms after an implantation.

Figure 5.20: Background subtracted β-delayed γ-ray spectrum after the decay of ^{29}F. The black, red, green and blue spectra correspond to implantation-decay correlations time windows with a width of 10 ms (see legend).

first time window from 0 to 10 milliseconds after an implantation of ^{29}F. Consequently they can be attributed to a transition in one of the daughter nuclei $^{27-29}$Ne after the ^{29}F β decay as the half-life of the mother nucleus $t_{1/2}(^{29}$F$) = 2.67(28)\,$ms (this work) is much shorter than the $10\,$ms time window and the half-lives of the daughter nuclei $^{27-29}$Ne $t_{1/2}(^{29}$Ne$) = 15.8(1.5)\,$ms [Tri06], $t_{1/2}(^{28}$Ne$) = 18.9(0.4)\,$ms [Eva12] and $t_{1/2}(^{27}$Ne$) = 31.5(1.3)\,$ms [Tri06] are longer than the $10\,$ms time window. So one can exclude that the 1308 and $1590\,$keV lines are transitions in a granddaughter nucleus $^{27-29}$Na after the decay.

The probability of a β-delayed neutron emission after the decay of ^{29}F is 100(80)% [Pen01]. The ground state spin and parity of ^{29}F is $5/2^+$ from systematics [Aud03]. The energy available for the β decay of ^{29}F is $Q_\beta = 21.2(5)\,$MeV and the one- and two-neutron separation energies of the daughter ^{29}Ne are $S_n = 0.96(14)\,$MeV and $S_{2n} = 4.78(12)\,$MeV, respectively [Wan12]. Since the one-neutron separation energy is smaller than the energy of the two lines, a placement in ^{29}Ne can be excluded as the β-delayed neutron decay is much faster than an electromagnetic deexcitation. No statement can be made about a possible coincidence of the 1308 and $1590\,$keV transitions as one expects less than one detected coincident event (see appendix section A.5) and no coincident event was detected.

The energy of the first 2_1^+ excited state in ^{28}Ne was measured to be $1320(20)\,$keV [Pri99], $1293(8)\,$keV [Bel05], $1319(22)\,$keV [Dom06] and $1306(4)\,$keV [RV07]. Consequently the $2_1^+ \rightarrow 0_{gs}^+$ transition in the β-n daughter ^{28}Ne is a candidate for the $1308\,$keV line. For the $1590\,$keV line no candidate transition can be found in the present literature. Table 5.8 gives a summary of the relative intensities and the origin of the measured transitions after the decay of ^{29}F.

energy [keV]	intensity [%] this experiment	origin
1308	100(13)	^{28}Ne
1590	44(9)	^{27,28}Ne

Table 5.8: Relative intensities of β-delayed γ-rays after the decay of ^{29}F, normalized to the γ-ray at an energy of $1308\,$keV and corrected for efficiency.

5.7 Modified shell model calculations for ^{37}Si and systematics for $^{35-38}$Si

The experimental excitation energies of the levels in ^{37}Si can give evidence for modifications of the SDPF-MU interaction. Negative and positive parity states are treated separately, as their modifications have different origins. To give a consistent description the level schemes of ^{37}Si are compared to the level schemes of ^{35,36,38}Si. This section summarizes the results of an extensive discussion with Yutaka Utsuno [Uts13].

5.7.1 Negative parity states of ^{37}Si

In figure 5.21 the experimental excitation energies of the negative parity states in ^{37}Si and ^{35}Si are compared to several calculations. The level schemes obtained in this experiment and [Num01] are labeled with (a) and the SDPF-MU calculations with (b).

If there are large $Z = 14$ and $N = 28$ shell gaps the $3/2_1^-$, $5/2_1^-$, and $7/2_1^-$ states in ^{37}Si have a pure $(\nu f7/2)^3$ configuration. With this assumption, the $3/2_1^-$, $5/2_1^-$, and $7/2_1^-$ energy levels in ^{37}Si can be obtained as

$$E(3/2_1^-) = 3 \cdot \left(\frac{3}{14} E_2 + \frac{11}{14} E_4 \right), \tag{5.3}$$

$$E(5/2_1^-) = 3 \cdot \left(\frac{11}{18} E_2 + \frac{2}{33} E_4 + \frac{65}{198} E_6 \right), \tag{5.4}$$

and

$$E(7/2_1^-) = 3 \cdot \left(\frac{1}{4} E_0 + \frac{5}{36} E_2 + \frac{1}{4} E_4 + \frac{13}{36} E_6 \right). \tag{5.5}$$

E_0, E_2, E_4, and E_6 are the energies of the 0_1^+, 2_1^+, 4_1^+ and 6_1^+ states of a $(\nu f7/2)^2$ system and the prefactors result from the coupling of the angular momenta. Using the experimental energy levels of ^{36}Si for $E_0 = 0\,\text{keV}$, $E_2 = 1408\,\text{keV}$ and $E_4 = 2850\,\text{keV}$ [Lia06] and the shell model for the 6_1^+ level ($E_6 = 3837\,\text{keV}$ [Uts13]), the energy levels of ^{37}Si become $E_{5/2_1^-} = 0\,\text{keV}$, $E_{7/2_1^-} = 3\,\text{keV}$ and $E_{3/2_1^-} = 745\,\text{keV}$ as it can be seen in the level scheme labeled with (d) in figure 5.21. The near degeneracy of the $5/2_1^-$ and
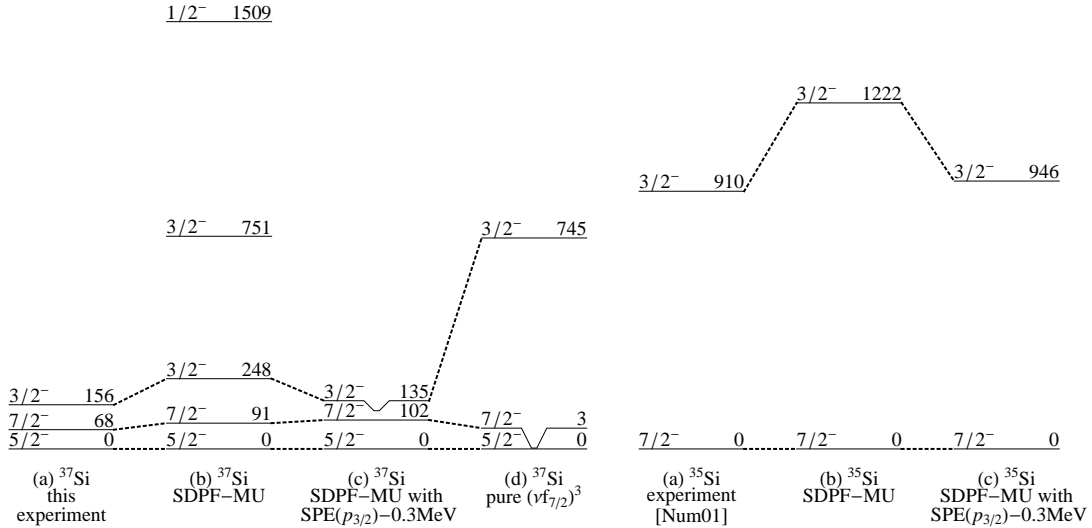

Figure 5.21: Comparison of experimental excitation energies for the negative parity states of ^{37}Si and ^{35}Si with several theoretical calculations. Detailed explanations can be found in the text.

$7/2_1^-$ states in the experiment is reproduced by this simple model, but the $3/2_1^-$ level has a very large excitation energy.

In contrast, if the $\nu p_{3/2}$ orbit is close to the $\nu f_{7/2}$ orbit, the $3/2_1^-$ level should have some mixing with the $(\nu f_{7/2})^2 \otimes (\nu p_{3/2})^1$ configuration. The mean occupation numbers in the $\nu p_{3/2}$ orbit calculated with the SDPF-MU interaction for the $5/2_1^-$, $7/2_1^-$ and $3/2_1^-$ states are $n_{\nu p_{3/2}}(5/2_1^-) = 0.214$, $n_{\nu p_{3/2}}(7/2_1^-) = 0.180$ and $n_{\nu p_{3/2}}(3/2_1^-) = 0.577$, respectively (see figure 5.22), showing more $\nu p_{3/2}$ contribution in the $3/2_1^-$ state than in the $5/2_1^-$ and $7/2_1^-$ states. The $3/2_1^-$ level is lowered by a strong mixing with the $(\nu f_{7/2})^2 \otimes (\nu p_{3/2})^1$ configuration. It is likely that the $3/2_1^-$ level is sensitive to the single-particle energy of the $\nu p3/2$ orbit. The $\nu p_{3/2}$ single-particle energy can be reduced to reproduce the $3/2^-$ level of ^{35}Si. The results of the calculations with the SDPF-MU interaction using a $\nu p_{3/2}$ SPE reduced by 0.3 MeV are displayed in the level schemes labeled with (c) in figure 5.21. The $3/2_1^-$ level of ^{37}Si is lowered with this calculation and the agreement with the experimental result gets better. From this comparison, it can be concluded that the $3/2_1^-$ level is strongly influenced by the $\nu p_{3/2}$ SPE and a consistent description of ^{35}Si and ^{37}Si can be obtained taking an appropriate $\nu p3/2$ SPE which is reduced by 0.3 MeV compared to the "standard" $\nu p3/2$ SPE.

The tensor force is an important part for the calculations. In a calculation with the SDPF-MU interaction whose cross-shell tensor force is removed the excitation energies of the $3/2_1^-$ levels in ^{37}Si and ^{35}Si are $E_{3/2_1^-}(^{37}\text{Si}) = 378$ keV and $E_{3/2_1^-}(^{35}\text{Si}) = 1887$ keV. Since the tensor force decreases the $\nu f_{7/2} - p_{3/2}$ gap at $Z = 14$ the excitation energies without the tensor force are too high.
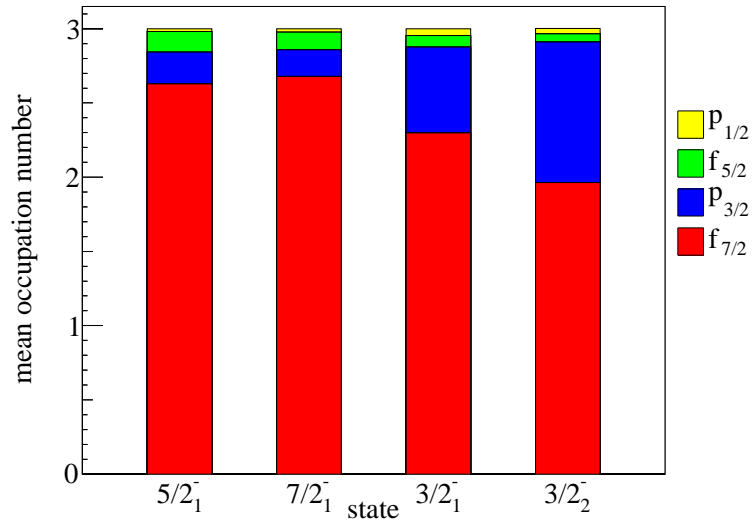

Figure 5.22: SDPF-MU calculation of the mean neutron occupation numbers for the ^{37}Si negative parity states in the $\nu f_{7/2}$, $\nu p_{3/2}$, $\nu f_{5/2}$ and $\nu p_{1/2}$ orbits.

5.7.2 Positive parity states of ^{37}Si

The positive parity states in ^{37}Si populated by the β decay are dominated by a ^{38}Si $(0^+_{gs}) \otimes (\nu d_{3/2})^{-1}$ and a ^{38}Si $(2^+_1) \otimes (\nu d_{3/2})^{-1}$ configuration. Shifting the $N = 20$ shell gap, the energies of the positive parity states are shifted in the same way. This means that the positive parity states are very sensitive to the $N = 20$ shell gap, while they are not a direct measure of the shell gap. The level energy is determined by a subtle balance between the $N = 20$ shell gap and the correlation energy. Namely, there is a $6 \sim 7 \, \text{MeV}$ $N = 20$ gap on top of a ^{34}Si core, but the lowest positive parity state is at an excitation energy below $\sim 1 \, \text{MeV}$ due to a large attractive correlation energy.

In the single particle picture the location of the one-neutron separation energy S_n is very sensitive to the absolute SPE of the $\nu f_{7/2}$ orbit. The SDPF-MU calculation results in $S_n(^{37}\text{Si}) = 2.61 \, \text{MeV}$ comparable to the experimental literature value of $S_n(^{37}\text{Si}) = 2.27(11) \, \text{MeV}$ [Wan12]. It is likely that a reasonable agreement of the $3/2^+_1$ level indicates both a good shell structure and a good correlation energy to the extent of hundreds of keV. On the other hand, the energy difference between the $3/2^+_1$ and $5/2^+_1$ states in ^{37}Si is independent of the $N = 20$ shell gap as the former is dominated by a ^{38}Si $(0^+_{gs}) \otimes (\nu d_{3/2})^{-1}$ and the latter by a ^{38}Si $(2^+_1) \otimes (\nu d_{3/2})^{-1}$ configuration. Their energy difference with the SDPF-MU interaction is $\Delta E_{\text{SDPF-MU}}(3/2^+_1, 5/2^+_1) = 1.033 \, \text{MeV}$, somewhat larger than the experimental value of $\Delta E_{\text{exp}}(3/2^+_1, 5/2^+_1) = 0.553 \, \text{MeV}$. As mentioned previously, one possibility is the effect of the 2^+_1 level in ^{38}Si. The 2^+_1 level energy in ^{38}Si with the SDPF-MU interaction is $E_{\text{SDPF-MU}}(2^+_1) = 1.260 \, \text{MeV}$, while it is $E_{\text{exp}}(2^+_1) = 1.074 \, \text{MeV}$ experimentally. When the pairing matrix element in the $\nu f_{7/2}$ orbit is weakened by 15% to get a good 2^+_1 energy in ^{38}Si (1.099 MeV), the energy difference between the $3/2^+_1$ and $5/2^+_1$ states in ^{37}Si becomes 0.899 MeV. This is an improvement compared to the original SDPF-MU, but there is still a discrepancy of $\sim 0.3 \, \text{MeV}$ with $\Delta E_{\text{exp}}(3/2^+_1, 5/2^+_1)$. A summary of the energy differences between the $3/2^+_1$ and $5/2^+_1$ states in the odd-mass isotopes ^{35,37}Si and the 0^+_1 and 2^+_1 states in the even-mass isotopes ^{36,38}Si is shown in table 5.9. As measured in a β decay experiment [Num01] the energy difference of the $3/2^+_1$ and $5/2^+_1$ states in ^{35}Si is $\Delta E_{\text{exp}}(3/2^+_1, 5/2^+_1) = 1.194 \, \text{MeV}$. But it is $\Delta E_{\text{SDPF-MU}}(3/2^+_1, 5/2^+_1) = 1.763 \, \text{MeV}$ with the SDPF-MU interaction and 1603 keV with the modified SDPF-MU interaction. The overestimation of $\Delta E(3/2^+_1, 5/2^+_1)$ in ^{35}Si by the SDPF-MU calculation gets reduced from $\sim 0.6 \, \text{MeV}$ to $\sim 0.4 \, \text{MeV}$ by the modified matrix element similar to the case of ^{37}Si. There might be a common reason for the deviations. But at present these deviations are not understood. The experimental excitation energy of the 2^+_1 state in ^{36}Si is reproduced by the modified SDPF-MU interaction.

	experiment	SDPF-MU	modified SDPF-MU
^{35}Si: $\Delta E(3/2_1^+, 5/2_1^+)$	1194 keV	1763 keV	1603 keV
^{37}Si: $\Delta E(3/2_1^+, 5/2_1^+)$	553 keV	1033 keV	899keV
^{36}Si: $\Delta E(0_1^+, 2_1^+)$	1408 keV	1609 keV	1420 keV
^{38}Si: $\Delta E(0_1^+, 2_1^+)$	1074 keV	1260 keV	1099keV

Table 5.9: Summary of the energy differences between the $3/2_1^+$ and $5/2_1^+$ states in the odd-mass and the 0_1^+ and 2_1^+ states in the even-mass Si isotopes. The experimental results are compared to the SDPF-MU calculation and a modified version of the SDPF-MU calculation. The pairing matrix element in the $\nu f_{7/2}$ orbit is weakened by 15% in this modified calculation.

Chapter 6

Summary and Outlook

In this thesis the properties of neutron-rich nuclei around ^{37}Al were investigated by performing decay spectroscopy. The data analyzed in this thesis were recorded at a beam time in fall 2010 at the RIKEN Nishina Center for Accelerator-Based Science. The fragments of a cocktail beam which was produced by relativistic projectile fragmentation of a ^{48}Ca primary beam were identified and implanted in the CAITEN detector. With this implantation- and β-detector together with germanium clover detectors decay properties of the nuclei of interest could be deduced. Here is a short summary of the obtained results:

6.1 Half-life measurements

- The half-lives of ^{29}F, ^{30}Ne, ^{35,36}Mg and ^{37}Al were measured with a better precision than the known values. For ^{31,35}Na and ^{38}Al literature half-life values could be confirmed within a confidence level of 2σ. The results can be found in the tables 4.1 and 4.2.

6.2 Gamma-ray spectroscopy

- By measuring β-delayed γ-rays after the decay of ^{30}Ne the level structure of ^{30}Na reported in [Tri07a] could be reproduced. With the measured γ-rays at the energies of 151, 367, 410, 1598, 1963 and 2113 keV and the information from γ-γ coincidences a level scheme with excited states at 151, 517, 926 and 2113 keV can be confirmed.

- For the first time β-delayed γ-rays were measured after the decay of ^{37}Al. Transitions with 156, 562, 717, 1115, 1202, 1270 and 1504 keV were measured and coincidences of the transition at 156 keV with the lines at 562 and 1115 keV were observed. With this information and guided by shell model calculations a level scheme of ^{37}Si could be constructed with excited states at 68, 156, 717 and 1270 keV. From the determined log(ft) values and a comparison to shell model calculations tentative spin and parity assignments displayed in table 6.1 could be made. The positive parity states are populated in allowed β decays from the

experimental energy [keV]	0	68	156	717	1270
SDPF-MU energy [keV]	0	91	245	586	1619
SDPF-U energy [keV]	0	170	237		
J^P	$5/2^-$	$7/2^-$	$3/2^-$	$3/2^+$	$5/2^+$

Table 6.1: Tentative spin and parity assignment for the states in ^{37}Si.

$5/2^+$ ground state of ^{37}Al and have a 1-hole configuration with respect to the ground state $(0^+_{\text{gs}}) \otimes (\nu d_{3/2})^{-1}$ and first excited state $(2^+_1) \otimes (\nu d_{3/2})^{-1}$ of ^{38}Si. Both the SDPF-MU and the SDPF-U shell model calculations reproduce the relative energies between the $5/2^-_1$, $7/2^-_1$ and $3/2^-_1$ negative parity states very well (deviations are smaller than 0.1 MeV). A calculation of the positive parity states is only possible with the SDPF-MU interaction since for the SDPF-U interaction a $N = 20$ closed core is used and no 1p-1h excitations across this core are allowed. The excitation energies of the $3/2^+_1$ and $5/2^+_1$ states calculated with the SDPF-MU interaction are smaller by 0.13 MeV and larger by 0.35 MeV, respectively, with respect to the experimental results. A systematic comparison between the experimental and calculated level schemes of ^{35}Si [Num01] and ^{38}Si suggest a modification of the following input parameters for the SDPF-MU calculation [Uts13] (for details see section 5.7): The single particle energy (SPE) of the $\nu p_{3/2}$ orbit should be decreased by 0.3 MeV and the pairing matrix element of the $\nu f_{7/2}$ orbit by 15% to better reproduce the experimental results.

- After the decay of ^{38}Al γ-transitions with the energies 68, 418, 1074, 1159, 1470, 2211 and 3656 keV were measured for the first time. A comparison to [Tak12] leads to the assignment of the 1074 keV line to the $2^+_1 \to 0^+_{\text{gs}}$ transition and the 1159 keV line to the $4^+_1 \to 2^+_1$ transition in ^{38}Si. Thus an improvement of the precision of excitation energies $E_{2^+_1}$ and $E_{4^+_1}$ is achieved. Coincidences of the 1074 keV line with transitions at 418, 1159, 1470 and 2211 keV show that these lines originate from ^{38}Si. An experimental level scheme for ^{38}Si including these transitions is shown in figure 5.14 of section 5.3.2. By comparing the results to shell model calculations tentative spin and parity assignments for all excited states in ^{38}Si are possible.

- After the decay of ^{36}Mg γ-rays with energies of 658, 804 and 1109 keV were detected. From the timing information the 658 and 804 keV lines could be attributed to transitions in one of the daughter nuclei $^{34-36}$Al while the 1109 keV line is a transition in a granddaughter $^{34-36}$Si. As a 657 ± 9 keV ground state transition was already measured in ^{34}Al [Him08] it is very likely that it corresponds to the 658 keV transition measured in this work.

- A 661 keV line was measured after the decay of ^{35}Na. From the timing information and a comparison to previous measurements [Ele06, Chu05, Yon01, Iwa01, Gad11] it could be assigned to a transition in ^{34}Mg or ^{35}Mg.

- γ-rays with the energies 1308 and 1590 keV were detected after the ^{29}F β decay. From the timing they could both be assigned to transitions in one of the daughter nuclei $^{27-29}$Ne. Comparing to previous measurements [Pri99, Bel05, Dom06, RV07] the 1308 keV line is likely to originate from the $2^+_1 \rightarrow 0^+_{gs}$ transition in ^{28}Ne. For the 1590 keV line no candidate transition is known. The one-neutron separation energy of ^{29}Ne is smaller than 1590 keV. Consequently a placement of the 1590 keV line in ^{29}Ne can be excluded.

6.3 Upgrade of the CAITEN array

To improve the performance of the CAITEN detector several updates are planned in the future: To increase the geometrical acceptance the layout of the ring with the photomultipliers will be changed. Instead of one row with 24 photomultipliers there will be two rows with 12 photomultipliers. In addition the gaps among the photomultipliers will be decreased to improve the detection efficiency. Furthermore an additional trigger line will be prepared with lower threshold values (with a multiplicity condition of 2 or more different channels above threshold) to save the decay events at the gaps of the photomultipliers.

Appendix

A.1 General Probability Terms

λ_1, λ_{20}, λ_{21}, λ_{22}, λ_{30}, λ_{31} and λ_{32} denote the decay constants for the mother, daughter, β-n daughter, β-2n daughter, granddaughter, β-n granddaughter and β-2n granddaughter decay. Higher numbers of neutron emission and further decay generations are neglected. This is reasonable because further generations have very long life times compared to the mother nuclides and there is only a small probability to have more than two neutrons emitted in one decay chain.

$p_{x,N}$ denotes the probability that a nuclide x emits N neutrons at the beta decay (e.g. $p_{1,0}$, $p_{1,1}$, $p_{1,2}$, $p_{20,0}$, $p_{20,1}$, $p_{20,2}$, $p_{21,0}$, $p_{21,1}$ and $p_{22,0}$).

$P_x(t)$ is the probability that a nuclide x exists at the time t since the implantation of the mother nuclide.

$$\frac{\partial P_1\left(\lambda_1, t\right)}{\partial t} = -\lambda_1 P_1\left(\lambda_1, t\right) \text{ with } P_1(t=0) = 1 \tag{A.1}$$

$$P_1\left(\lambda_1, t\right) = \exp\left(-\lambda_1 t\right) \tag{A.2}$$

The probability density of a decay of a nuclide x with the decay constant λ_x taking place in the infinitesimal interval between t and t + dt is given by $f_x(t)$.

$$f_x\left(\lambda_x, t\right) = \lambda_x P_x\left(\lambda_x, t\right) \tag{A.3}$$

$$f_1\left(\lambda_1, t\right) = \lambda_1 P_1\left(\lambda_1, t\right) = \lambda_1 \cdot \exp\left(-\lambda_1 t\right) \tag{A.4}$$

The probability of a decay of a nuclide x taking place in the interval between t = 0 and t is given by the expression $F_x(t)$.

$$F_x\left(\lambda_x, t\right) = \int_0^t f_x\left(\lambda_x, t'\right)\, dt' \tag{A.5}$$

$$F_1\left(\lambda_1, t\right) = \int_0^t f_1\left(\lambda_1, t'\right)\, dt' = 1 - \exp\left(-\lambda_1 t\right) \tag{A.6}$$

The following formulae show the values $N_x(t)$, $f_x(t)$ and $F_x(t)$ for the daughter and granddaughter nuclides.

$$\frac{\partial P_{20}\left(p_{1,0}, \lambda_1, \lambda_{20}, t\right)}{\partial t} = p_{1,0}\lambda_1 P_1\left(\lambda_1, t\right) - \lambda_{20}P_{20}\left(p_{1,0}, \lambda_1, \lambda_{20}, t\right) \text{ with } P_{20}(t=0) = 0$$
(A.7)

$$P_{20}\left(p_{1,0}, \lambda_1, \lambda_{20}, t\right) = \frac{p_{1,0}\lambda_1}{\lambda_{20} - \lambda_1}\left[\exp\left(-\lambda_1 t\right) - \exp\left(-\lambda_{20}t\right)\right]$$
(A.8)

$$f_{20}\left(p_{1,0}, \lambda_1, \lambda_{20}, t\right) = \lambda_{20}P_{20}\left(p_{1,0}, \lambda_1, \lambda_{20}, t\right) = \frac{p_{1,0}\lambda_1\lambda_{20}}{\lambda_{20} - \lambda_1}\left[\exp\left(-\lambda_1 t\right) - \exp\left(-\lambda_{20}t\right)\right]$$
(A.9)

$$F_{20}\left(p_{1,0}, \lambda_1, \lambda_{20}, t\right) = p_{1,0}\left[1 - \frac{\lambda_1\lambda_{20}}{\lambda_{20} - \lambda_1}\left(\frac{1}{\lambda_1}\exp\left(-\lambda_1 t\right) - \frac{1}{\lambda_{20}}\exp\left(-\lambda_{20}t\right)\right)\right]$$
(A.10)

$$\frac{\partial P_{21}\left(p_{1,1}, \lambda_1, \lambda_{21}, t\right)}{\partial t} = p_{1,1}\lambda_1 P_1\left(\lambda_1, t\right) - \lambda_{21}P_{21}\left(p_{1,1}, \lambda_1, \lambda_{21}, t\right) \text{ with } P_{21}(t=0) = 0$$
(A.11)

$$P_{21}\left(p_{1,1}, \lambda_1, \lambda_{21}, t\right) = \frac{p_{1,1}\lambda_1}{\lambda_{21} - \lambda_1}\left[\exp\left(-\lambda_1 t\right) - \exp\left(-\lambda_{21}t\right)\right]$$
(A.12)

$$f_{21}\left(p_{1,1}, \lambda_1, \lambda_{21}, t\right) = \frac{p_{1,1}\lambda_1\lambda_{21}}{\lambda_{21} - \lambda_1}\left[\exp\left(-\lambda_1 t\right) - \exp\left(-\lambda_{21}t\right)\right]$$
(A.13)

$$F_{21}\left(p_{1,1}, \lambda_1, \lambda_{21}, t\right) = p_{1,1}\left[1 - \frac{\lambda_1\lambda_{21}}{\lambda_{21} - \lambda_1}\left(\frac{1}{\lambda_1}\exp\left(-\lambda_1 t\right) - \frac{1}{\lambda_{21}}\exp\left(-\lambda_{21}t\right)\right)\right]$$
(A.14)

$$\frac{\partial P_{22}\left(p_{1,2}, \lambda_1, \lambda_{22}, t\right)}{\partial t} = p_{1,2}\lambda_1 P_1\left(\lambda_1, t\right) - \lambda_{22}P_{22}\left(p_{1,2}, \lambda_1, \lambda_{22}, t\right) \text{ with } P_{22}(t=0) = 0$$
(A.15)

$$P_{22}\left(p_{1,2}, \lambda_1, \lambda_{22}, t\right) = \frac{p_{1,2}\lambda_1}{\lambda_{22} - \lambda_1}\left[\exp\left(-\lambda_1 t\right) - \exp\left(-\lambda_{22}t\right)\right]$$
(A.16)

$$f_{22}\left(p_{1,2}, \lambda_1, \lambda_{22}, t\right) = \frac{p_{1,2}\lambda_1\lambda_{22}}{\lambda_{22} - \lambda_1}\left[\exp\left(-\lambda_1 t\right) - \exp\left(-\lambda_{22}t\right)\right]$$
(A.17)

$$F_{22}\left(p_{1,2}, \lambda_1, \lambda_{22}, t\right) = p_{1,2}\left[1 - \frac{\lambda_1\lambda_{22}}{\lambda_{22} - \lambda_1}\left(\frac{1}{\lambda_1}\exp\left(-\lambda_1 t\right) - \frac{1}{\lambda_{22}}\exp\left(-\lambda_{22}t\right)\right)\right]$$
(A.18)

$$\frac{\partial P_{30}\left(p_{1,0}, p_{20,0}, \lambda_1, \lambda_{20}, \lambda_{30}, t\right)}{\partial t} = p_{20,0}\lambda_{20}P_{20}\left(p_{1,0}, \lambda_1, \lambda_{20}, t\right)_{\text{with } P_{30}(t=0)=0}$$
$$- \lambda_{30}P_{30}\left(p_{1,0}, p_{20,0}, \lambda_1, \lambda_{20}, \lambda_{30}, t\right)$$

$$(A.19)$$

$$P_{30}\left(p_{1,0}, p_{20,0}, \lambda_1, \lambda_{20}, \lambda_{30}, t\right) =$$
$$\frac{p_{1,0}p_{20,0}\lambda_1\lambda_{20}}{\left(\lambda_{20}-\lambda_1\right)\left(\lambda_{30}-\lambda_1\right)\left(\lambda_{30}-\lambda_{20}\right)}\left[\left(\lambda_{30}-\lambda_{20}\right)\exp\left(-\lambda_1 t\right)\right. \qquad (A.20)$$
$$\left. - \left(\lambda_{30}-\lambda_1\right)\exp\left(-\lambda_{20}t\right) + \left(\lambda_{20}-\lambda_1\right)\exp\left(-\lambda_{30}t\right)\right]$$

$$f_{30}\left(p_{1,0}, p_{20,0}, \lambda_1, \lambda_{20}, \lambda_{30}, t\right) =$$
$$\frac{p_{1,0}p_{20,0}\lambda_1\lambda_{20}\lambda_{30}}{\left(\lambda_{20}-\lambda_1\right)\left(\lambda_{30}-\lambda_1\right)\left(\lambda_{30}-\lambda_{20}\right)}\left[\left(\lambda_{30}-\lambda_{20}\right)\exp\left(-\lambda_1 t\right)\right. \qquad (A.21)$$
$$\left. - \left(\lambda_{30}-\lambda_1\right)\exp\left(-\lambda_{20}t\right) + \left(\lambda_{20}-\lambda_1\right)\exp\left(-\lambda_{30}t\right)\right]$$

$$F_{30}\left(p_{1,0}, p_{20,0}, \lambda_1, \lambda_{20}, \lambda_{30}, t\right) =$$
$$p_{1,0}, p_{20,0} - \frac{p_{1,0}p_{20,0}\lambda_1\lambda_{20}\lambda_{30}}{\left(\lambda_{20}-\lambda_1\right)\left(\lambda_{30}-\lambda_1\right)\left(\lambda_{30}-\lambda_{20}\right)}\left[\frac{\lambda_{30}-\lambda_{20}}{\lambda_1}\exp\left(-\lambda_1 t\right)\right. \qquad (A.22)$$
$$\left. - \frac{\lambda_{30}-\lambda_1}{\lambda_{20}}\exp\left(-\lambda_{20}t\right) + \frac{\lambda_{20}-\lambda_1}{\lambda_{30}}\exp\left(-\lambda_{30}t\right)\right]$$

$$P_{31}\left(p_{1,0}, p_{1,1}, p_{20,1}, p_{21,0}, \lambda_1, \lambda_{20}, \lambda_{21}, \lambda_{31}, t\right) =$$
$$= \lambda_1\left[\left(\frac{\lambda_{20}p_{1,0}p_{20,1}}{\lambda_{20}-\lambda_1} + \frac{\lambda_{21}p_{1,1}p_{21,0}}{\lambda_{21}-\lambda_1}\right)\frac{\exp\left(-\lambda_1 t\right)}{\lambda_{31}-\lambda_1} - \frac{\lambda_{20}p_{1,0}p_{20,1}\exp\left(-\lambda_{20}t\right)}{\left(\lambda_{31}-\lambda_{20}\right)\left(\lambda_{20}-\lambda_1\right)}\right.$$
$$\left. - \frac{\lambda_{21}p_{1,1}p_{21,0}\exp\left(-\lambda_{21}t\right)}{\left(\lambda_{31}-\lambda_{21}\right)\left(\lambda_{21}-\lambda_1\right)} + \left(\frac{\lambda_{20}p_{1,0}p_{20,1}}{\lambda_{31}-\lambda_{20}} + \frac{\lambda_{21}p_{1,1}p_{21,0}}{\lambda_{31}-\lambda_{21}}\right)\frac{\exp\left(-\lambda_{31}t\right)}{\lambda_{31}-\lambda_1}\right]$$
$$(A.23)$$

$$f_{31}\left(p_{1,0}, p_{1,1}, p_{20,1}, p_{21,0}, \lambda_1, \lambda_{20}, \lambda_{21}, \lambda_{31}, t\right) =$$
$$= \lambda_1\lambda_{31}\left[\left(\frac{\lambda_{20}p_{1,0}p_{20,1}}{\lambda_{20}-\lambda_1} + \frac{\lambda_{21}p_{1,1}p_{21,0}}{\lambda_{21}-\lambda_1}\right)\frac{\exp\left(-\lambda_1 t\right)}{\lambda_{31}-\lambda_1} - \frac{\lambda_{20}p_{1,0}p_{20,1}\exp\left(-\lambda_{20}t\right)}{\left(\lambda_{31}-\lambda_{20}\right)\left(\lambda_{20}-\lambda_1\right)}\right.$$
$$\left. - \frac{\lambda_{21}p_{1,1}p_{21,0}\exp\left(-\lambda_{21}t\right)}{\left(\lambda_{31}-\lambda_{21}\right)\left(\lambda_{21}-\lambda_1\right)} + \left(\frac{\lambda_{20}p_{1,0}p_{20,1}}{\lambda_{31}-\lambda_{20}} + \frac{\lambda_{21}p_{1,1}p_{21,0}}{\lambda_{31}-\lambda_{21}}\right)\frac{\exp\left(-\lambda_{31}t\right)}{\lambda_{31}-\lambda_1}\right]$$
$$(A.24)$$

$$F_{31}\left(p_{1,0}, p_{1,1}, p_{20,1}, p_{21,0}, \lambda_1, \lambda_{20}, \lambda_{21}, \lambda_{31}, t\right) =$$
$$= p_{1,0}p_{20,1} + p_{1,1}p_{21,0} - \lambda_1\lambda_{31}\left[\left(\frac{\lambda_{20}p_{1,0}p_{20,1}}{\lambda_{20} - \lambda_1} + \frac{\lambda_{21}p_{1,1}p_{21,0}}{\lambda_{21} - \lambda_1}\right)\frac{\exp\left(-\lambda_1 t\right)}{\lambda_1(\lambda_{31} - \lambda_1)}\right.$$
$$- \frac{p_{1,0}p_{20,1}\exp\left(-\lambda_{20}t\right)}{\left(\lambda_{31} - \lambda_{20}\right)\left(\lambda_{20} - \lambda_1\right)} - \frac{p_{1,1}p_{21,0}\exp\left(-\lambda_{21}t\right)}{\left(\lambda_{31} - \lambda_{21}\right)\left(\lambda_{21} - \lambda_1\right)}$$
$$\left.+ \left(\frac{\lambda_{20}p_{1,0}p_{20,1}}{\lambda_{31} - \lambda_{20}} + \frac{\lambda_{21}p_{1,1}p_{21,0}}{\lambda_{31} - \lambda_{21}}\right)\frac{\exp\left(-\lambda_{31}t\right)}{\lambda_{31}(\lambda_{31} - \lambda_1)}\right]$$

$$\text{(A.25)}$$

$$P_{32}\left(p_{1,0}, p_{1,1}, p_{1,2}, p_{20,2}, p_{21,1}, p_{22,0}, \lambda_1, \lambda_{20}, \lambda_{21}, \lambda_{22}, \lambda_{32}, t\right) =$$
$$= \lambda_1\left[\left(\frac{\lambda_{20}p_{1,0}p_{20,2}}{\lambda_{20} - \lambda_1} + \frac{\lambda_{21}p_{1,1}p_{21,1}}{\lambda_{21} - \lambda_1} + \frac{\lambda_{22}p_{1,2}p_{22,0}}{\lambda_{22} - \lambda_1}\right)\frac{\exp\left(-\lambda_1 t\right)}{\lambda_{32} - \lambda_1}\right.$$
$$- \frac{\lambda_{20}p_{1,0}p_{20,2}\exp\left(-\lambda_{20}t\right)}{\left(\lambda_{32} - \lambda_{20}\right)\left(\lambda_{20} - \lambda_1\right)} - \frac{\lambda_{21}p_{1,1}p_{21,1}\exp\left(-\lambda_{21}t\right)}{\left(\lambda_{32} - \lambda_{21}\right)\left(\lambda_{21} - \lambda_1\right)} - \frac{\lambda_{22}p_{1,2}p_{22,0}\exp\left(-\lambda_{22}t\right)}{\left(\lambda_{32} - \lambda_{22}\right)\left(\lambda_{22} - \lambda_1\right)}$$
$$\left.+ \left(\frac{\lambda_{20}p_{1,0}p_{20,2}}{\lambda_{32} - \lambda_{20}} + \frac{\lambda_{21}p_{1,1}p_{21,1}}{\lambda_{32} - \lambda_{21}} + \frac{\lambda_{22}p_{1,2}p_{22,0}}{\lambda_{32} - \lambda_{21}}\right)\frac{\exp\left(-\lambda_{32}t\right)}{\lambda_{32} - \lambda_1}\right]$$

$$\text{(A.26)}$$

$$f_{32}\left(p_{1,0}, p_{1,1}, p_{1,2}, p_{20,2}, p_{21,1}, p_{22,0}, \lambda_1, \lambda_{20}, \lambda_{21}, \lambda_{22}, \lambda_{32}, t\right) =$$
$$= \lambda_1\lambda_{32}\left[\left(\frac{\lambda_{20}p_{1,0}p_{20,2}}{\lambda_{20} - \lambda_1} + \frac{\lambda_{21}p_{1,1}p_{21,1}}{\lambda_{21} - \lambda_1} + \frac{\lambda_{22}p_{1,2}p_{22,0}}{\lambda_{22} - \lambda_1}\right)\frac{\exp\left(-\lambda_1 t\right)}{\lambda_{32} - \lambda_1}\right.$$
$$- \frac{\lambda_{20}p_{1,0}p_{20,2}\exp\left(-\lambda_{20}t\right)}{\left(\lambda_{32} - \lambda_{20}\right)\left(\lambda_{20} - \lambda_1\right)} - \frac{\lambda_{21}p_{1,1}p_{21,1}\exp\left(-\lambda_{21}t\right)}{\left(\lambda_{32} - \lambda_{21}\right)\left(\lambda_{21} - \lambda_1\right)} - \frac{\lambda_{22}p_{1,2}p_{22,0}\exp\left(-\lambda_{22}t\right)}{\left(\lambda_{32} - \lambda_{22}\right)\left(\lambda_{22} - \lambda_1\right)}$$
$$\left.+ \left(\frac{\lambda_{20}p_{1,0}p_{20,2}}{\lambda_{32} - \lambda_{20}} + \frac{\lambda_{21}p_{1,1}p_{21,1}}{\lambda_{32} - \lambda_{21}} + \frac{\lambda_{22}p_{1,2}p_{22,0}}{\lambda_{32} - \lambda_{21}}\right)\frac{\exp\left(-\lambda_{32}t\right)}{\lambda_{32} - \lambda_1}\right]$$

$$\text{(A.27)}$$

$$F_{32}\left(p_{1,0}, p_{1,1}, p_{1,2}, p_{20,2}, p_{21,1}, p_{22,0}, \lambda_1, \lambda_{20}, \lambda_{21}, \lambda_{22}, \lambda_{32}, t\right) =$$
$$= p_{1,0}p_{20,2} + p_{1,1}p_{21,1} + p_{1,2}p_{22,0}$$
$$- \lambda_1\lambda_{32}\left[\left(\frac{\lambda_{20}p_{1,0}p_{20,2}}{\lambda_{20} - \lambda_1} + \frac{\lambda_{21}p_{1,1}p_{21,1}}{\lambda_{21} - \lambda_1} + \frac{\lambda_{22}p_{1,2}p_{22,0}}{\lambda_{22} - \lambda_1}\right)\frac{\exp\left(-\lambda_1 t\right)}{\lambda_1(\lambda_{32} - \lambda_1)}\right.$$
$$- \frac{p_{1,0}p_{20,2}\exp\left(-\lambda_{20}t\right)}{\left(\lambda_{32} - \lambda_{20}\right)\left(\lambda_{20} - \lambda_1\right)} - \frac{p_{1,1}p_{21,1}\exp\left(-\lambda_{21}t\right)}{\left(\lambda_{32} - \lambda_{21}\right)\left(\lambda_{21} - \lambda_1\right)} - \frac{p_{1,2}p_{22,0}\exp\left(-\lambda_{22}t\right)}{\left(\lambda_{32} - \lambda_{22}\right)\left(\lambda_{22} - \lambda_1\right)}$$
$$\left.+ \left(\frac{\lambda_{20}p_{1,0}p_{20,2}}{\lambda_{32} - \lambda_{20}} + \frac{\lambda_{21}p_{1,1}p_{21,1}}{\lambda_{32} - \lambda_{21}} + \frac{\lambda_{22}p_{1,2}p_{22,0}}{\lambda_{32} - \lambda_{21}}\right)\frac{\exp\left(-\lambda_{32}t\right)}{\lambda_{32}(\lambda_{32} - \lambda_1)}\right]$$

$$\text{(A.28)}$$

A.2 Gamma-ray efficiency for small energies

The results of a GEANT4 simulation of the relative γ-ray efficiency for energies up to $E_\gamma = 500\,\text{keV}$ assuming that the germanium crystals have a dead layer[1] with a thickness of $l_{\text{dead}} = 0.0$, 0.5 or $1.0\,\text{mm}$ are shown in figure A.1. For energies $E_\gamma \gtrsim 0.15\,\text{MeV}$ the relative efficiencies do not depend on the thickness of the dead layer of the germanium crystals used in the simulation. However for energies $E_\gamma \lesssim 0.1\,\text{MeV}$ this parameter is very important. As this thickness is not known exactly the relative intensities for γ-rays with energies $E_\gamma \lesssim 0.1\,\text{MeV}$ cannot be determined accurately in this experiment. Figure 3.5 in section 3.2.2 shows the relative γ-ray efficiencies for energies from $E_\gamma = 150$ to $2500\,\text{keV}$. A dead layer thickness of $l_{\text{dead}} = 0\,\text{mm}$ is used to determine the

---

[1]dead layer of a semiconductor detector: The surface of the crystal is not completely depleted. Charge which is deposited there is not detected.
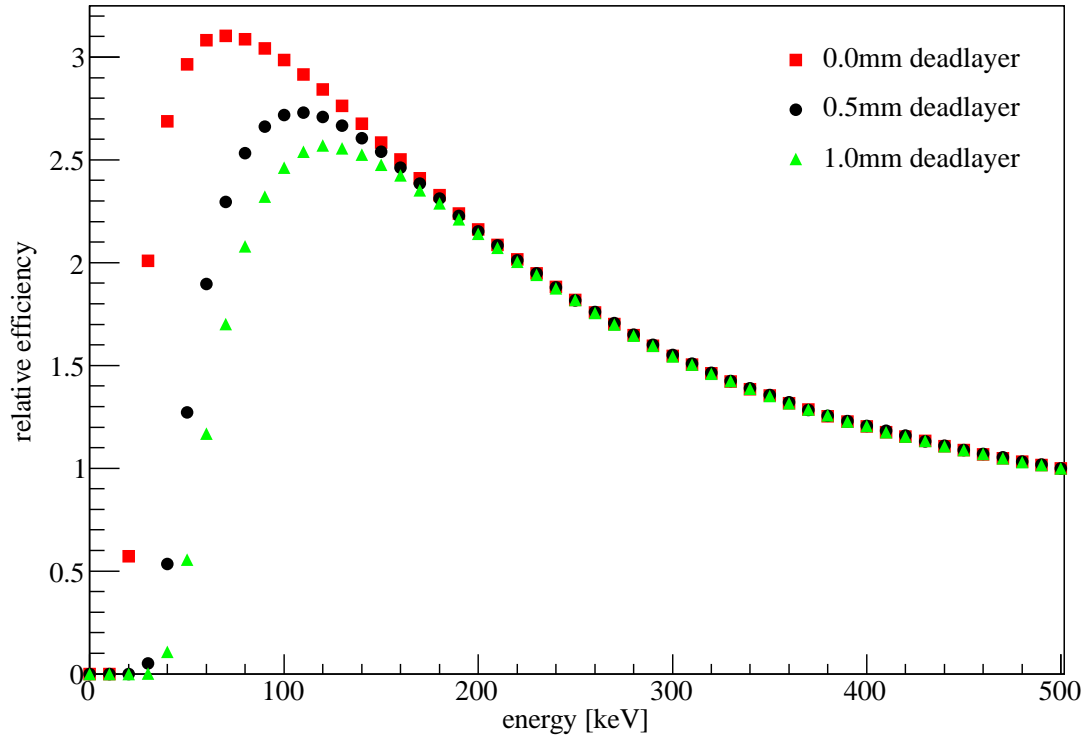
Figure A.1: Relative full energy peak efficiency for the detection of γ-rays of different energies without addback assuming that the germanium crystals have a dead layer with a thickness of $l_{\text{dead}} = 0.0$, 0.5 or $1.0\,\text{mm}$. The efficiency was derived from a GEANT4 simulation of the three clover detectors in the geometrical arrangement as shown in figure 2.5 and the γ-rays were emitted from the implantation position. The data is normalized to the efficiency at $E_\gamma = 500\,\text{keV}$. The statistical errors are smaller than the used symbols.

relative efficiencies in this figure. In this case an accurate knowledge of the thickness of the dead layer is not necessary as the efficiencies for energies $E_\gamma \gtrsim 0.2\,\mathrm{MeV}$ with a dead layer thickness of $l_{\mathrm{dead}} = 0\,\mathrm{mm}$ and $1\,\mathrm{mm}$ differ by less than 1% from each other.

A.3 Half-lives and beta-delayed neutron emission probabilities from literature

Nuclide	$t_{1/2}$	$P(\beta n)$ [%]	$P(\beta 2n)$ [%]	original source
^{27}Ne	31.5(13) ms	2.0(5)		[Tri06, Ten92]
^{27}Na	301(6) ms	0.13(4)		[Roe74, GM84]
^{27}Mg	9.458(12) min			
^{28}Ne	18.9(4) ms	11.9(7)	3.6(5)	
^{28}Na	30.5(4) ms	0.58(12)		[Roe74]
^{28}Mg	20.915(9) h			
^{29}F	2.5(3) ms	100(80)		[Dlo99, Not98, Ree99], [Pen01, Tar97]
^{29}Ne	14.8(3) ms	28(5)	4(1)	
^{29}Na	44.9(12) ms	21.5(30)		[GM84]
^{29}Mg	1.30(12) s			
^{29}Al	6.56(6) min			[Sei49]
^{30}Ne	7.3(3) ms	13(4)	8.9(23)	[Tri07a]
^{30}Na	48(2) ms	30(4)	1.15(25)	[Lan84, GM84]
^{30}Mg	335(17) ms			
^{30}Al	3.62(6) s			
^{31}Na	17.0(4) ms	37(5)	0.87(24)	[GM84]
^{31}Mg	232(15) ms	1.7(3)		
^{31}Al	644(25) ms	< 1.6		

Table A.1: Experimental half-lives, $P(\beta n)$ and $P(\beta 2n)$ values from [Eva12] or the references indicated in the last column. These values were used as input parameters for the half-life fits of implanted nuclei at the ^{30}Ne run.

Nuclide	$t_{1/2}$	$P(\beta n)$ [%]	$P(\beta 2n)$ [%]	original source
^{33}Mg	90.5(16) ms	14(2)		
	95.5(3) ms (preliminary)			[Kun12]
^{33}Al	41.7(2) ms	8.5(7)		
	37.4(6) ms (preliminary)			[Kun12]
^{34}Mg	20(10) ms	?		[Lan84]
	47(1) ms (preliminary)			[Kun12]
^{34}Al	42(6) ms	27(5)		
^{34}Si	2.77(20) s			
^{34}P	12.43(8) s			
^{35}Na	1.5(5) ms	?		[Lan83]
	3.3 ms(calc)	57(calc)	11(calc)	[Möl97]
^{35}Mg	70(40) ms,	52(46),		[Ree95]
	33.8 ms(calc)	21(calc)	14(calc)	[Möl97]
	14(3) ms (preliminary)			[Kun12]
^{35}Al	37.2(8) ms	38(2)		[Num01, Tim05]
^{35}Si	0.78(12) s	< 5		
^{35}P	47.3(8) s			
^{36}Mg	3.9(13) ms	48(12) (prel)		[Gré04, Yon99]
		28(calc)	3(calc)	[Möl97]
^{36}Al	90(40) ms	< 31		
	10.7 ms(calc)	2.8(calc)	6.7(calc)	[Möl97]
^{36}Si	0.45(6) s	< 10		[Duf86, Mue88]
		80.6(calc)		[Möl97]
^{36}P	5.6(3) s			
^{37}Al	10.7(13) ms			[Gré04]
^{37}Si	90(60) ms	17(13)		
^{37}P	2.31(13) s			[Duf86]
^{38}Al	7.6(6) ms	84(19) (tent)		[Gré04]
		0(calc)	11(calc)	[Möl97]
^{38}Si	> 1 μs	38(7) (tent)		[Zho91]
	90 ms(sys)			[Aud03]
	0.5 s(calc)	30(calc)		[Möl97]
^{38}P	0.64(14) s	12(5)		[Duf86]

Table A.2: Experimental half-lives, $P(\beta n)$ and $P(\beta 2n)$ values from [Eva12] or the references indicated in the last column. These values were used as input parameters for the half-life fits of implanted nuclei at the ^{36}Mg run.

A.4 Gamma-ray spectra of ^{38}Si from previous measurements
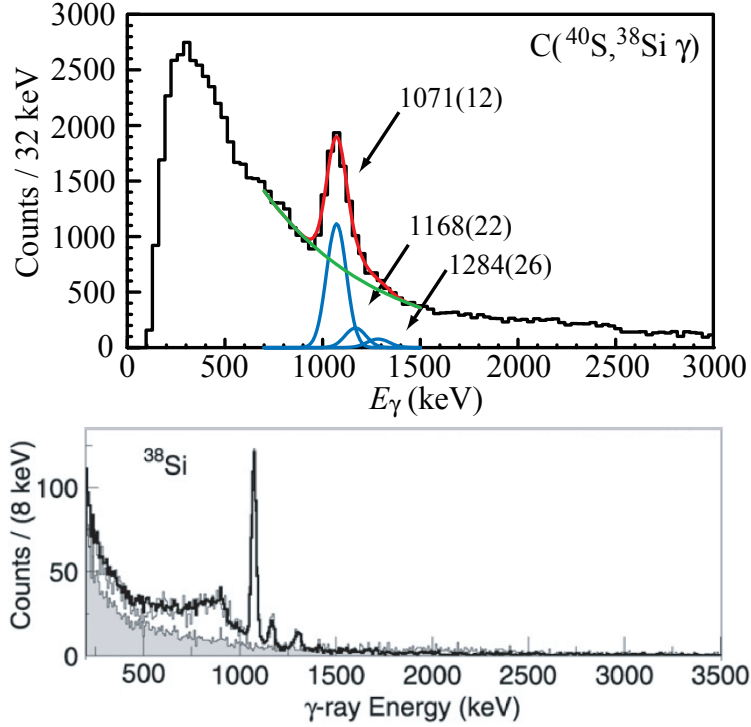
Figure A.2: *Top:* γ-ray spectrum at the C(^{40}S,^{38}Si γ) reaction reported in [Tak12]. *Bottom:* Prompt γ-ray spectrum from inelastic scattering of ^{38}Si ions in a liquid hydrogen target reported in [Cam07].

Figure A.2 shows two γ-ray spectra of previous measurements of ^{38}Si. The top one is from a C(^{40}S,^{38}Si γ) reaction [Tak12] and the bottom one displays the prompt γ-ray spectrum from inelastic scattering of ^{38}Si ions in a liquid hydrogen target [Cam07]: In both spectra there are three peaks at the energies 1071(12), 1168(22) and 1284(26) keV.

A.5 Expected number of coincident events

To calculate the expected number of detected γ-γ coincident events one assumes that there is a cascade of two γ-rays, γ_2 followed by γ_1. The level which is populated by γ_2 may also be populated by other transitions, γ_3, γ_4 and so on, but it is only deexcited by γ_1 and there is no other transition which deexcites this level (see an example in figure A.3). The number of emitted γ-rays is defined as N_1 for γ_1, N_2 for γ_2, N_3 for γ_3 and so on. As a consequence $N_1 = \sum_{i=2}^{i_{\max}} N_i + N_\beta$ with N_β being the number of events with direct β-feeding to this level. The number of detected events of each γ-ray γ_i is
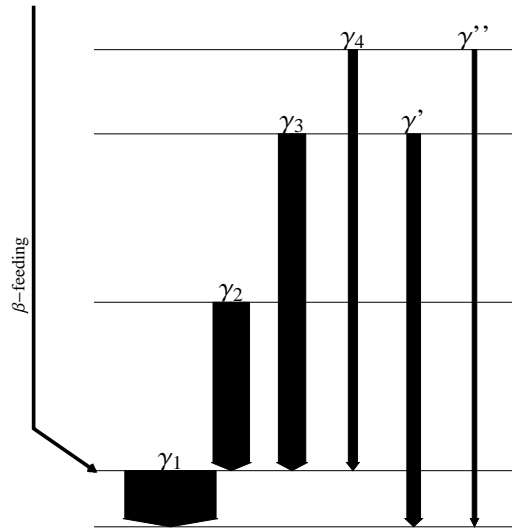
Figure A.3: Example of a level scheme to explain the calculation of the expected number of detected coincident events of γ_1 and γ_2 (details given in the text).

$d_i = \epsilon_i N_i$ with ϵ_i being the energy-dependent detection efficiency. In total there are N_2 events with a cascade of γ_2 and γ_1. Consequently the number of detected coincident events is $d_{\text{coinc 1-2}} = \epsilon_1 \epsilon_2 N_2$. As the term $\epsilon_2 N_2$ is equal to the number of detected γ-rays d_2 it can be extracted from a single γ-ray spectrum. The only input parameter is the efficiency ϵ_1 which can be taken from the simulation (see section 3.2.2). With the results of e.g. $d_{\text{coinc 156keV-562keV}}$ or $d_{\text{coinc 156keV-1115keV}}$ after the decay of ^{37}Al one can calculate the expected number of detected γ-γ coincident events $d_{\text{coinc } E_1 E_2}$ after the decay of ^{38}Al and compare it to the number of detected γ_{E1}-γ_{E2} coincident events. From the comparison one can decide whether γ_{E2} and γ_{E1} are emitted in a (coincident) cascade or not.

List of Figures

List of Tables

Bibliography

[Aoi06]   N. Aoi, Journal of Physics: Conference Series 49(1) (2006) 190. 11

[Aud03]   G. Audi, O. Bersillon, J. Blachot, and A. Wapstra, Nuclear Physics A 729(1) (2003) 3 – 128. 30, 69, 85

[Bel05]   M. Belleguic, F. Azaiez, Z. Dombrádi, D. Sohler, M. J. Lopez-Jimenez, T. Otsuka, M. G. Saint-Laurent, O. Sorlin, M. Stanoiu, Y. Utsuno, Y.-E. Penionzhkevich, N. L. Achouri, J. C. Angelique, C. Borcea, C. Bourgeois, J. M. Daugas, F. D. Oliveira-Santos, Z. Dlouhy, C. Donzaud, J. Duprat, Z. Elekes, S. Grévy, D. Guillemaud-Mueller, S. Leenhardt, M. Lewitowicz, S. M. Lukyanov, W. Mittig, M. G. Porquet, F. Pougheon, P. Roussel-Chomaz, H. Savajols, Y. Sobolev, C. Stodel, and J. Timár, Phys. Rev. C 72 (2005) 054316. 69, 77

[Bro88]   B. A. Brown and B. H. Wildenthal, Annual Review of Nuclear and Particle Science 38(1) (1988) 29–66. 50

[Cam07]   C. Campbell, N. Aoi, D. Bazin, M. Bowen, B. Brown, J. Cook, D.-C. Dinca, A. Gade, T. Glasmacher, M. Horoi, S. Kanno, T. Motobayashi, L. Riley, H. Sagawa, H. Sakurai, K. Starosta, H. Suzuki, S. Takeuchi, J. Terry, K. Yoneda, and H. Zwahlen, Physics Letters B 652(4) (2007) 169–173. 86

[Can]   Canberra   website,   *http://www.canberra.com/pdf/Products/ Detectors_pdf/clover.pdf*. 17, 18

[Cau99]   E. Caurier and F. Nowacki, Acta Phys. Pol. B 30(3) (1999) 705. 48

[Cau04]   E. Caurier, *http://sbgat194.in2p3.fr/~theory/antoine*, *shell model code ANTOINE, IRES, Strasbourg*, 1989–2004. 48

[Cau05]   E. Caurier, G. Martínez-Pinedo, F. Nowacki, A. Poves, and A. P. Zuker, Rev. Mod. Phys. 77 (2005) 427–488. 48

[Chu05]   J. A. Church, C. M. Campbell, D.-C. Dinca, J. Enders, A. Gade, T. Glasmacher, Z. Hu, R. V. F. Janssens, W. F. Mueller, H. Olliver, B. C. Perry, L. A. Riley, and K. L. Yurkewicz, Phys. Rev. C 72 (2005) 054320. 66, 76

[Coh65]   S. Cohen and D. Kurath, Nuclear Physics 73(1) (1965) 1 – 24. 1

[Dlo99] Z. Dlouhý, Y. Penionzhkevich, R. Anne, D. Baiborodin, C. Borcea, A. Fomichev, D. Guillemaud-Mueller, R. Kalpakchieva, M. Lewitowicz, S. Lukyanov, A. C. Mueller, Y. Oganessian, R. D. Page, A. Reed, M. G. Saint-Laurent, E. Sokol, N. Skobelev, O. Sorlin, O. Tarasov, V. Toneev, and W. Trinder, Journal of Physics G: Nuclear and Particle Physics 25(4) (1999) 859. 84

[Dom06] Z. Dombrádi, Z. Elekes, A. Saito, N. Aoi, H. Baba, K. Demichi, Z. Fülöp, J. Gibelin, T. Gomi, H. Hasegawa, N. Imai, M. Ishihara, H. Iwasaki, S. Kanno, S. Kawai, T. Kishida, T. Kubo, K. Kurita, Y. Matsuyama, S. Michimasa, T. Minemura, T. Motobayashi, M. Notani, T. Ohnishi, H. J. Ong, S. Ota, A. Ozawa, H. K. Sakai, H. Sakurai, S. Shimoura, E. Takeshita, S. Takeuchi, M. Tamaki, Y. Togano, K. Yamada, Y. Yanagisawa, and K. Yoneda, Phys. Rev. Lett. 96 (2006) 182501. 69, 77

[Duf86] J. P. Dufour, R. Del Moral, A. Fleury, F. Hubert, D. Jean, M. S. Pravikoff, H. Delagrange, H. Geissel, and K. H. Schmidt, Zeitschrift für Physik A Hadrons and Nuclei 324 (1986) 487–488. 85

[Ele06] Z. Elekes, Z. Dombrádi, A. Saito, N. Aoi, H. Baba, K. Demichi, Z. Fülöp, J. Gibelin, T. Gomi, H. Hasegawa, N. Imai, M. Ishihara, H. Iwasaki, S. Kanno, S. Kawai, T. Kishida, T. Kubo, K. Kurita, Y. Matsuyama, S. Michimasa, T. Minemura, T. Motobayashi, M. Notani, T. Ohnishi, H. J. Ong, S. Ota, A. Ozawa, H. K. Sakai, H. Sakurai, S. Shimoura, E. Takeshita, S. Takeuchi, M. Tamaki, Y. Togano, K. Yamada, Y. Yanagisawa, and K. Yoneda, Phys. Rev. C 73 (2006) 044314. 66, 76

[Eva12] Evaluated Nuclear Structure Data File, National nuclear data center, Database version of January 13, 2012, *http://www.nndc.bnl.gov/ensdf*, 2012. 30, 37, 38, 41, 64, 66, 69, 84, 85

[Fer34] E. Fermi, Zeitschrift für Physik 88 (1934) 161–177. 6

[Gad11] A. Gade, D. Bazin, B. A. Brown, C. M. Campbell, J. M. Cook, S. Ettenauer, T. Glasmacher, K. W. Kemper, S. McDaniel, A. Obertelli, T. Otsuka, A. Ratkiewicz, J. R. Terry, Y. Utsuno, and D. Weisshaar, Phys. Rev. C 83 (2011) 044305. 66, 76

[GEA03] GEANT4 Collaboration, S. Agostinelli, et al., Nuclear Instruments and Methods in Physics Research Section A: Accelerators, Spectrometers, Detectors and Associated Equipment 506(3) (2003) 250 – 303. 26

[GEA06] GEANT4 Collaboration, J. Allison, et al., IEEE Transactions on Nuclear Science 53(1) (2006) 270 –278. 26

[GM84] D. Guillemaud-Mueller, C. Detraz, M. Langevin, F. Naulin, M. de Saint-Simon, C. Thibault, F. Touchard, and M. Epherre, Nuclear Physics A 426(1) (1984) 37 – 76. 84

[Goe49]   M. Goeppert Mayer, Phys. Rev. 75 (1949) 1969–1970. 1

[Got07]   A. Goto, M. Fujimaki, T. Fujinawa, N. Fukunishi, H. Hasebe, Y. Higurashi,
          K. Ikegami, E. Ikezawa, N. Inabe, T. Kageyama, O. Kamigaito, M. Kase,
          M. Kidera, S. Kohara, M. Kobayashi-Komiyama, M. Nagase, K. Kuma-
          gai, T. Maie, T. Nakagawa, J. Ohnishi, H. Okuno, H. Ryuto, N. Sakamoto,
          M. Wakasugi, T. Watanabe, K. Yamada, S. Yokouchi, and Y. Yano, Proc.
          18th Int. Conf. on Cyclotrons and Their Applications, Giardini Naxos, Italy,
          (2007) 3–8. 10

[Gré04]   S. Grévy, J. C. Angélique, P. Baumann, C. Borcea, A. Buta, G. Canchel,
          W. N. Catford, S. Courtin, J. M. Daugas, F. de Oliveira, P. Dessagne,
          Z. Dlouhy, A. Knipper, K. L. Kratz, F. R. Lecolley, J. L. Lecouey, G. Lehrsen-
          neau, M. Lewitowicz, E. Liénard, S. Lukyanov, F. Maréchal, C. Miehé,
          J. Mrazek, F. Negoita, N. A. Orr, D. Pantelica, Y. Penionzhkevich, J. Péter,
          B. Pfeiffer, S. Pietri, E. Poirier, O. Sorlin, M. Stanoiu, I. Stefan, C. Stodel,
          and C. Timis, Physics Letters B 594(3-4) (2004) 252–259. 30, 63, 85

[Ham]   Hamamatsu   website,   *http: // sales. hamamatsu. com/ index. php? id=
          13199716* . 14

[Har77]   J. Hardy, L. Carraz, B. Jonson, and P. Hansen, Physics Letters B 71(2) (1977)
          307 – 310. 46

[Hax49]   O. Haxel, J. H. D. Jensen, and H. E. Suess, Phys. Rev. 75 (1949) 1766–1766.
          1

[Him08]   P. Himpe, G. Neyens, D. Balabanski, G. Bélier, J. Daugas, F. de Oliveira San-
          tos, M. D. Rydt, K. Flanagan, I. Matea, P. Morel, Y. Penionzhkevich, L. Per-
          rot, N. Smirnova, C. Stodel, J. Thomas, N. Vermeulen, D. Yordanov, Y. Ut-
          suno, and T. Otsuka, Physics Letters B 658(5) (2008) 203 – 208. 64, 66,
          76

[Hon05]   M. Honma, T. Otsuka, B. A. Brown, and T. Mizusaki, Eur. Phys. J. A 25
          (2005) 499. 50

[Hon08]   M. Honma et al., RIKEN Accel. Prog. Rep. 41 (2008) 32. 50

[Ibb99]   R. W. Ibbotson, T. Glasmacher, P. F. Mantica, and H. Scheit, Phys. Rev. C
          59(2) (1999) 642–647. 56

[Iwa01]   H. Iwasaki, T. Motobayashi, H. Sakurai, K. Yoneda, T. Gomi, N. Aoi,
          N. Fukuda, Z. Fülöp, U. Futakami, Z. Gacsi, Y. Higurashi, N. Imai, N. Iwasa,
          T. Kubo, M. Kunibu, M. Kurokawa, Z. Liu, T. Minemura, A. Saito, M. Ser-
          ata, S. Shimoura, S. Takeuchi, Y. Watanabe, K. Yamada, Y. Yanagisawa,
          and M. Ishihara, Physics Letters B 522(3-4) (2001) 227 – 232. 66, 76

[Kim05] K. Kimura, T. Izumikawa, R. Koyama, T. Ohnishi, T. Ohtsubo, A. Ozawa, W. Shinozaki, T. Suzuki, M. Takahashi, I. Tanihata, T. Yamaguchi, and Y. Yamaguchi, Nuclear Instruments and Methods in Physics Research Section A: Accelerators, Spectrometers, Detectors and Associated Equipment 538(1-3) (2005) 608 – 614. 11

[Kra87] K. S. Krane, *Introductory Nuclear Physics*, Wiley, New York, 3 edition, 1987. 6

[Kub03] T. Kubo, Nuclear Instruments and Methods in Physics Research Section B: Beam Interactions with Materials and Atoms 204 (2003) 97–113. 10

[Kun12] P. Kunz, *UCx03 @ 10 μA, http://www.triumf.ca/sites/default/files/ISAC%20Science%20Forum_February%2029%202012_Peter%20Kunz.pdf*, 2012. 85

[Lan83] M. Langevin, C. Détraz, D. Guillemaud-Mueller, A. Mueller, C. Thibault, F. Touchard, and M. Epherre, Physics Letters B 125(2-3) (1983) 116 – 118. 85

[Lan84] M. Langevin, C. Détraz, D. Guillemaud-Mueller, A. Mueller, C. Thibault, F. Touchard, and M. Epherre, Nuclear Physics A 414(1) (1984) 151 – 161. 30, 66, 84, 85

[Lee11] J. Lee, H. Scheit, N. Aoi, P. Doornenbal, E. Ideguchi, N. Kobayashi, Y. Kondo, G. Lee, K. Li, M. Matsushita, S. Michimasa, T. Motobayashi, H. Sakurai, D. Steppenbeck, M. Takechi, S. Takeuchi, Y. Togano, and H. Wang, RIKEN Accel. Prog. Rep. 44 (2011) 12. 11

[Lia06] X. Liang, F. Azaiez, R. Chapman, F. Haas, D. Bazzacco, S. Beghini, B. R. Behera, L. Berti, M. Burns, E. Caurier, L. Corradi, D. Curien, A. Deacon, G. d. Angelis, Z. Dombradi, E. Farnea, E. Fioretto, A. Hodsdon, A. Gadea, F. Ibrahim, A. Jungclaus, K. Keyes, A. Latina, S. Lunardi, N. Marginean, R. Menegazzo, G. Montagnoli, D. R. Napoli, F. Nowacki, J. Ollier, A. Papenberg, G. Pollarolo, V. F. E. Pucknell, M.-D. Salsac, F. Scarlassara, J. F. Smith, K. Spohr, M. Stanoiu, A. M. Stefanini, S. Szilner, N. Toniolo, M. Trotta, D. Verney, Z. Wang, and J. Wrzesinski, Phys. Rev. C 74(1) (2006) 014311. 45, 48, 53, 66, 70

[Möl97] P. Möller, J. Nix, and K.-L. Kratz, Atomic Data and Nuclear Data Tables 66(2) (1997) 131 – 343. 37, 38, 66, 85

[Mue88] A. C. Mueller, D. Bazin, W. D. Schmidt-Ott, R. Anne, D. Guerreau, D. Guillemaud-Mueller, M. G. Saint-Laurent, V. Borrel, J. C. Jacmart, F. Pougheon, and A. Richard, Zeitschrift für Physik A Hadrons and Nuclei 330 (1988) 63–68. 85

[Nis07] S. Nishimura, T. Sumikama, H. Sakurai, T. Ohnishi, T. Kubo, H. Scheit, M. Nishimura, T. Ohnishi, H. Kimura, A. Shiraki, Y. Ichikawa, H. Miyatake, S. Jeong, T. Hayakawa, Y. Wakabayashi, S. Kubono, S. Hayakawa, H. Yamaguchi, T. Teranishi, and N. Iwasa, Proposal for Nuclear Physics Experiment at RI Beam Factory RIBF NP-PAC-01 (2007). 13

[Not98] M. Notani, N. Aoi, N. Fukuda, M. Ishihara, H. Iwasaki, H. Ogawa, T. Kubo, S. Lukyanov, T. Nakamura, Y. Penionzhkevich, H. Sakurai, T. Teranishi, Y. Watanabe, K. Yoneda, and A. Yoshida, RIKEN Accel. Prog. Rep. 31 (1998) 71. 84

[Now09] F. Nowacki and A. Poves, Phys. Rev. C 79(1) (2009) 014310. 48, 49

[Num01] S. Nummela, P. Baumann, E. Caurier, P. Dessagne, A. Jokinen, A. Knipper, G. Le Scornet, C. Miehé, F. Nowacki, M. Oinonen, Z. Radivojevic, M. Ramdhane, G. Walter, and J. Äystö, Phys. Rev. C 63(4) (2001) 044316. 48, 64, 66, 70, 72, 76, 85

[Ohn08] T. Ohnishi, T. Kubo, K. Kusaka, A. Yoshida, K. Yoshida, N. Fukuda, M. Ohtake, Y. Yanagisawa, H. Takeda, D. Kameda, Y. Yamaguchi, N. Aoi, K. ichiro Yoneda, H. Otsu, S. Takeuchi, T. Sugimoto, Y. Kondo, H. Scheit, Y. Gono, H. Sakurai, T. Motobayashi, H. Suzuki, T. Nakao, H. Kimura, Y. Mizoi, M. Matsushita, K. Ieki, T. Kuboki, T. Yamaguchi, T. Suzuki, A. Ozawa, T. Moriguchi, Y. Yasuda, T. Nakamura, T. Nannichi, T. Shimamura, Y. Nakayama, H. Geissel, H. Weick, J. A. Nolen, O. B. Tarasov, A. S. Nettleton, D. P. Bazin, B. M. Sherrill, D. J. Morrissey, and W. Mittig, Journal of the Physical Society of Japan 77(8) (2008) 083201. 10

[Ots01] T. Otsuka, R. Fujimoto, Y. Utsuno, B. A. Brown, M. Honma, and T. Mizusaki, Phys. Rev. Lett. 87(8) (2001) 082502. 2

[Ots05] T. Otsuka, T. Suzuki, R. Fujimoto, H. Grawe, and Y. Akaishi, Phys. Rev. Lett. 95(23) (2005) 232502. 2, 3

[Ots08] T. Otsuka, T. Suzuki, and Y. Utsuno, Nuclear Physics A 805(1–4) (2008) 127c–136c. 50

[Ots10] T. Otsuka, T. Suzuki, M. Honma, Y. Utsuno, N. Tsunoda, K. Tsukiyama, and M. Hjorth-Jensen, Phys. Rev. Lett. 104(1) (2010) 012501. 2, 3, 50

[Pen01] Y. Penionzhkevich, Physics of Atomic Nuclei 64 (2001) 1121–1126. 69, 84

[Pri99] B. Pritychenko, T. Glasmacher, P. Cottle, M. Fauerbach, R. Ibbotson, K. Kemper, V. Maddalena, A. Navin, R. Ronningen, A. Sakharuk, H. Scheit, and V. Zelevinsky, Physics Letters B 461(4) (1999) 322 – 328. 69, 77

[Pri01] B. V. Pritychenko, T. Glasmacher, B. A. Brown, P. D. Cottle, R. W. Ibbotson, K. W. Kemper, and H. Scheit, Phys. Rev. C 63 (2001) 047308. 64, 66

[Ree95]   P. L. Reeder, Y. Kim, W. K. Hensley, H. S. Miley, R. A. Warner, Z. Y. Zhou, D. J. Vieira, and J. M. W. adn H. L. Seifert, Proc. Intern. Conf. on Exotic Nuclei and Atomic Masses, Arles, France, (1995) 587–588. 30, 85

[Ree99]   A. T. Reed, O. Tarasov, R. D. Page, D. Guillemaud-Mueller, Y. E. Penionzhkevich, R. G. Allatt, J. C. Angélique, R. Anne, C. Borcea, V. Burjan, W. N. Catford, Z. Dlouhý, C. Donzaud, S. Grévy, M. Lewitowicz, S. M. Lukyanov, F. M. Marqués, G. Martinez, A. C. Mueller, P. J. Nolan, J. Novák, N. A. Orr, F. Pougheon, P. H. Regan, M. G. Saint-Laurent, T. Siiskonen, E. Sokol, O. Sorlin, J. Suhonen, W. Trinder, and S. M. Vincent, Phys. Rev. C 60 (1999) 024311. 84

[Rex]   Rexon website, *http://www.rexon.com/RP408.htm*. 14

[Roe74]   E. Roeckl, P. F. Dittner, C. Détraz, R. Klapisch, C. Thibault, and C. Rigaud, Phys. Rev. C 10 (1974) 1181–1188. 84

[RV07]   E. Rodriguez-Vieitez, *Structure and cross section data of neutron-rich N∼20 nuclei produced in fragmentation and few-nucleon knockout reactions*, Ph.D. thesis, University of California, Berkeley, 2007. 69, 77

[Sei49]   L. Seidlitz, E. Bleuler, and D. J. Tendam, Phys. Rev. 76 (1949) 861–862. 84

[Sie11]   K. Sieja, *private communication*, 2011. 49

[Sin98]   B. Singh, J. Rodriguez, S. Wong, and J. Tuli, Nuclear Data Sheets 84(3) (1998) 487 – 563. 6

[Soh11]   D. Sohler, S. Grévy, Z. Dombrádi, O. Sorlin, L. Gaudefroy, B. Bastin, N. Achouri, J. Angélique, F. Azaiez, D. Baiborodin, R. Borcea, C. Bourgeois, A. Buta, A. Burger, L. Caceres, R. Chapman, J. Dalouzy, Z. Dlouhy, A. Drouard, Z. Elekes, S. Franchoo, S. Iacob, I. Kuti, B. Laurent, M. Lazar, X. Liang, E. Liénard, S. Lukyanov, J. Mrazek, L. Nalpas, F. Negoita, F. Nowacki, N. Orr, Y. Penionzkhevitch, Z. Podolyák, F. Pougheon, A. Poves, P. Roussel-Chomaz, M. Stanoiu, I. Stefan, and M. St-Laurent, Physics Letters B 703(4) (2011) 417–421. 56

[Ste09]   K. Steiger, *Effizienzbestimmung des Detektoraufbaus für die Zerfallsspektroskopie von ^{100}Sn*, Diplomarbeit, Technische Universität München, 2009. 27

[Tak03]   S. Takeuchi, T. Motobayashi, H. Murakami, K. Demichi, and H. Hasegawa, RIKEN Accel. Prog. Rep. 36 (2003) 148. 11

[Tak09]   S. Takeuchi, N. Aoi, T. Motobayashi, S. Ota, E. Takeshita, H. Suzuki, H. Baba, T. Fukui, Y. Hashimoto, K. Ieki, N. Imai, H. Iwasaki, S. Kanno, Y. Kondo, T. Kubo, K. Kurita, T. Minemura, T. Nakabayashi, T. Nakamura, T. Okumura, T. K. Onishi, H. Sakurai, S. Shimoura, R. Sugou, D. Suzuki, M. K. Suzuki, M. Takashina, M. Tamaki, K. Tanaka, Y. Togano, and K. Yamada, Phys. Rev. C 79(5) (2009) 054319. 11

[Tak12]   S. Takeuchi, M. Matsushita, N. Aoi, P. Doornenbal, K. Li, T. Motobayashi, H. Scheit, D. Steppenbeck, H. Wang, H. Baba, D. Bazin, L. Càceres, H. Crawford, P. Fallon, R. Gernhäuser, J. Gibelin, S. Go, S. Grévy, C. Hinke, C. R. Hoffman, R. Hughes, E. Ideguchi, D. Jenkins, N. Kobayashi, Y. Kondo, R. Krücken, T. Le Bleis, J. Lee, G. Lee, A. Matta, S. Michimasa, T. Nakamura, S. Ota, M. Petri, T. Sako, H. Sakurai, S. Shimoura, K. Steiger, K. Takahashi, M. Takechi, Y. Togano, R. Winkler, and K. Yoneda, Phys. Rev. Lett. 109 (2012) 182501. 53, 56, 76, 86

[Tar97]   O. Tarasov, R. Allatt, J. Angélique, R. Anne, C. Borcea, Z. Dlouhy, C. Donzaud, S. Grévy, D. Guillemaud-Mueller, M. Lewitowicz, S. Lukyanov, A. Mueller, F. Nowacki, Y. Oganessian, N. Orr, A. Ostrowski, R. Page, Y. Penionzhkevich, F. Pougheon, A. Reed, M. Saint-Laurent, W. Schwab, E. Sokol, O. Sorlin, W. Trinder, and J. Winfield, Physics Letters B 409(1-4) (1997) 64 – 70. 84

[Ten92]   O. Tengblad, M. J. G. Borge, L. Johannsen, B. Jonson, M. Lindroos, T. Nilsson, G. Nyman, A. Poves, H. L. Ravn, J. Retamosa, K. Riisager, P. Sona, and K. Wilhelmsen, Zeitschrift für Physik A Hadrons and Nuclei 342 (1992) 303–307. 84

[Tim05]   C. Timis, J. C. Angélique, A. Buta, N. L. Achouri, D. Baiborodin, P. Baumann, C. Borcea, S. Courtin, P. Dessagne, Z. Dlouhy, J. M. Daugas, S. Grévy, D. Guillemaud-Mueller, A. Knipper, F. R. Lecolley, J. L. Lecouey, M. Lewitowicz, E. Liénard, S. M. Lukyanov, F. M. Marqués, C. Miehé, J. Mrazek, F. Negoita, F. Nowacki, F. de Oliveira, N. A. Orr, J. Péter, S. Pietri, Y. E. Penionzhkevich, E. Poirier, M. Stanoiu, and G. Walter, Journal of Physics G: Nuclear and Particle Physics 31(10) (2005) S1965. 85

[Tri06]   V. Tripathi, S. L. Tabor, C. R. Hoffman, M. Wiedeking, A. Volya, P. F. Mantica, A. D. Davies, S. N. Liddick, W. F. Mueller, A. Stolz, B. E. Tomlin, T. Otsuka, and Y. Utsuno, Phys. Rev. C 73 (2006) 054303. 69, 84

[Tri07a] V. Tripathi, S. L. Tabor, P. F. Mantica, Y. Utsuno, P. Bender, J. Cook, C. R. Hoffman, S. Lee, T. Otsuka, J. Pereira, M. Perry, K. Pepper, J. S. Pinter, J. Stoker, A. Volya, and D. Weisshaar, Phys. Rev. C 76(2) (2007) 021301. I, III, 40, 43, 44, 75, 84

[Tri07b] V. Tripathi, S. L. Tabor, P. F. Mantica, Y. Utsuno, P. Bender, J. Cook, C. R. Hoffman, S. Lee, T. Otsuka, J. Pereira, M. Perry, K. Pepper, J. S. Pinter, J. Stoker, A. Volya, and D. Weisshaar, Phys. Rev. C 76(4) (2007) 049902. 40, 41, 42, 44

[Uts12]   Y. Utsuno, T. Otsuka, B. A. Brown, M. Honma, T. Mizusaki, and N. Shimizu, Phys. Rev. C 86 (2012) 051301. 3, 50, 53

[Uts13]   Y. Utsuno, *private communication*, 2013. 50, 61, 69, 70, 76

[Wan12]   M. Wang, G. Audi, A. Wapstra, F. Kondev, M. MacCormick, X. Xu, and B. Pfeiffer, Chinese Physics C 36(12) (2012) 1603. 46, 51, 54, 55, 57, 63, 64, 66, 69, 72

[Wei35]   C. F. v. Weizsäcker, Zeitschrift für Physik 96 (1935) 431–458. 7

[Wil83]   B. H. Wildenthal, M. S. Curtin, and B. A. Brown, Phys. Rev. C 28 (1983) 1343–1366. 37, 38

[Wil84]   B. Wildenthal, Progress in Particle and Nuclear Physics 11 (1984) 5 – 51. 1

[Wim10a] K. Wimmer, *Discovery of the shape coexisting 0^+ state in ^{32}Mg*, Ph.D. thesis, Technische Universität München, 2010. 4

[Wim10b] K. Wimmer, T. Kröll, R. Krücken, V. Bildstein, R. Gernhäuser, B. Bastin, N. Bree, J. Diriken, P. Van Duppen, M. Huyse, N. Patronis, P. Vermaelen, D. Voulot, J. Van de Walle, F. Wenander, L. M. Fraile, R. Chapman, B. Hadinia, R. Orlandi, J. F. Smith, R. Lutter, P. G. Thirolf, M. Labiche, A. Blazhev, M. Kalkühler, P. Reiter, M. Seidlitz, N. Warr, A. O. Macchiavelli, H. B. Jeppesen, E. Fiori, G. Georgiev, G. Schrieder, S. Das Gupta, G. Lo Bianco, S. Nardelli, J. Butterworth, J. Johansen, and K. Riisager, Phys. Rev. Lett. 105(25) (2010) 252501. 3

[Yan07]   Y. Yano, Nuclear Instruments and Methods in Physics Research Section B: Beam Interactions with Materials and Atoms 261(1-2) (2007) 1009–1013. 9

[Yon99]   K. Yoneda, H. Sakurai, N. Aoi, N. Fukuda, T. Gomi, E. Ideguchi, N. Imai, H. Iwasaki, T. Kubo, Z. Liu, S. M. Lukyanov, T. Nakamura, M. Notani, H. Ogawa, Y. E. Penionzhkevich, W.-D. Schmidt-Ott, S. Shimoura, E. Sokol, Y. X. Watanabe, A. Yoshida, X. Zhou, and M. Ishihara, RIKEN Accel. Prog. Rep. 32 (1999) 78. 55, 57, 65, 85

[Yon01]   K. Yoneda, H. Sakurai, T. Gomi, T. Motobayashi, N. Aoi, N. Fukuda, U. Futakami, Z. Gacsi, Y. Higurashi, N. Imai, N. Iwasa, H. Iwasaki, T. Kubo, M. Kunibu, M. Kurokawa, Z. Liu, T. Minemura, A. Saito, M. Serata, S. Shimoura, S. Takeuchi, Y. Watanabe, K. Yamada, Y. Yanagisawa, K. Yogo, A. Yoshida, and M. Ishihara, Physics Letters B 499(3-4) (2001) 233 – 237. 66, 76

[Zho91]   X. Zhou, X. Tu, J. Wouters, D. Vieira, K. Löbner, H. Seifert, Z. Zhou, and G. Butler, Physics Letters B 260(3-4) (1991) 285 – 290. 85

Acknowledgement

I would like to thank everyone who helped, contributed and supported me during this thesis: